Charting the Unknown: the Hunt for Dark Matter Continues

Haider Alhazmi

Submitted to the graduate degree program in the Department of Physics and Astronomy and the Graduate Faculty of the University of Kansas in partial fulfillment of the requirements for the degree of Doctor of Philosophy.

Professor Kyoungchul Kong, Chairperson

Professor Ian Lewis

Committee members

Professor Douglas McKay

Professor John Ralston

Professor Zsolt Talata

Professor Graham Wilson

Date defended: June 25, 2021

The Dissertation Committee for Haider Alhazmi certifies
that this is the approved version of the following dissertation :

Charting the Unknown: the Hunt for Dark Matter Continues

Professor Kyoungchul Kong, Chairperson

Date approved: July 9, 2021

Abstract

For thousands of years, the human mind struggles to answer a simple question: what is the universe made of? The majority of what composes our universe, dark matter and dark energy, are just mysteries. Undoubtedly, dark matter is one of the most interesting fundamental puzzles of our universe. While we have accumulated sufficient cosmological evidence supporting its existence, the character of the dark matter particle is still unknown. The widely successful theory of elementary particles, the standard model, is incapable of providing an interpretation of the dark matter puzzle, pressing towards new theories. A myriad of models have been proposed, the majority of which introduce a single dark matter candidate for simplicity. Though they provide testable hypotheses at various experiments, little attempt has been made beyond single-candidate dark matter. In this thesis, we go beyond single-candidate dark matter by focusing on two-component dark matter candidates. Surprisingly, their phenomenology is very different from that of single-candidate, providing a new avenue for dark matter experiments. In particular, we examine a novel thermal dark matter scenario where present-day annihilation of dark matter in the galactic center or in the Sun may produce subdominant but detectable boosted stable particles via neutral-current-like interactions. We scrutinize various scenarios where such dark matter of spin 0 and 1/2 interacts with electrons via an exchange of vector, scalar, axial-vector or pseudo-scalar mediators. Detailed detection prospects due to high or moderate Lorentz-boosted particles are studied at deep neutrino experiments and traditional direct detection experiments. We stress that the extension of dark matter models with more than one candidate beyond the minimal dark matter model opens up a new window for various experiments. Such a theoretical investigation and multiple experimental probes will advance our knowledge about dark matter and perhaps lead to its discovery in the near future.

Acknowledgements

I would like to express my sincere gratitude to my PhD advisor Prof. KC Kong. Thank you for your guidance, patience and most importantly for making my PhD journey an enlightening experience. Thank you for exposing me to multiple research areas, introducing me to many collaborators and encouraging me to participate in local and international workshops, conferences and summer schools. Thank you for dedicating an endless time and effort to teach me physics.

I also would like to thank all of the PhD committee members for their time, efforts and thoughtful comments. I am thankful to the physics department at the University of Kansas for providing a unique environment for learning and interacting. I extend my thanks to all of our professors, postdocs and colleagues in the High Energy Group for being great advisors, mentors and friends.

I acknowledge the financial support provided by Jazan University to cover my entire PhD program.

I would like to express my deepest thanks to my parents, my siblings and my wife for their unconditional support they provided through the years and during my PhD time.

Contents

1 Introduction **1**

1.1 Dark Matter and its Evidence 1

1.2 The Standard Model 9

1.3 Necessity of Theories Beyond the Standard Model 11

2 Dark Matter: Theory and Detection **17**

2.1 Weekly Interacting Massive Particles 17

2.1.1 Freeze-out 17

2.1.2 Weakly Interacting Massive Particles 20

2.2 Dark Matter Examples 22

2.3 Dark Matter Detection 25

3 Boosted Dark Matter at Large Volume Neutrino Experiments: High Energy Electron Recoil **32**

3.1 Introduction 32

3.2 Basic Model Setup 34

3.3 Experimental Details 38

3.4 The Galactic Center as a Source 40

3.4.1 BDM Galactic Flux and Signal 40

3.4.2 Detection Prospects 42

3.5 The Sun as a Source 45

3.5.1 BDM Solar Flux and Signal 45

3.5.2 Detection Prospects 47

3.6 Discussion 49

4 Low Energy Electron Recoil in the Dark Matter Electron Scattering 51

4.1 Basic Kinematics Setup 51

4.2 Differential Cross Section 55

4.3 Atomic Ionization Form Factor 57

4.3.1 Non-relativistic Approximations 57

4.3.2 Relativistic Treatment: Dirac Continuum Energy 63

4.3.3 The Free Particle Limit of the Ionization Form Factor 73

5 Boosted Dark Matter at Direct Detection Experiments: Low Energy Electron Recoil 76

5.1 Shape Analysis 76

5.1.1 The Models 76

5.1.2 Case Studies: Vector Mediator and Fermionic Dark Matter 80

5.1.3 Case Studies: all other Models 83

5.2 Scattering Energy Spectrum at Low Electron Recoil 86

5.3 The XENON1T Excess 88

6 Generic Fast Moving Dark Matter 96

6.1 General Framework 96

6.2 The XENON1T Excess Revisited 98

6.3 Prospects at Direct Detection Experiments 101

6.4 Mechanism Dependence: BDM as an Example 105

7 Conclusions 108

List of Figures

2.1 Dark matter thermal decoupling at different cross section values. Taken from Ref. [28]. 20

2.2 Current limits on WIMP dark matter assuming spin-independent cross section from various direct detection experiments experiments. Taken from Ref. [55]. 27

3.1 Feynman diagrams representing various interactions induced by the model. Self interaction between heavy states in the left panel, heavy-light state interaction in the middle and BDM interaction with electron in the right panel via a dark photon, V. 35

3.2 Annual number of BDM signal events expected from the GC at SK on the left and DUNE20 on the right. The numerical label above each contour indicates the minimum annual $N_{\text{sig}}^{\text{GC}}$ that any point in a parameter space enclosed by the same contour will produce. 43

3.3 Two-σ significance comparison between all four detectors considering TL1 and TL2 on left and right panel respectively. SK, HK, DUNE20 and DUNE40 are represented by solid blue, dashed black, solid red and dashed green respectively. 44

3.4 Annual number of BDM signal events expected from the Sun at SK on the left and DUNE20 on the right with σ_{00}^{min}. The numerical label above each contour indicates the minimum annual $N_{\text{sig}}^{\text{Sun}}$ that any point in the parameter space enclosed by the same contour will produce. 47

3.5 Two-σ significance comparison between all four detectors considering TL1 and TL2 on left and right panel respectively in detecting BDM from the Sun. SK, HK, DUNE20 and DUNE40 are represented by solid blue, dashed black, solid red and dashed green respectively. Here we assume minimum amount of self interaction. 48

3.6 Two-σ significance comparison between all four detectors considering TL1 and TL2 on left and right panel respectively in detecting BDM from the Sun. SK, HK, DUNE20 and DUNE40 are represented by solid blue, dashed black, solid red and dashed green respectively. Here we assume maximum amount of self interaction. 49

3.7 A rough reproduction of the results presented by the SK collaboration based on the discussion of the previous section. 50

4.1 Relativistic electron momentum density, left: for $3s$ and $5p_{1/2}$ of Xe atom and right: for $2s$ and $3p_{1/2}$ of Ar atom. 52

4.2 The PW approximation for the ionization form factor for a representative shells of Xe atom at different recoil energies. The solid curves represent equation (4.32) while the dashed ones represent our calculation in equation (4.30). 60

4.3 The PW ionization factor contribution from $5p$ ($3p$) shell of the Xe (Ar) atom on the left (right) panel. Different colors represent different examples of the electron recoil energy: red, blue, black and green correspond to $E_r = 0.015$ keV, 1 keV, 10 keV and 100 keV respectively. We purposefully chose the red curve to represent $E_r = 0.015$ keV to validate against existing literature, see main text. 61

4.4 The SCE ionization form factor: $5p$ shell of Xe on the left panel and the $3p$ shell of the Ar on the right panel. Different colors represent different examples of the electron recoil energy: red, blue, black and green correspond to $E_r =$ 0.1 keV, 1 keV, 10 keV and 100 keV respectively. 62

4.5 Transition factor for iodine $3s$ shell as a function of the momentum transfer at $\Delta E = 2$keV. Left: we test the convergence of the summation over κ' by fixing one potential method. Right we compare the transition factor given different methods for the potential. 69

4.6 Left iodine $3s$ transition factor as a function of the momentum transfer at $\Delta E = 4$keV for different potential methods. Right: Xe ionization form factor with contributions at $\Delta E = 2$keV from different energy shells. 70

4.7 Different transition factors that correspond to different mediator types. . . . 71

4.8 Xe ionization form factor as a function of the momentum transfer at different electron recoil energies represented by different colors. Left, center and right panels correspond to $5p$, $4d$ and $3s$ shells respectively. The dotted, dashed and solid line represent the PW, SCE and DCE approximations restrictively. Different colors represent different examples of the electron recoil energy: red, blue, black and green correspond to $E_r = 0.1$ keV, 1 keV, 10 keV and 100 keV respectively. 72

4.9 Ar ionization form factor as a function of the momentum transfer at different electron recoil energies represented by different colors. Left (right) panel corresponds to $3s$ ($2p$) shell. The dotted, dashed and solid line represent the PW, SCE and DCE approximations restrictively. Different colors represent different examples of the electron recoil energy: red, blue, black and green correspond to $E_r = 0.1$ keV, 1 keV, 10 keV and 100 keV respectively. 73

4.10 The asymptotic behavior of the ionization form factor as the recoil energy is increased. Different colors represent different examples of the electron recoil energy: red, blue, black and green correspond to $E_r = 100$ keV, 1 MeV, 10 MeV and 100 MeV respectively. The dotted lines represent the corresponding $|\mathbf{k}'|$ values given by $\sqrt{2m_eE_r + E_r^2}$. 74

5.1 Parameter space of m_1 and E_1 showing the curves that correspond to $E_r^{\max} = 1$ keV, 10 keV and 10 MeV in solid blue, green and red respectively. Also shows the curves that correspond to $v_{1e}/c = 0.1, 0.9$ and 0.99 in black dotted, dashed and solid respectively. 80

5.2 Differential cross section with respect to the electron recoil energy normalized to the total cross section. Left (right) panel corresponds to the VF (AF) scenarios while red, green and blue solid curves represent the first, second and third BMPs respectively. 85

5.3 Differential cross section with respect to the electron recoil energy normalized to the total cross section. Left (right) panel corresponds to the PF (PS) scenarios while red, green and blue solid curves represent the first, second and third BMPs respectively. 85

5.4 Top: Xe $3s$ and $5s$ shells in the left and right panels respectively. Notice the wide range of interest for the momentum transfer, $|\mathbf{q}|$. For first and second BMPs we are interested in the region where $|\mathbf{q}| < 60$ keV. For the third BMP, we are interested in the entire range. Bottom: the same as the top panel but for Ar $1s$ and $2s$ in the left and right panels respectively. 87

5.5 Differential cross section with respect to the electron recoil energy normalized to the total cross section. Left (right) panel corresponds to the VF (AF) scenarios while red, green and blue solid curves represent the first, second and third BMPs respectively. The solid curves correspond to the free scattering (the same as in figure 5.2), the dashed curves includes the PW approximation and the dotted curves include the DCE approximation. 88

5.6 Differential cross section with respect to the electron recoil energy normalized to the total cross section. Left (right) panel corresponds to the PF (PS) scenarios while red, green and blue solid curves represent the first, second and third BMPs respectively. The solid curves correspond to the free scattering (the same as in figure 5.3), the dashed curves includes the PW approximation and the dotted curves include the DCE approximation. 89

5.7 Number of dark matter signal at XENON1T for the two models: VF and AF in the left and right panel respectively. Red, green and blue represent first, second and third BMP respectively. The top row corresponds to the treatment explained in section 5.1 where electron is assumed free with $N_e^{\text{eff}} = 18.$. The bottom row consider the effects from binding energy as well as atomic effects, i.e., including the ionization form factor. Where dashed curves assume the PW approximation while dotted assume the DCE approximation. It only counts contributions from the outermost 3 shells of the Xe atom. 91

5.8 Number of dark matter signal at XENON1T for the two models: PF and PS in the left and right panel respectively. Red, green and blue represent first, second and third BMP respectively. The top row corresponds to the treatment explained in section 5.1 where electron is assumed free with $N_e^{\text{eff}} = 18$. The bottom row consider the effects from binding energy as well as atomic effects, i.e., including the ionization form factor. Where dashed curves assume the PW approximation while dotted assume the DCE approximation. It only counts contributions from the outermost 3 shells of the Xe atom. 92

5.9 Number of dark matter signal at XENON1T for VF model including the ionization form factor with allowed Xe shells where dashed curves assume the PW approximation while dotted assume the DCE approximation. Red, green and blue represent first, second and third BMP respectively. 94

6.1 The dark matter rate at XENON1T based on Ref. [136] where left panel adopts equation (6.7) while right panel adopts equation (6.5). The background in grey and data points correspond to those reported by the XENON1T collaboration [134]. Detector effects such as resolution and efficiency are discussed in section 5.3. 100

6.2 The log total rate of fast moving dark matter represented by colored contours for the VF model with mediator mass of 15 MeV. The four panels respectively represent the free scattering, PW, SCE and DCE cases. Only contributions from Xe 3 outermost shells are considered. 102

6.3 The log total rate of fast moving dark matter represented by colored contours for the PF model with mediator mass of 15 MeV. The four panels respectively represent the free scattering, PW, SCE and DCE cases. Only contributions from Xe 3 outermost shells are considered. 103

6.4 Comparison between VF and PF models in the left and right panel respectively with the mediator mass changing from 15 MeV in the top panel to 30 keV in the bottom panel. We only consider relativistic ionization form factor and contribution from all Xe atom shells. 104

6.5 The log of the factor f_1^{BDM} that quantifies the amount of fast moving dark matter. 106

6.6 The same as figure 6.4 but this time considering BDM scenario by taking the factor in equation (6.14) instead of a fixed constant parameter. 107

List of Tables

3.1 Comparison between the three different neutrino experiments in terms of volume, V_{exp}, energy threshold, E_{th} and angular resolution, θ_{res}. In our analysis, we use two examples of DUNE volume since its volume is planned to increase in 3 stages in increment of 10 kTon starting with two modules of 10 kTon LAr [112], therefore we consider 20 kTon (DUNE20) and 40 kTon (DUNE40). 39

3.2 Estimated annual number of background events from two sources at the three experiments. 40

4.1 The absolute values of the ionization energy of different shells for the Xe atom comparing different types of method for estimating the potential. 66

4.2 The absolute values of the ionization energy of different shells for the Ar atom comparing different types of method for estimating the potential. 67

5.1 Scenarios of simple dark matter interaction with electron. 77

5.2 Approximation of the differential cross section with respect to electron recoil energy for the 7 model scenarios in table 5.1 estimated at the three BMPs given by equation (5.7). 84

Chapter 1

Introduction

1.1 Dark Matter and its Evidence

The existence of dark matter as a major energy component in the universe is very well established by various cosmological and astrophysical observations. Yet, its particle nature is still a mystery. The fundamental characteristics such as its mass, spin and interactions are unknown. An ongoing indefatigable theoretical and experimental pursuit to unveil its particle nature has shown a null result so far.

There are many different pieces of cosmological evidence on the existence of dark matter and its history is long and rich. Here, we do not attempt to provide a comprehensive historical description but we refer the reader to review articles such as Refs. [1–3] and references therein. We list a few examples that will help us illustrate the general idea of dark matter and introduce the needed terminology for the rest of this thesis.

- *Rotational Curves*

  The idea of dark matter existed around 1933 after the observation made by Fritz Zwicky on the radial velocities of galaxies in the Coma cluster [4]. However, the term "dark" or its equivalent existed long before that. In order to explain the peculiarity of a motion of a particular astronomical object, astronomers, sometimes would hypothesize the existence of an unobserved object that is faint or dark. If such an object exists, the movement of the original object is no longer peculiar. A robust example on this was the prediction made by Urbain Le Verrier and John Couch Adams, that a planet later known as Neptune must exist in order to explain the movement of Uranus. Their prediction was precise enough to allow the discovery of Neptune in only one day.

What Zwicky had observed was that the radial velocity of galaxies in the Coma cluster was unexpectedly high. Considering the gravitational effect of the observed luminous matter, the estimated radial velocities should be much smaller. This contradiction between the observation and the prediction, especially when the observation has been independently confirmed, naturally leads to the hypothesis that some sort of unknown matter exists and its gravity would resolve the contradiction. This type of matter is known as the dark matter. Unlike the discovery of Neptune that took only one day, dark matter is not yet discovered for almost a century now! It is notable to mention that Zwicky applied the virial theorem to estimate the velocity dispersion of 800 galaxies of 10^9 solar mass within a system of size 10^6 light year to be 80 km/s. What he had observed on the other hand was an average velocity of 1000 km/s. Also, in 1937 Zwicky [5] attempted to estimate the mass to light ratio of the Coma cluster and he found a very high ratio of order 500. Today this ratio is smaller by roughly an order of magnitude due to the improved calculation of the Hubble parameter.

Not only these high radial velocities had been observed in the Coma cluster, they were also observed in the Virgo cluster by Sinclair Smith in 1936 [6]. Smith estimated the average mass per galaxy in the Virgo cluster to be 2×10^{11} solar mass, a very high value compared to Hubble's estimate of 10^9 solar mass. Moreover, this discrepancy had been observed on a galaxy scale rather than cluster scale. In 1939, Horace Babcock [7] observed that the rotational velocity of the outer region of the Andromeda galaxy was very high hinting towards unobserved mass in the galaxy. These kinds of observations persisted with time. In fact, 21-cm line[1] enabled one to study the rotational velocity of objects far from the center of a certain galaxy. For example, in the 1970s it was shown by Roberts and Whitehurst [8] that the rotation curve of the Andromeda galaxy

---

[1] A spectral line from hydrogen with wavelength of 21 cm.

remained constant up to distance 30 kpc[2]. *A rotation curve is a relation between the absolute distance of an object from the center of the galaxy and its rotational velocity around the galaxy.* If an extra component does not exist in the outer region of the galaxy, one would observe a falling curve. However it was observed that these curves remained stable for quite long distances. More than 30 years later, these rotational curves of the Andromeda galaxy are in a very good agreement with more recent observations, see for example Ref. [9]. These observations were not limited to the the Andromeda galaxy alone. For example, D. Rogstad and G. Shostak [10], studied five different galaxies and concluded that their rotational curves remained constant up to the largest observed radii.

- *Gravitational Lensing*

  The general theory of relativity predicted that when light passes close to a massive astronomical object, its path bends in response to the existence of the mass of the object. This of course has been observed in the famous experiment by Eddington during the total solar eclipse in 1919. This gravitational effect on light is called gravitational lensing and serves as further evidence on the existence of dark matter. Not only gravitational lensing proves the existence of dark matter but it also helps to quantify the distribution of dark matter in specific galaxies. There are different types of gravitational lensing that are related to dark matter [11, 12]. For example:

  - *strong lensing*: it is a phenomenon where the source of light is deflected by an intermediate object that is compact and dense enough to cause the original source to appear as multiple images or even a ring-shaped image at the observer. This ring is known as the Einstein ring and its size is related to the square root of the mass inside it. In 2008, a team studied the spectroscopy of almost 100 elliptical galaxies where a strong lensing effect was observed [13]. The total mass of an ellip-

---

[2] A kpc is one thousand parsec and a parsec is an astronomical unit of distance equivalent to 3.26 light years.

tical galaxy is contained within the geometrical lensed image. On top of that one can use the dynamics inside the elliptical galaxy itself by looking at the dispersion velocities. Together, a mass density distribution of these galaxies as a function of distance is inferred. These densities are found to be more extended than expected from luminous matter only, consequently supporting the dark matter hypothesis.

- *weak lensing*: the theory of weak lensing was developed in the early 1990s. In contrast to strong lensing, weak lensing does not cause the original sources to appear as multiple or ring-shaped images. However, it causes a distortion in the image due to the relatively small mass density of the intermediate object. At first order approximation, the distorted image is described by a linear transformation of the original source image. This transformation takes into account magnification, shear and rotation. Therefore, distorted images in the sky provide another probe on dark matter and its density. By the the end of the 1990s weak lensing was detected around many high mass clusters. In 2000, four independent research groups [14–17] have examined random batches of the sky and were consistently able to reach the same conclusion about the detected strength of weak lensing and the amount of dark matter per unit volume. In fact, weak lensing was also used to study dark matter on a much smaller scale, the scale of an individual galaxy. For instance, it is now assumed that different galaxies are structured inside an extended dark matter halo. Theoretically, these dark matter halos are responsible for the extra gravitational effect that is observed far beyond the galactic disc. It has been demonstrated that weak lensing can be used as a probe to constrain the shape of the mass density profile of these dark halos [18].
- *micro lensing*: it is similar in theory to the previous two types however in application it targets the gravitational effects due to much more compact and smaller objects such as planets and stars. In fact, it is widely used to examine the following well-known dark matter hypothesis. What we know is that there exists

an unobserved gravitational component with unknown nature. In analogy to the observed universe, one may simply assume that this unobserved component is baryonic in nature. This assumption will naturally lead this component to form structures that are similar to the observed universe. Moreover, one has to further assume that these structures are not luminous for some reason. These structures are known as massive astrophysical compact halo objects or MACHOs. A search for MACHOs has been proposed by the end of the 1980s predicting that if the dark matter halo is entirely made of MACHOs it will magnify bright stars in a close galaxy. This magnification or micro lensing event will occur roughly within a time equivalent to 130 days $\times\sqrt{M}$ where M is the mass of one MACHO in solar mass unit. It has been concluded that dark matter halos such as that of the Milky Way do not favor MACHOs as its major component. In fact MACHOs are not completely ruled out, an upper limit of 8% of the dark matter halo could be made of MACHOs [19] within a detectable micro lensing mass range.

- *Cosmic Microwave Background*

The Big Bang model is very successful in describing the ratio of light abundant elements to hydrogen. In the very early universe and during what is known as Big Bang Nucleosynthesis, light elements such as helium and deuterium were formed due to the fusion of protons and neutrons. In fact, the theoretical prediction of the ratio of these abundant elements to hydrogen is in a great agreement with observation. Moreover, the deuterium to hydrogen ratio is related to the overall density of baryons in the universe, $\rho_{\rm b}$. The ratio of the baryonic density to the critical density of the universe, $\Omega_{\rm b}$, multiplied by the reduced Hubble parameter squared, h^2 is approximately: $0.021 < \Omega_{\rm b}h^2 < 0.024$ [20]. Note that this limit is predicted theoretically by the Big Bang Nucleosynthesis and we should see in a moment how it agrees with observation very well! But how is this related to dark matter? The answer is in the cosmic microwave background (CMB). In the late 1940s, Ralph Alpher and Robert Herman suggested that the early universe was dominated by radiation. Penzias and Wilson discovered the CMB for the first time in 1964. In the early universe, charged particles and photons were dense and hot. While the universe was expanding, particles started to cool down and were able to recombine to form neutral atoms allowing photons to stream more freely. These photons are what we refer to as the CMB. Later in 1989, COBE (Cosmic Background Explorer) was launched and was able to get more characteristics of the CMB. It has been found that the CMB is very uniform across the sky with a temperature equivalent to 2.73 K. Despite being very uniform, the CMB was shown to have an order of 10^{-5} temperature fluctuations around its average temperature. These fluctuations can be understood on two major cosmological scales. First, on a very large scale, one can relate the fluctuations to the Sachs-Wolfe effect. Second, on a small scale, the fluctuations are related to the acoustic oscillation that took place before the decoupling of photons. At that time, photons and baryons were approximated as a fluid that compresses while falling into some gravitational well until it becomes very dense. The pressure of the fluid then increases allowing the fluid to expand. Due to the effect of the gravity of the potential well the fluid falls and compresses again. This process repeats itself until photons decouple from baryons. Therefore the fluctuations in the CMB can be attributed to the variation in the photon temperature due to the different stages of the acoustic oscillation.

The magnitude of the temperature fluctuation is very small, this fluctuation is related to the amount of baryonic matter in the universe. As cosmologists argue, if the matter in the universe is made up only from baryonic matter, the universe will not be in the same form today! Due to electric force, it is hard for the baryonic matter to start clumping in order to prepare for structure formation before the recombination epoch. They must be neutral in charge to start clumping together and that happens after recombination which consequently changes the time line of structure formation. Now dark matter comes to rescue the situation once again. If an extra matter component exists that is effectively neutral to the electromagnetic interaction, it would form potential wells allowing the baryonic matter to fall into them. In 2001, WMAP which stands for Wilkinson Microwave Anisotropy Probe was launched and it was equipped with very high resolution capabilities to study CMB fluctuations. According to WMAP [21], we now have an estimate on the total matter component in the universe to be $\Omega_{\rm m}h^2 = 0.1376 \pm 0.0020$, the baryonic matter $\Omega_{\rm b}h^2 = 0.02223 \pm 0.00033$ and the dark matter $\Omega_{\rm dm}h^2 = 0.1153 \pm 0.0019$. More recently, the Planck collaboration [22] reported improved measurements on the above parameters resulting in $\Omega_{\rm m}h^2 = 0.1428 \pm 0.0011$, $\Omega_{\rm b}h^2 = 0.02233 \pm 0.00015$, and $\Omega_{\rm dm}h^2 = 0.1198 \pm 0.0012$. That means dark matter is a major component accounting to a roughly 84% of the total matter in the universe. What is remarkable is that, when we try to theoretically explain the CMB power spectrum, we do not have much freedom on the values of the above parameters. In fact, it has been shown that small deviations in the value of these parameters will lead to a substantial difference in the shape of the CMB power spectrum and hence lead to disagreement with observation[3]. In addition to providing direct evidence on dark matter, CMB fluctuations helped us quantify the amount of dark matter in the universe. The parameter $\Omega_{\rm dm}$ above leads to the local dark matter density in the Sun's neighborhood to be $\rho_{\rm dm} \approx 0.3\,{\rm GeV/cm^3}$.

- *The Bullet Cluster*

A unique example on the existence of dark matter is what is known as the Bullet Cluster. It is a cosmological event in which two different clusters approach each other and subsequently collide or merge. Since the distance between the different galaxies within one cluster is very large, the galaxies of the two clusters pass through without any notable interaction. However, what is important in this case is the hot baryonic gas that exists between galaxies which forms the major baryonic component of the cluster. When the two clusters collide with each other at a relative velocity of a few million miles

---

[3] For an illustration, see figure 3 in Ref. [2].

per hour the hot gas is compressed and heated more. During the collision, an enormous amount of X-rays is emitted from the compressed baryonic gas. The location at which these X-rays are emitted traces back the location of the majority of the baryonic matter in the colliding system. Now, in order to determine the major gravitational component of the system, weak lensing is used. It has been found that the location of the major gravitational effect due to weak lensing is quite off from that corresponding to the X-ray emission. The X-ray emissions are more central while the major gravitational effect is located on both sides of the collision following the passing through galaxies. The first observation of the bullet cluster was made in 2006 for a cosmological system known as 1E 0657-56 [23]. Two years later another example was demonstrated on a system known as MACS J0025.4-1222 [24]. *What do these unique examples tell us?* They indicate that clusters are primarily made of a large non-luminous component supporting the dark matter hypothesis.

As a matter of fact, the bullet cluster is also used to eliminate some ad hoc alternatives to the dark matter hypothesis. One particular alternative is a version of Modified Newtonian Dynamics (MOND) in which the acceleration is artificially scaled by an overall factor that depends on the magnitude of the Newtonian acceleration. This factor is equivalent to one for large accelerations and hence will not modify the general picture we have for small scale structures such as the solar system. MOND is capable of explaining the flatness of the rotation curves that we encountered above. Rotation curves of different galaxies tend to be flat at high distances away from the center of the galaxy. The artificially introduced factor by MOND, makes the rotation curves in the outer region of a given galaxy more flat in contrast to Newtonian dynamics. In practice, all one needs to do is to perform a fit of this theory to the observed rotation curves and appropriately determine a numerical value of the factor. This had been proven to work for rotational curves, but as one can easily expect, it completely fails to describe the bullet cluster.

In fact, the bullet cluster example is a key evidence on the dark matter hypothesis, not only because it agrees with previous observation or manages to rule out some other theories, but also because it somewhat sheds light on the nature of dark matter. Physicists can now use it to set a limit on the strength of dark matter interaction, a point that we will attempt to address later.

1.2 The Standard Model

In the previous section, we have explored observational evidence on the existence of dark matter. We found that there is enough evidence on the existence of an extra major matter component in the universe. All of what we have discussed so far still does not answer the important fundamental questions about the nature of dark matter. Indeed, all evidence tell us that dark matter does respond to the gravitational interaction, however we do not yet know what other types of interaction it has. Moreover, we still lack other information such as the mass, spin and quantum charges. In other words, we still do not know what dark matter really is! The major questions we are concerned with here, are *how can we understand dark matter from the elementary particle physics point of view?* and *how can we phenomenologically determine its properties in experiments?*

To address the above questions, it is important to remind ourselves that we already have a very successful model that describes the observed elementary particles in the universe and their fundamental interactions. This model is known as the standard model (SM) of elementary particles. The SM is a mathematical framework that utilizes quantum field theory to explain all of the known elementary particles through their fundamental interactions: the electromagnetic interaction, the weak nuclear interaction and the strong nuclear interaction. The fourth fundamental interaction of nature, gravity, is not described by the SM. There are 17 fundamental particles in the SM which so far give a complete interpretation to the observed baryonic matter. In the SM, there are two fermionic sectors (spin-1/2 particles) known as leptons and quarks. Each sector has six particles in three matter generations with masses increasing from one generation to the next. There are four gauge bosons (with spin-1) carrying the fundamental interactions: the massless photon for the electromagnetic interaction, the massive Z and W bosons for the weak interactions and the massless gluon for the strong interaction. Finally, the Higgs boson (with spin-0) is theoretically introduced to provide a natural explanation for the origin of masses in the SM and was the last piece of the SM that was experimentally confirmed in 2012 at the large hadron collider (LHC).

The question we may ask here is, can we find at least one particle in the SM that could serve as a dark matter candidate? According to the dark matter evidence we provided above especially when we discussed CMB, a dark matter particle must be effectively neutral to the electromagnetic interaction. Also, dark matter existed in the early universe until now which means that it must have a very long lifetime or it must be a stable particle. Any particle in the SM with a sizable electric charge or short lifetime will fail to be a candidate for dark matter. In other words, we should exclude the 6 quarks, the 3 charged leptons and the three massive bosons. Also we should exclude the photon and the gluon since in addition to being massless they will have respectively sizable and strong interactions with baryonic matter. We are only left with the neutrinos. Neutrinos are electromagnetically neutral, stable and also have weak interaction strength since they interact through the weak gauge bosons only. Is dark matter composed of neutrinos?

To answer this particular question, let us consider the structure formation in the universe in view of two different types of dark matter. Let us characterize these two types by how relativistic they are and denote one by being very relativistic, hot dark matter, and the other as non-relativistic, cold dark matter. It turns out that, these two types will have diametrically different patterns for the structure formation in the universe. Hot dark matter will result in a “top-down” pattern while cold dark matter will lead to a“bottom-up” pattern [2, 3]. For example, simulations show that if dark matter is relativistic at the structure formation epoch, large scale structures will form first and then fragment to form small structures such as galaxies, “top-down”. On the other hand, cold dark matter will result in a “bottom-up” pattern in which small galaxies form first and then larger ones leading to clusters forming much later. In fact, the latter pattern is more favored by observation such as surveys of galaxy redshifts [25, 26]. Neutrinos are light mass particles that are produced in the early universe with velocities that are very relativistic. Apparently, neutrinos, if considered as dark matter, would serve as a hot dark matter component which will not lead to the structure formation we know today. When comparing the numerical simulation to the observations, it was evident that hot dark matter or neutrinos in particular can not account for the entire dark matter in the universe [27]. Moreover, analysis of the WMAP data had set a limit on the amount of SM neutrinos that could possibly contribute to the dark matter density in the universe, $\Omega_\nu h^2 < 0.0047$ [21].

1.3 Necessity of Theories Beyond the Standard Model

What is dark matter then? Despite all the success of the SM, it seems impossible for the SM alone to explain the dark matter. This indicates that the SM alone may not be the ultimate theory for the universe. One can argue that the SM is an effective theory that is very successful in the low energy limit but fails to explain physics at very high energies. Or maybe the SM is just one corner of a much more global theory that can explain the dark matter and beyond. With all of the cosmological and astrophysical evidence we mentioned above, we have strong motivations to go beyond the SM framework. Additionally, by examining the SM itself, we know that many questions remain unanswered. For example, why are there only three matter generations? Why does symmetry need to be broken in order to explain the masses of the elementary particles? Is the Higgs particle the only elementary scalar particle in the universe? Why is there a huge mass difference between the different particles within the SM? Indeed the SM is successful but not fully understood. Most of the theories that try to answer these questions (and more) end up extending the SM by adding more particles and interactions. Therefore, extension of the SM is based on both experimental evidence and theoretical motivations.

However, we should not abandon the SM at all! While questioning it, the SM should work as an inspiration and a guideline in searching for new physics. In fact, the neutrino as a candidate for dark matter, though it fails to be one, is a great example and does set the ground rules for other candidates. Many studies and reviews had collected the properties of dark matter particles to ensure a good candidacy, see for instance Refs. [28, 29]. Here we summarize theoretical aspects of these properties and come back to the observational ones when we talk about dark matter detection in the next chapter.

- *abundance*: any hypothesized particle species for the dark matter should always respect the observational value of the amount of dark matter present in the universe. And if these species were in thermal equilibrium with SM particles in the early universe, then they have to follow what is known as the "freeze-out" process. In other words, when the expansion rate of the universe becomes much greater than the interaction rate of some particles, the probability of interaction drops significantly and leaves the particles at some particular fixed amount. That means, the co-moving density [4] of dark matter (and other particles) is dynamic based on the strength of their interactions while the universe was hot and dense, however, it becomes fixed after the universe cools down. This fixed co-moving density is called the relic abundance and is proportional to the density Ω_{dm} we introduced above. Note that this applies to any particle species which follows the thermal history of our universe.

- *cold*: as we have learned from the neutrino example above, a major part of dark matter has to be cold, i.e., non-relativistic. To be more precise, the hypothesized particle species should respect the "bottom-up" structure formation pattern that is favored by observation. In fact, the standard model of cosmology adapts a framework where the universe is modeled by a cosmological constant, Λ, and cold dark matter, CDM, collectively denoted by ΛCDM. The success of such a simple model and the

---

[4] It is a dynamical quantity for the number density of a given species that takes into account the expanding universe.

agreement of the numerical simulations with the observations favors the cold dark matter hypothesis.

Generally, and without specifying any particular model, there are two other types of dark matter one can consider when examining the temperature or how relativistic dark matter is: hot and warm [30].

- *hot*: hot dark matter is any relativistic massive stable particle that decouples when the universe was at temperature $\lesssim T_{\mathrm{qh}} \sim \Lambda_{\mathrm{QCD}}$ [31]. The temperature at T_{qh} is quark-hadron phase transition which defines the approximate boundary between hot and warm dark matter. Above that temperature, the number of relativistic particles increases due to the presence of different quark-antiquark pairs. One particular example of hot dark matter is SM neutrinos. We have seen above how the observational limit constraints the amount of relic neutrinos. In fact the relic abundance of neutrinos is related to the sum of the masses of different neutrino flavors, $\Omega_\nu h^2 = \frac{\sum m_\nu}{90\mathrm{eV}}$ [29]. In Ref. [32], a combination of different observations is performed to set a limit on the sum of neutrino masses as $\sum m_\nu < 0.14$ eV at 95 % confidence level and a year later, the Planck collaboration [22] found $\sum m_\nu < 0.12$ eV. This limit is roughly three times stronger than that of WMAP [21]. In fact these limits can be applied to any hot dark matter particle with a generic mass and we can infer the ratio of hot dark matter density that may contribute to the overall dark matter as $\Omega_\nu/\Omega_{\mathrm{dm}} \sim \frac{\mathrm{mass}}{10\mathrm{eV}} \lesssim 0.014$.
- *warm*: although cold dark matter is widely accepted, in terms of small scale structures, it still has few problems such as “too big to fail” and “core vs cusp” problems. We will discuss these issues in more details when we motivate strongly interacting dark matter particles in chapter 3. One of the suggested solutions for such problems is to use relatively warmer dark matter particles. These particles have velocities between those of cold and hot dark matter and in contrast to hot

dark matter they decouple at temperature above T_{qh} [31]. These particles lead to a structure formation that is similar to cold dark matter on large scales however it differs at small scales. Particularly, if the mass of warm dark matter is in the keV scale, a suppression in the formation of dwarf galaxies should occur. This suppression is inversely proportional to the mass of the warm dark matter particle and hence a lower limit is obtained on the mass by several studies. For example, results in Ref. [33] concluded that mass $\gtrsim 3.3$ keV.

- *stable*: the dark matter has to be long-lived on a cosmological scale. But before we talk about its stability, it might be interesting to consider the stability of the SM particles. Most of the fundamental particles in the SM as well as composite particles are unstable, heavy particles tend to decay to lighter ones while conserving quantities such as four-momentum, electric charges, lepton number and baryon number. In the SM, there are few examples where particles are stable. Stable particles are usually associated with some sort of symmetry or particle content to protect their stability. For example, the electron is the lightest charged particle in the SM and therefore it can not decay to other charged particles. The photon is also stable and has an exact gauge symmetry hence staying massless in contrast to massive gauge bosons which are unstable and their gauge symmetries are spontaneously broken. The proton, a composite particle, is also stable because it is the lightest baryon and its stability is protected by the conservation of baryon number. The lesson we learn is that stable particles naturally exist due to existing symmetries in the model [34]. Sometimes, when formulating a particular model, one would impose an *ad hoc* symmetry to ensure stability of the dark matter particle in the form of a discrete or a continuous global symmetry [35].

  The dark matter particle does not have to be strictly stable but its lifetime should be at least greater than the age of the universe. In fact, many well motivated dark matter models allow dark matter to be unstable but with a long lifetime.

- *neutral*: dark matter is electromagnetically neutral. Generally, it should not have a sizable interaction with the photon, a justification for the term “dark” and an interpretation for the CMB power spectrum as mentioned above. This on the other hand does not totally prevent suppressed interactions with photons, eventually dark matter has to interact with the SM model if we wish to detect it and study its particle nature. As a matter of fact, and as we will discuss later, many models consider small interactions between dark matter and the photon and consequently with charged SM particles.

- *interaction strength*: not only dark matter has to be effectively blind to the electromagnetic interaction, its interaction strength with the rest of the SM must be be relatively weak. By weak, we do not necessarily mean it has to be exactly similar to the weak interaction in the SM though such a choice lead to a remarkable coincidence in reproducing the right dark matter abundance in the early universe which we shall discuss in the next chapter. By weak we generally mean that dark matter should not have an interaction strength that is strong enough to contradict with the CMB observation. As we discussed above, dark matter plays an important role in interpreting the CMB power spectrum, and hence the size of the interaction between dark matter and neutral baryons should be small in general. On the other hand dark matter could have a sizable self interaction, a motivation that is used to alleviate some of the small scale structure problems which we will discuss later.

In summary of this chapter, we learned that dark matter does exist in the universe with a large amount and its gravitational interaction has been confirmed by various strong cosmological evidence. The simulations based on the standard model of cosmology can not be in a good agreement with observations unless dark matter is taken as a major component in the universe. Though dark matter exists, its particle nature remains a mystery and the SM of elementary particle physics, despite being successful, does not provide a suitable candidate for dark matter physics. Additionally, many questions about the SM remain unanswered, and therefore, both observation and theory necessitate the extension of the SM. We explored the general features that one needs to consider when postulating a new particle as a dark matter candidate. We now know at least a major component of the dark matter is non-baryonic, non-relativistic, effectively neutral, and its particle interaction with the SM, if it exists, must not be strong.

In the next chapter we will review one of the highly motivated paradigms of dark matter by introducing its general features and reviewing the "freeze-out" mechanism. Then, we will briefly explore different types of dark matter models and discuss the enormous mass range they occupy. Finally, we introduce different techniques of dark matter detection which all show a null dark matter signal so far.

Chapter 2

Dark Matter: Theory and Detection

2.1 Weekly Interacting Massive Particles

We have argued in the previous chapter the need for new theory beyond the SM to accommodate dark matter and explain its fundamental nature. Such a theory should be able to explain both dark matter and the SM altogether or at least it should not contradict the very-well tested SM. We have already listed the general features needed to be considered in order to agree with the observational limits on dark matter properties such as temperature, density and interaction strength.

2.1.1 Freeze-out

In this subsection we shall present a brief discussion on a dark matter particle species that was in a thermal equilibrium with the SM in the early universe and then decoupled at some time later. What motivates someone to do such a discussion is because of a very simple and reasonable assumption. If dark matter has any sizable interaction with the SM (this is precisely what one requires in order to detect dark matter) and it existed in the early universe then it is reasonable to assume that dark matter was in thermal equilibrium with the SM in the early universe. The thermal decoupling process considered is inspired by the SM ones and its great agreement with the observation. We mentioned in the previous chapter how the standard model of cosmology was very successful in determining the abundance of light elements. The abundance of a particular species is set after the thermal decoupling or the freeze-out. Therefore, a dark matter species will be treated on equal footing given that it was in thermal equilibrium.

Let us now assume that a stable dark matter species denoted generically by χ, has a mass m_χ and a number density n_χ with an implicit dependence on the temperature, T. The expansion rate of the universe is governed by the Hubble parameter, $H = \dot{a}/a$ where a is the the dimensionless scale factor. The rate of the interaction of dark matter with the SM, Γ, is proportional to the pair annihilation cross section, σ, of dark matter into SM and to the equilibrium number density, $n_{\chi,\mathrm{eq}}$. The Boltzmann equation that describes the cosmological evolution of n_χ can be represented as

$$\dot{n}_\chi + 3Hn_\chi = -\langle \sigma v \rangle \,(n_\chi^2 - n_{\chi,\mathrm{eq}}^2), \tag{2.1}$$

where $\langle \sigma v \rangle$ is the thermally averaged cross section and v is the relative velocity between interacting particles. Dark matter stays in equilibrium as long as $\Gamma \gg H$. However the universe continues to expand and Γ will fall below H at some time. The equilibrium number density eventually falls as $n_{\chi,\mathrm{eq}} \propto \exp{(-m_\chi/T)}$. In other words, once $T \gg m_\chi$, the dark matter annihilation rate drops far below the expansion rate and dark matter freezes-out. At that time, dark matter decouples from the thermal bath and becomes a thermal relic. To be able to validate this argument let us represent the above equation in a more convenient form in which the number density n_χ is replaced by the dimensionless co-moving density $Y_\chi \equiv n_\chi/s$, the mass is related to the temperature as $x \equiv m_\chi/T$ and the evolution in time is replaced by the evolution in the parameter x. The quantity s is the entropy density which is scaled as $s \propto T^3$ while the Hubble parameter is scaled as $H \propto T^2$ in a radiation dominated universe and they are related as $\dot{s} + 3Hs = 0$. One can also factor out the x-dependence as $H(T) = H(m_\chi)/x^2$ and $s(T) = s(m_\chi)/x^3$. Before, we rewrite the above equation we also change the time variable by realizing that $H = \dot{a}/a$ and $a \propto 1/T$ which means $dt = -dT/(HT) = xdx/H(m)$. With all of this notation introduced we can now represent the evolution of the dark matter species as

$$\frac{dY_\chi}{dx} = -\frac{1}{x^2}\,\frac{s(m)}{H(m)}\,\langle\sigma v\rangle\,(Y_\chi^2 - Y_{\chi,\mathrm{eq}}^2). \tag{2.2}$$

This is all one needs to study the evolution of a dark matter species in the early universe, however it is not an easy equation to solve. In fact we do not attempt to solve this equation here but rather highlight some of the important properties. First of all there exists no general analytical solution given the complexity in the dependence on the parameter x, for example both $Y_{\chi,\mathrm{eq}}$ and $\langle\sigma v\rangle$ are x-dependent, see for instance Refs. [28, 36]. Instead of solving the above equation let us examine its general behavior. Let us denote $\frac{s(m)}{H(m)}\,\langle\sigma v\rangle$ by a parameter λ that is in fact mass and x-dependent. For simplicity, let us assume λ is a free parameter that quantifies two major regimes: small and large λ. That means that when λ is very large it represents the regime where $\Gamma \gg H$, that is the case where dark matter is still in thermal equilibrium with the SM and simply, with decreasing x, Y_χ follows the equilibrium one, $Y_{\chi,\mathrm{eq}}$, which falls exponentially. We can think about it by looking at the left hand side of the above equation, when solution exists and its derivative is assumed finite, the quantity $(Y_\chi^2 - Y_{\chi,\mathrm{eq}}^2)$ should be very small to compensate the factor λ/x^2 that increases with decreasing x. Therefore, $Y_\chi^2 \approx Y_{\chi,\mathrm{eq}}$. Later after $x > x_f$, λ starts decreasing due to the fact that the universe expansion rate is much higher: $H \gg \Gamma$. At that time, Y_χ stops following the equilibrium one and fixes its value roughly at $Y_\chi \sim Y_\chi(x_f)$ i.e., freeze-out occurs. Therefore, a key quantity that determines when dark matter decouples from the thermal bath is $\langle\sigma v\rangle$. Figure 2.1 represents our discussion very well, the higher the cross section the later dark matter decouples. Moreover at high cross section the density of dark matter becomes smaller. This is somewhat anticipated, when particles have high annihilation cross section their amount will decrease. Certainly what we have discussed is incomplete since we ignored the x-dependence in the parameter λ. In that case one can use some numerical techniques to solve the differential equation fully. Even though our description

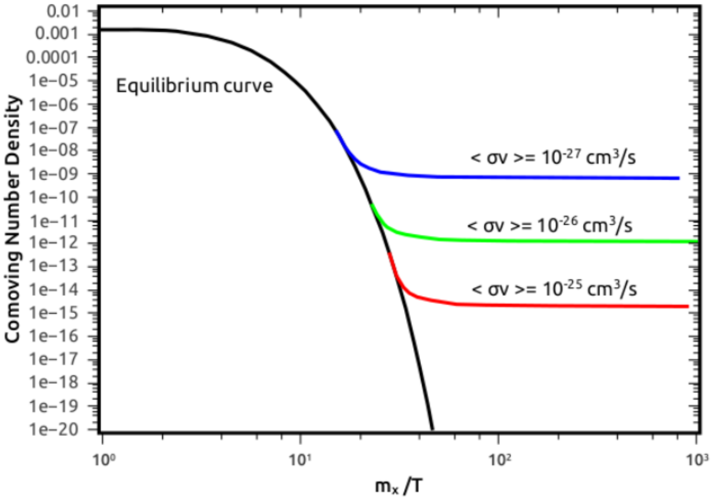

Figure 2.1: Dark matter thermal decoupling at different cross section values. Taken from Ref. [28].

is not complete, the full solution still follows similar behavior as in figure 2.1. One of the numerical packages that is widely used in the literature and dedicated to determining dark matter observables is known as `microOMEGAs` [37] and can be used to solve the dark matter Boltzmann equation.

2.1.2 Weakly Interacting Massive Particles

Let us now try to relate what we have discussed so far to the abundance of dark matter and see what one needs to match the one inferred from observation. The abundance is defined as the ratio of dark matter density to the critical density of the universe $\Omega_\chi = \rho_\chi/\rho_{\text{cr}}$. The critical density of the universe is defined as $\rho_{\text{cr}} = 3H^2M_{\text{pl}}^2/8\pi$ where M_{Pl} is the Planck constant. The density of dark matter can be related to the co-moving density that we presented in the previous section as $\rho_\chi = m_\chi Y_\chi s$. Therefore, once we know Y_χ, the solution to equation (2.2), we can readily determine the abundance Ω_χ. The co-moving density of dark matter at present day with temperature T_0 is found semi-analytically in Ref. [36] as:

$$Y_{\chi,0} \simeq \sqrt{\frac{\pi}{45}} M_{\rm Pl} \left[\int_{T_0}^{T_f} g_*^{1/2} \langle \sigma v \rangle \, dT \right]^{-1} , \tag{2.3}$$

where g_* is the number of relativistic degrees of freedom that are present in the thermal bath. Note that this equation is the integration of equation (2.2) from T_0 to T_f after ignoring $Y_{\chi,\rm eq}$ which is very suppressed and replacing s and H with their appropriate expressions. The approximation sign is to indicate that the term $1/Y_f$ is dropped given that it is very small in comparison with $Y_{\chi,0}$. Now we can write the abundance as

$$\Omega_\chi h^2 \approx 8.77 \times 10^{-11} {\rm GeV}^{-2} \left[\int_{T_0}^{T_f} g_*^{1/2} \langle \sigma v \rangle \, \frac{dT}{m_\chi} \right]^{-1} . \tag{2.4}$$

The question one asks now is what are the numerical values one needs to reproduce $\Omega_{dm} h^2 = 0.12$ which is favored by observation? Naively, and without focusing more on the temperature dependence of both g_* and the averaged cross section, if $g_* \sim 100$, $\langle \sigma v \rangle \sim 10^{-9}$ GeV^{-2} and $x \sim 20$ then one would reproduce the needed amount of dark matter, i.e., $\Omega_\chi \sim \Omega_{\rm dm}$. Also note that the abundance is inversely related to the cross section, something that would make the interpretation of figure 2.1 straightforward.

So far, there is nothing so intriguing about the discussion we have done. But on the other hand, we have not made any connection with particle physics that is required to generate such a cross section value. In reality the interpretation of the cross section and its implication on the SM is what makes this paradigm so attractive. From the previous discussion, it seems like if we have a new physics that is able to produce an averaged annihilation cross section with a numerical value in the neighborhood of 10^{-9} GeV^{-2} or $10^{-26}\,{\rm cm}^3/{\rm s}$, one would simply reproduce the required abundance. As we have discussed before, dark matter should be massive and has a very small interaction strength. If one proposes the interaction strength similar to that of the electroweak theory in the SM and chooses a mass in the electroweak scale, then the cross section is approximated by the Fermi 4-point interaction $\sigma \approx G_{\rm F}^2 T^2$

with G_{F} being the Fermi constant. Typically at freeze-out $T \sim m_\chi/20$, then with a mass of an electroweak scale $\sim$ 200 GeV one can reproduce the required abundance. These types of particle are called Weakly Interacting Massive Particles (WIMPs). Let us pause for a while and see what these choices of parameters offer. We have a dark matter particle that is: massive to account for the gravitational effect, weakly interacting providing small interaction strength, $m_\chi/T \sim 20$ i.e., relatively cold, effectively neutral, stable by assumption and most importantly agrees with the relic abundance of dark matter. This means that with the WIMP paradigm we are able to incorporate the general features we introduced in the previous chapter as "characteristics" of the dark matter particle.

What makes the WIMP paradigm so appealing is two coincidences, first, electroweak physics as a natural choice for a generic dark matter remarkably reproduces the right amount of dark matter in the universe. The second coincidence is the anticipation that some sort of new physics is associated with the electroweak theory to interpret long standing problems in the SM such as the hierarchy and naturalness.

2.2 Dark Matter Examples

Though the WIMP hypothesis has drawn great attention from both the theoretical and experimental sides, it is only one scenario of dark matter. In fact, if we study the allowed range of mass that dark matter may have, the WIMP regime is only few order of magnitudes in a range spanned by $\sim$50 order of magnitudes, assuming an elementary particle. There are other interesting theoretical scenarios that are used to probe the enormous range of dark matter mass. Here, we do not attempt to discuss every single scenario, but we rather mention some of the examples.

- *Extremely Heavy Objects*

  We start by discussing cosmological objects as an illustration on extremely large mass dark matter. We introduced MACHOs in the previous chapter as one hypothesis of dark matter and discussed how micro lensing can be used to limit such a hypothesis. Another example of cosmological objects is primordial black holes (PBHs). Though they are not fundamental particles but rather black holes which may have formed in the early universe due to collapse of large density perturbations during inflation, they serve as interesting dark matter candidates [38]. Because of their lifetime, PBHs must have a mass greater than 3×10^{-19} solar mass in order to exist to the present day. For recent constraints on PBHs refer to Ref. [39].

- *Thermal Dark Matter*

  Thermal dark matter generically refers to those dark matter particles which were in thermal equilibrium in the early universe and were produced thermally through the process of freeze-out. In the previous section we have introduced WIMP which has an interaction scale comparable to the electroweak scale making its mass ranging from a few GeV to a few TeV [5]. This particular type of WIMP or sometimes known as the standard WIMP is one of the most studied dark matter candidates. In fact WIMP properties do not have to be associated with the electroweak scale, one can simply assume that the annihilation cross section effectively proportional to g^4/m_χ^2 allowing a broader range of masses from an eV to 120 TeV, see for example Refs. [40, 41]. In general, thermal dark matter can be achieved through various theoretical approaches. One approach is through full and well defined models such as supersymmetry which provides the lightest neutralino as a candidate, see Refs. [41, 42] for recent reviews. A second approach would be through effective field theories (EFTs) which are assumed effective at some energy scale and hence only care about the interaction of the dark particle with the SM particle despite the origin and the details of the interaction which on the other hand can be derived from a full theory [43, 44]. Additionally, one can consider another approach known as simplified models where dark matter lives in the

---

[5] The driving factor for such a limit is not to overproduce dark matter, however this does not prevent other mechanisms to lower the limit to order of 100 MeV, see for example Ref. [40].

dark sector, the SM is another sector and there is a portal connecting the two sectors together through interaction. Popular examples of this kind of model include the Higgs portal and the dark photon portal where the former corresponds to the SM Higgs as a mediator [45] while the latter adopts a new massive vector boson that kinetically mixes with the SM photon which we will encounter in the next chapter.

- *Non-thermal Dark Matter*

  In a roughly similar mass range as thermal dark matter, there is another type of dark matter known as feebly interacting massive particles (FIMPs) [46] or sometimes known as extremely weakly interacting massive particles (EWIMPs) or super-WIMPs. As the names suggest, they account for particles whose interactions with the SM are much weaker than that of the WIMP. In contrast to the WIMP, these types of particle are not produced through the freeze-out mechanism but rather through a mechanism known as the freeze-in. The process of FIMPs production assumes a negligible amount of dark matter in the early universe. The process is described as follows: there exists a set of particles which are in thermal equilibrium at a temperature T while the FIMP denoted generically by X is effectively decoupled due to its extremely small interaction. Even though the interaction is feeble, through a renormalizable interaction, and while the universe temperature is dropping below the mass of X, the production of X is possible such that its mass is heavier than those interacting with it.

  Another example of non-thermal dark matter is the sterile neutrino that can not interact with the electroweak force and can be achieved by extending the SM by a right-handed singlet sector with mass in the range of keV to MeV. They mix with the SM neutrinos and are highly constrained by X-ray observation due to their decay to neutrinos and photons [47].

  A very well motivated example of non-thermal dark matter is the QCD axion generically occupying a mass range of peV to meV. The original purpose of the axion is to solve the CP problem (charge-parity violation) of the SM strong interaction while at the same time the axion provides a candidate for dark matter. The axion can be produced by an explicit breaking of a $U(1)_{\mathrm{PQ}}$ Peccei-Quinn symmetry [48] during the QCD phase transition in the early universe leading to a pseudo Nambu Goldstone boson serving as the axion. In fact, the phenomenon of breaking a $U(1)$ symmetry is general and not limited only to the QCD axion. Other theories can also produce axion like particles (ALP) in a similar manner as QCD axions, see Ref. [49] for a review. Finally there are a number of dark matter examples of a bosonic nature that have extremely small masses known as ultra light dark matter (ULDM) which span a mass range from 10^{-25} eV to an eV. One particular example of this type of dark matter is fuzzy dark matter whose introduction is motivated to reconcile small scale problems in ΛCDM [50, 51], see Ref. [52] for a general review on ULDM.

2.3 Dark Matter Detection

Given the variety of dark matter models, the natural question now is how can we detect the dark matter particle? Simply, all one needs is to observe an interaction of the dark matter particle with the SM. Once an observation is achieved, a particular dark matter model can be favored or disfavored based on the outcomes of the observation. Since all dark matter experiments have not observed a signal yet, a limit on the viability of the theoretical model is set based on the prediction given by the model. Phenomenologically, a particular dark matter model with a certain set of parameters predicts a signal at a certain experiment. When the experiment reports null results, a limit on the numerical values of the model parameters such as couplings and masses are set. This is indeed the current status of all dark matter experiments, the longer we run the experiment the more we tighten the parameter space of the theoretical models. In what follows, we will briefly mention some of the different types of dark matter detection techniques and what they can tell us about the dark matter particle.

- *Direct Detection*

  Direct detection experiments as an idea provides the most simple straightforward probes for the dark matter particle. In a nutshell, if dark matter exists in our galaxy with enough amount and an interaction with the SM is allowed, then we can build a detector composed of some material and wait until a signal is observed upon the traveling of dark matter particles around the galaxy. If we take a WIMP with mass $m = 100$ GeV and non-relativistic velocity $v = 10^{-3}$c as an example then one would anticipate a kinetic energy of order 50 keV. Therefore, an experiment has to be sensitive to this kind of energy in order to detect dark matter. Of course the energy changes based on the velocity and the mass, a typical range would then be from a keV to a few MeV. Usually, direct detection experiments are composed of relatively heavy nuclei and focusing on elastic WIMP-nucleus scattering [6], where the dark matter signal is anticipated as a nuclear recoil with energy, $E_{\rm nr}$, and a rate, R, given as [53]

$$\frac{dR}{dE_{\rm nr}} = \frac{\rho_{\rm dm}\, M}{m\, m_N} \int dv\, v f(v) \frac{d\sigma}{dE_{\rm nr}}. \tag{2.5}$$

  Here M is the mass of the detector, m_N is the mass of the nucleus, $\rho_{\rm dm} \approx 0.3\,{\rm GeV/cm^3}$ is the dark matter local density, $f(v)$ is the normalized dark matter velocity distribution in the galaxy and finally σ is the WIMP-nucleus scattering cross section. For a good review on the basics of direct detection see for example Ref. [54]. What the above equation tells us is the following: high mass/volume experiment is preferred and high cross section is needed to enhance the signal rate. At the first look, it might be desired to choose nuclei with smaller masses due to the presence of m_N in the denominator, however, the spin-independent cross section for example grows with the mass number squared while decreasing the nuclear recoil energy making heavy nuclei more preferred. But the rate corresponding to heavy nuclei falls rapidly at high nuclear recoil due to

---

[6] We will discuss later in this thesis the interaction of dark matter particle with electrons at direct detection experiments.

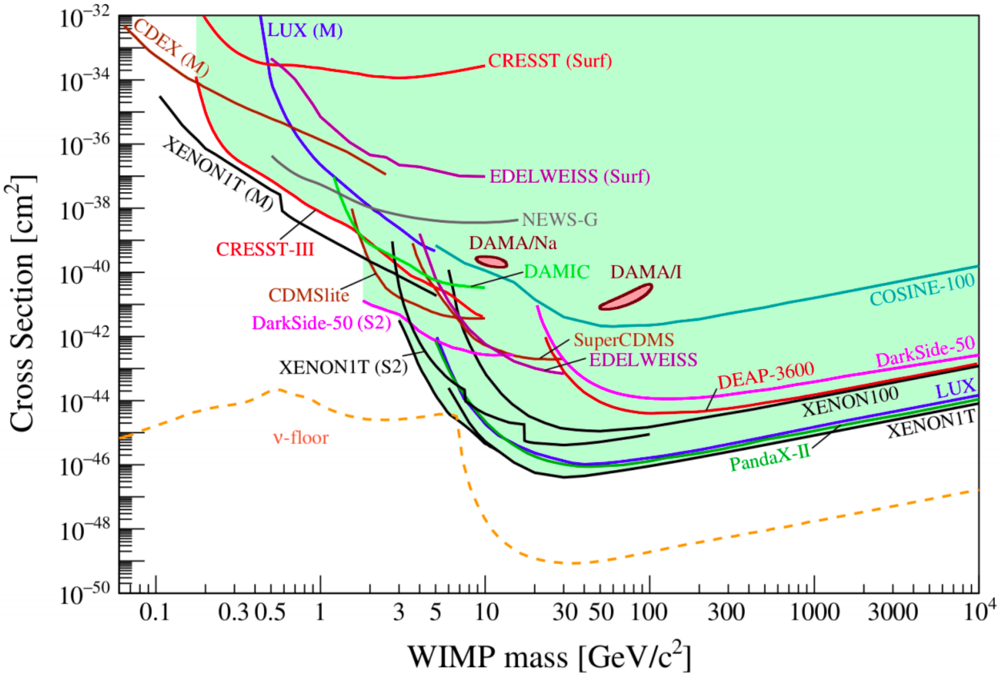

Figure 2.2: Current limits on WIMP dark matter assuming spin-independent cross section from various direct detection experiments experiments. Taken from Ref. [55].

the presence of the nucleus form factor, see for example figure 3 in Ref. [53]. There are many direct detection experiments facilitating different types of target materials such as germanium, xenon, argon, silicon and sodium iodine, see table 2 in Ref. [53].

Before we discuss the current status of the direct detection experiments, we comment briefly on the background at such experiments. Direct detection experiments generically provide a quiet environment however noise from background still exists in two major forms. First there is nuclear recoil background, for example neutron-induced nuclear recoils from spontaneous fission reactions or from cosmic ray muons is one of the crucial backgrounds since it can not be distinguished from a WIMP. Second, background from electron recoil due to photons in the surrounding environment or due to β decays inside the detector. Once the background is understood an analysis is carried out on the observed data testing the dark matter hypothesis or prediction as in equation (2.5). The usual outcome of the analysis is presented as limit curves in the cross section vs the mass space. Figure 2.2 shows the current limit in the mass vs cross section space for WIMP-nucleus scattering. The parameter space above the curves should be excluded. Experiments such as XENON1T, LUX and PandaX-II seem to have the most stringent limits for dark matter masses above a few GeV. As we can see a great deal of the parameter space has been probed already with null results despite some anomalies such as the DAMA/LIBRA one which is ruled out by other experiments. Also notice the orange dashed line representing an irreducible background known as the neutrino floor. This could be a challenge for dark matter discovery or could be a great opportunity to deepen our understanding about the background and hence design experiments accordingly.

- *Indirect Detection*

Indirect detection of dark matter is concerned with the dark matter annihilation or decay into SM particles in the universe. Therefore, a survey or scan is performed to the sky or sources in the sky attempting to observe an excess in some SM particles. This excess can be studied by measuring the flux, Φ. In general for dark matter with a mass m annihilating or decaying to neutral particles for example, the flux is given by [56]

$$\Phi(E,\phi) = \frac{\Gamma}{4\pi m^a}\frac{dN}{dE}\int \rho(\ell,\phi)^a\, d\ell, \tag{2.6}$$

where Γ is the rate of dark matter interaction which is inversely proportional to its lifetime τ, $\frac{dN}{dE}$ is the energy spectrum of the resulting SM particles which depends on the details of the process, a is 2 (1) for dark matter annihilation (decay) and finally the integral is performed over the line of sight for the dark matter density at the source. The idea of indirect detection seems very straightforward however one has to keep in mind the significance of systematic error due to the background from astrophysical sources. This leads one to explore scenarios where the rate can be enhanced, the energy spectrum has a distinct feature distinguishing it from background or focusing on regions of high dark matter densities.

There are many different ways of searching for dark matter indirectly depending on the resulting SM particles. One way is to search for neutrinos as a result of annihilating or decaying dark matter at experiments with large volumes and quiet environment such as Super-Kamiokande and IceCube or future deep underground neutrino experiment and Hyper-Kamiokande [7]. There are several sources to study neutrinos such as the galactic center and the stars including the Sun. However the Sun provides a very unique source due to its geometrical nature as a point like source, its closeness to Earth and also the difficulty of particles other than neutrinos escaping it, see for example Ref. [57] for neutrino searches. Another way of probing dark matter indirectly is through observation of excess X-rays. This kind of probe can be used for example to search for sterile neutrinos since they are assumed to decay to SM photons, see for example Ref. [58]. Additional ways of dark matter indirect detection are through searching for excess gamma rays which can be produced through a direct annihilation of dark matter into gamma rays pair or through emission of hadronized particles as a result of dark matter decay. Both X-ray and gamma ray searches can cover an energy range from less than a keV to a 1000 TeV. All of the above indirect probes commonly enjoy one thing, the particles for which they search are neutral and hence are not subject to deflection due to astrophysical magnetic fields. In fact, indirect detection can also be performed on charged particles such as charged cosmic rays with experiments covering an energy range from tens of MeV to roughly 10^9 TeV. However due to the complexity of modeling the astrophysical magnetic field, measurements will suffer from systematic uncertainty. Various experiments had studied charged particles such as positron and anti-proton and provided constraints on dark matter parameter space. For reviews of indirect detection results please refer to references such as [56,59].

- *Collider Physics*

In contrast to direct and indirect detection of dark matter where the signal is produced

---

[7] More about these types of experiments in the next chapter.

by the dark matter particle itself, collider physics provides a unique opportunity to produce the dark matter particle from the SM. Depending on the mass scale and the production mechanism (the model), dark matter can be produced from SM processes: SM + SM $\rightarrow n\chi + X$, where n indicates that the dark matter particle can be produced in multiples and X could be any set of SM particles or could be just nothing. Just like neutrinos at collider detectors, the dark matter signature will arise as missing energy. Therefore search techniques for dark matter are generally devoted into missing energy at colliders. Over the past, there have been efforts to study dark matter at colliders such as LEP: large electron positron collider at CERN see for example Refs. [60, 61] and the Tevatron (a proton collider) at Fermi Lab, see for example Ref. [62].

After its proven success in discovering the Higgs particle, the LHC with its high center of mass energy provides a great opportunity to probe dark matter at masses that have never been studied before at colliders. At the LHC, many types of dark matter scenarios can be probed ranging from full theories with particular predictions such as supersymmetry to EFTs and simplified models. After all, any dark matter process that can be initiated by a proton-proton collision is potentially possible to be probed by the LHC within its energy reach.

In efforts of searching for dark matter through complete models such as supersymmetry, both CMS and ATLAS experiments (two major experiments at the LHC) had studied different production mechanisms and various final states predicted by supersymmetry and presented their results as limits on the cross section vs mass space [63,64]. Another effort is studying dark matter production through new mediators of different spins as in some simplified models. This could be done by pair producing dark matter leading to large missing energy, associated production of dark matter and visible SM particle leading to imbalance in the transverse component of the momentum of the observed particles or by pair producing SM particles which could lead to the discovery of new mediators. Since the LHC is a proton-proton collider, if produced, a new resonance will most likely decay back to jets. Therefore, one of the channels to search for such resonances is through a pair of jets, see for examples [65, 66]. For more details of collider searches for dark matter see for example Refs. [67–70].

In a summary of this chapter, we discussed one of the highly motivated dark matter theory: the WIMP paradigm. We discussed how WIMPs can be produced in the early universe through the mechanism of freeze-out and highlighted the fact that a WIMP could give rise to the correct relic abundance of dark matter desired by observation if its interaction and mass are somewhat described by the electroweak physics. We then briefly discussed the wide mass range the dark matter particle may have and how other theories -other than WIMP- provide interesting solutions. Finally, we quickly went through some of the techniques of dark matter detection. In the next chapter, we will take a very specific model of dark matter that manages to evade the direct detection constraints above and at the same time provides a testable hypothesis at neutrino detectors.

Chapter 3

Boosted Dark Matter at Large Volume Neutrino Experiments: High Energy Electron Recoil

3.1 Introduction

With the stringent direct detection limits on "standard single-component" dark matter such as a WIMP, it is important to introduce scenarios that are capable of evading such stringent limits. In this chapter we are interested in studying a dark matter model that is non-conventional in the sense that the dark sector is non-minimal. The amount of dark matter in the universe is 6 times greater than the baryonic matter represented by the SM. The SM on its own is complicated and has a rich phenomenology: 3 fundamental interactions, 17 fundamental particles and hundreds of composite particles. The dark matter on the other hand is under no obligation to be minimal or single-component, it could be as complicated as the SM or even more. Therefore, we wish to focus our attention for the rest of this chapter on the simplest possible multi-component scenario: two-component dark matter with one component being abundantly dominant and heavy and the other sub-dominant and light. For concreteness we take a particular example model with a specific phenomenology in this chapter and generalize in the next ones.

We will focus our attention on what is known as boosted dark matter (BDM) and its detection at neutrino experiments while interacting with electrons. However, and before we discuss the model, it is notable to mention the different efforts in studying BDM. A BDM refers to a sub-dominant dark matter particle that acquired relativistic velocities due to an interaction in the dark sector while the dominant component is non-relativistic "conventional". The mechanism of producing such a relativistic velocity can be achieved through annihilation [71, 72], decay [73, 74], semi-annihilation [75–79] or through number changing self annihilation [80–82]. BDM can originate from different sources such as the center of the galaxy [73, 83–85], the Sun [86–89] and Spheroidal galaxies [90]. Detection prospects have been studied at various underground neutrino experiments.

In this chapter we begin by motivating the use of self interaction and discuss the basic structure of the model. We then focus our efforts on BDM from the galactic center and the Sun and discuss how BDM can be detected at large-volume deep underground neutrino experiments via interaction with electrons.

We have briefly discussed in the first chapter how ΛCDM, the standard model of cosmology (which utilizes cold dark matter as an essential ingredient in the universe) is very successful when it is compared to observation and simulation on large scale structures. Despite that, we know that there exists a tension between N-body simulation based on ΛCDM and the observation. This tension reveals itself as problems in the cosmology of small structures. The authors of Ref. [91] summarize four problems with a caveat: the simulations are generally based on models where the baryonic component of the universe is neglected. Also there have been discussions on whether these problems can be solved by including the effects from baryonic matter, see for example Refs. [92, 93].

One of these problems is the core vs cusp: the simulations suggest that the dark matter density of a galactic halo grows as 1/distance while approaching the center of the galaxy. On the other hand, many observations suggest a contradictory behavior. For example, it has been shown that the rotational velocities of dark matter dominated, low surface brightness galaxies [94] and gas-rich, halo-dominated dwarf spirals [95] favor a flat density distribution near the center. Another problem is the missing satellites: one of the predictions of ΛCDM is the amount of dark matter sub-halos. For instance, it is predicted that the Milky-way galaxy should have order of hundreds sub-halos which are capable of hosting smaller galaxies.

However, the number of Spheroidal galaxies that are discovered so far are far less than predicted [96]. This contradiction also exists in other galaxies as well, see for instance Ref. [97]. More recently, another problem was raised, the too-big-to-fail, increasing the tension between simulation and observation. It was realized that the most massive sub-halos (from prediction) are in direct inconsistency with the dynamics of the most bright Spheroidal galaxies (from observation) in the Milky-way. For example, as a result of simulation, the maximum circular velocity of 10 sub-halos is greater than those of the dwarf Spheroidal galaxies. This contradiction has also been shown in dwarf galaxies in Andromeda and the Large Group field.

Even though the aforementioned problems are debatable it is an interesting practice to see how these problems motivate new scenarios of dark matter and the phenomenological implications they lead to. As we mentioned in the first chapter, warm dark matter is considered as a solution to these problems. On the other hand, self interacting dark matter (SIDM) has been considered as another scenario to solve these problems [98]. For an excellent review please refer to Ref. [91]. It has been shown by simulation that SIDM resolves the tension with observation without altering the large scale structures if the ratio between its cross section and its mass, $\sigma_{\chi\chi}^{\rm self}/m_\chi$ is $\mathcal{O}(0.1-1)\,{\rm cm}^2/{\rm g}$ [99,100]. The stringent limit on the SIDM is provided by an analysis of the Bullet Cluster matter distribution as $\sigma_{\chi\chi}^{\rm self}/m_\chi < 1.25{\rm cm}^2/{\rm g}$ at 68 % confidence level [101] .

Therefore we would like to study BDM while incorporating the fact that a certain amount of self interaction is allowed. We will discuss the model and kinematic aspects first and then we will explore the possibility of signal detection at various neutrino experiments. We will study two main sources of dark matter and compare their signal detection.

3.2 Basic Model Setup

In this section we consider a specific dark matter model in which the dark sector is non-minimal. For simplicity we focus on two dark matter particles that are assumed fermionic

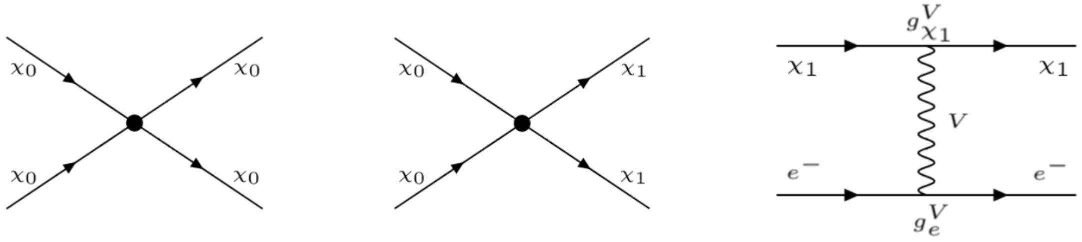

Figure 3.1: Feynman diagrams representing various interactions induced by the model. Self interaction between heavy states in the left panel, heavy-light state interaction in the middle and BDM interaction with electron in the right panel via a dark photon, V.

with a sufficient mass splitting between them. We denote the heavy state by χ_0 with a mass m_0 while the lighter state is denoted by χ_1 and mass m_1. The stability of these two particles can be achieved by two separate symmetries, for example discrete: $Z_2 \otimes Z_2'$ or continuous: $U(1)' \otimes U(1)''$, [71, 83, 88]. For now we assume that the dark matter in the universe is dominated by the heavy component, χ_0, which has no tree-level interaction with the SM but rather interacts with the lighter one through a contact operator, $\mathcal{L}_{01} = \frac{1}{\Lambda^2}\overline{\chi}_0\chi_1\overline{\chi}_1\chi_0$, figure 3.1, center panel. We will see later how this is no longer an assumption but rather a consequence. Since we are interested in incorporating the self interaction of dark matter and since the heavy state is the dominant dark matter we will assume that the SIDM only takes place among the heavy states for simplicity. Therefore, throughout this chapter we will allow χ_0 to acquire self interaction in the range: $0.1\,\mathrm{cm}^2/\mathrm{g} < \sigma_{00}^{\mathrm{self}}/m_1 < 1\,\mathrm{cm}^2/\mathrm{g}$ which is a favored range by simulation and observation as we argued in the previous section, figure 3.1, left panel. Moreover, due to the large mass splitting between the two dark states, when the process $\chi_0\,\chi_0 \to \chi_1\,\chi_1$ takes place, the particle χ_1 acquires a large kinetic energy and becomes relativistic or boosted.

The lighter component, χ_1, on the other hand is charged under a gauge group $U(1)_V$ that lives in the dark sector with a new massive vector gauge boson denoted by V that has a mass m_V. The dark gauge group then interacts with the SM through a kinetic mixing term with the photon and is parameterized by ϵ, a mixing parameter: $\mathcal{L} = -\frac{\epsilon}{2}V_{\mu\nu}F^{\mu\nu}$ where $V_{\mu\nu}$ and $F_{\mu\nu}$ are respectively the field strength tensor for the dark gauge boson and the SM photon. The massive gauge boson V is widely known as the dark photon since it mixes with the SM photon. In fact, this mixing is a consequence of an original mixing between the dark gauge group and the $U(1)_Y$ of the SM. For full details of such mixing, please refer to Refs. [102–108]. With this consideration, a tree-level interaction between χ_0 and any electrically charged particle in the SM is allowed though suppressed by the small parameter ϵ. In this thesis we will focus our efforts on the interaction with the electrons only, this process is diagrammatically represented in figure 3.1, right panel.

There are two important questions here. First: *how the abundance of dark matter is considered in such a model?* In the previous chapter, we have reviewed how a generic dark matter composed of only one species evolves and freezes out in the early universe. But our scenario here is a little different, we have two species of dark matter instead. Therefore, instead of describing the evolution only by one Boltzmann equation, one would solve two coupled Boltzmann equations representing the two species. The differential equations are coupled due to the interaction between the two dark states. Eventually both states do freeze out through a mechanism known as assisted freeze out [71, 83]. It has been numerically verified that as long as the annihilation cross sections: $\langle \sigma v \rangle_{11 \to \mathrm{SM\,SM}} \gg \langle \sigma v \rangle_{00 \to 11}$ then the ratio $\Omega_{\chi_1}/\Omega_{\chi_0}$ is very small. For example the abundance of χ_0 is estimated to be

$$\Omega_{\chi_0} \simeq 0.2 \left(\frac{5 \times 10^{-26} \mathrm{cm}^3/\mathrm{s}}{\langle \sigma_{00 \to 11} v \rangle} \right). \tag{3.1}$$

In addition, the abundance of the lighter species could be a few orders of magnitude smaller than the heavier one, see Ref. [71] for more details. We also remark that, indeed our model satisfies $\langle \sigma v \rangle_{11 \to \mathrm{SM\,SM}} \gg \langle \sigma v \rangle_{00 \to 11}$ and hence the dark matter is dominated by the heavy state naturally without a need for an assumption [88]. The other question is: *how can we probe this type of dark matter?* By construction, the interaction, $\chi_0\, \chi_0 \to$ SM SM, is suppressed by loop process and mixing parameter making it almost impossible to be detected directly. In fact, this is an excellent advantage. This way the heavy state which makes up the majority of dark matter in the universe remarkably evades the strong constraints from direct detection. Therefore, in order to probe this model we would rely on the interaction $\chi_1\,\chi_1 \to \mathrm{SM\ SM}$.

As we mentioned before, we are interested in studying interaction with electrons only. This interaction takes place as one t-channel diagram and can be represented by the following operator

$$\mathcal{L}_{\rm int} = \left(g_e^V \bar{e}\gamma^\mu e + g_{\chi_1}^V \bar{\chi}_1\gamma^\mu\chi_1\right) V_\mu. \tag{3.2}$$

The parameter g_e^V ($g_{\chi_1}^V$) denotes the interaction coupling between the massive gauge boson, V, and the electron (χ_1). Let us remark that the electron coupling parameter is related to the mixing parameter as $g_e^V = \epsilon e$ where e is the electric charge. Therefore, any analysis or conclusion drawn on the coupling parameter can be linearly recast on the mixing parameter. We chose this convention to make generalization more straightforward when we consider different models of dark matter later. The model has effectively 5 free parameters: the self interaction, the couplings which always appear as a multiplication of each other and the masses.

$$\text{model parameters} = \left\{\sigma_{00}^{\rm self}, g_e^V g_{\chi_1}^V, m_0, m_1, m_V\right\}. \tag{3.3}$$

In fact there is also an additional parameter, Λ, the scale associated with the contact operator. However its value is always adjusted to match the dark matter required abundance as dictated by the annihilation cross section of the heavy states which we fix to: $\langle\sigma_{00\to11}v\rangle = 3\times10^{-26}\mathrm{cm}^3/\mathrm{s}$ in the entire analysis of this chapter. To be specific, in this chapter we only consider one particular mass hierarchy: $m_0 > m_1 > m_V$ and generalize this case to more general scenarios later. As a benchmark point (BMP), we consider the following:

$$\text{BMP}:\ \ g_e^V = 3\times10^{-5}, g_{\chi_1}^V = 0.5\ \text{ and }\ m_V = 15\,\mathrm{MeV}. \tag{3.4}$$

The self interaction is fixed to two values according to the favored range, $\sigma_{00}^{\rm min} = 0.1\mathrm{cm}^2/\mathrm{g}$ and $\sigma_{00}^{\rm max} = 1\mathrm{cm}^2/\mathrm{g}$.

3.3 Experimental Details

We mainly consider detection prospects at the deep underground neutrino experiment (DUNE) as well as Super-K(SK)/Hyper-K(HK) [89]. DUNE has a deep underground far detector in Sanford South Dakota that is composed of 4 modules of liquid argon time projection chambers (LArTPC). Though its primary mission is not dark matter detection, it is a great experiment to probe such a dark matter model. As we will show in the next sections, DUNE will prove capable of detecting a possible signal emerging from pair annihilation of two heavy dark matter states into two lighter ones at the center of the galaxy or at the center of the Sun. One great advantage of DUNE is the fact that it will utilize a very good angular resolution as well as particle identification capability allowing it to probe smaller energies while reducing background when signal has a specific direction. We will compare our results with water based detectors that use Cherenkov radiation such as SK and HK. The basic specifications of these three detectors that are relevant to our analysis are summarized in table 3.1.

Generically, BDM at the detector will roughly behave like a neutrino due to the boost factor coming from the mass splitting though its mass is higher. Therefore, any neutrinos such as atmospheric, solar or from muon decay are potential background for BDM. Background from solar neutrinos dominate below 20 MeV, an energy that is already below the experimental thresholds. Muons on the other hand do not radiate in SK/HK and subsequently decay into neutrinos leading to background in the 30 to 50 MeV range. Notice that SK and HK have a greater energy threshold which can be lowered in general. However, this in return will worsen the energy and angular resolution. In any way, we consider the threshold energy to be 100 MeV to avoid muon decays [83]. The particle identification capability helps DUNE in distinguishing muon background and hence we use an energy threshold of $E_{\text{th}} = 30$ keV [111].

We use a conservative count on the number of background events at SK by considering both sub-GeV and multi-GeV events for a period of time of 10.7 years resulting in 7,755

	Volume (kTon)	E_{th} (MeV)	θ_{res}	Running Time (years)
SK [109]	22.5	100	3°	~ 18
HK [110]	560	100	3°	
DUNE [111]	$40 - 50$	30	1°	

Table 3.1: Comparison between the three different neutrino experiments in terms of volume, V_{exp}, energy threshold, E_{th} and angular resolution, θ_{res}. In our analysis, we use two examples of DUNE volume since its volume is planned to increase in 3 stages in increment of 10 kTon starting with two modules of 10 kTon LAr [112], therefore we consider 20 kTon (DUNE20) and 40 kTon (DUNE40).

events [113]. Then we can parameterize the background count as

$$\frac{N_{\text{BG,SK}}^{\text{all sky}}}{\Delta T} = \frac{923}{\text{year}} \frac{V_{\text{exp}}}{22.5\,\text{kTon}}. \tag{3.5}$$

This also applies to HK. On the other hand, according to the GENIE neutrino Monte-Carlo software, the expected number of background events in DUNE is [90]

$$\frac{N_{\text{BG,DUNE}}^{\text{all sky}}}{\Delta T} = \frac{128}{\text{year}} \frac{V_{\text{exp}}}{10\,\text{kTon}}. \tag{3.6}$$

Since we are going to focus only on two sources of dark matter: the galactic center and the Sun, we do not need to include the all-sky background. We therefore estimate the background based on the geometrical size of the source in the sky. For example the Galactic center corresponds to a cone with a half angle $\theta_C \sim 10°$. The Sun in principle is a point like source but conservatively we consider background within a cone of half angle $\theta_C = 1°$. The detection of BDM from the Sun as an effectively point-like source is more pronounced at DUNE since its angular resolution is $\theta_{\text{res}} = 1°$ in contrast to SK/HK whose angular resolution is poor leading to a higher number of background events. We summarize the estimated number of background events in table 3.2.

	DUNE20	DUNE40	SK	HK
GC	2 with 10°	4 with 10°	7.01 with 10°	174 with 10°
Sun	0.02 with 1°	0.04 with 1°	0.632 with 3°	15.7 with 3°

Table 3.2: Estimated annual number of background events from two sources at the three experiments.

3.4 The Galactic Center as a Source

In this section we study the detectors sensitivity for a signal emerging from the galactic center (GC) as an annihilation of heavy states to lighter states, $\overline{\chi}_0\,\chi_0 \to \overline{\chi}_1\,\chi_1$. The lighter states, the BDM, will then travel through the galaxy and interact with electrons in the detector according to $\chi_1\,e^- \to \chi_1\,e^-$.

3.4.1 BDM Galactic Flux and Signal

The differential flux, $\Phi_{\rm GC}$, with respect to a solid angle, Ω, and the energy of the BDM particle, E_1, from the GC is provided in Ref. [83] as

$$\frac{d\Phi_{\rm GC}}{d\Omega\,dE_1} = \frac{r_{\rm Sun}}{16\pi}\left(\frac{\rho_0}{m_0}\right)^2 \langle\sigma_{00\to 11}v\rangle\, J\frac{dN_1}{dE_1}, \tag{3.7}$$

where $r_{\rm Sun} = 8.33$ kpc is the distance from the GC to the Sun, $\rho_0 = 0.3\,{\rm GeV/cm^3}$ is the local dark matter density and J is a factor defined as

$$J(\theta) = \int_{\rm l.o.s} \frac{ds}{r_{\rm Sun}}\left(\frac{\rho(r(s,\theta))}{\rho_0}\right)^2, \tag{3.8}$$

which is responsible for integrating the dark matter density along the line of sight (l.o.s) from the GC. The density, $\rho(r(s,\theta))$, defines the dark matter profile for the galactic halo with the coordinate distance $r(s,\theta) = \sqrt{r_{\rm Sun}^2 + s^2 - 2\,s\,r_{\rm Sun}\cos\theta}$ where θ is the angle between the GC-Earth and the l.o.s direction and s is the l.o.s distance from earth to the GC. We take the galactic halo profile to be the NFW profile [8] [115, 116]. Finally, the last factor of equation (3.7), dictates the energy spectrum distribution of BDM particles after the annihilation of heavy states. We assume it follows a mono-energetic spectrum governed by the mass, m_0, given that the two heavy states roughly annihilate with relatively low velocity, $\frac{dN_1}{dE_1} = 2\delta\left(E_1 - m_0\right)$. It has been estimated in Ref. [90] that the flux from the GC within a cone of angle $\theta_C = 10^\circ$ is

$$\Phi_{\rm GC}^{10^\circ} \simeq 4.7 \times 10^{-8}\ {\rm cm}^{-2}\ {\rm s}^{-1} \times \left(\frac{\langle \sigma_{00\to 11} v\rangle}{3\times 10^{-26}\ {\rm cm}^3/{\rm s}}\right)\left(\frac{20\,{\rm GeV}}{m_0}\right)^2 . \tag{3.9}$$

Though this approximation is useful, we use the full expression in equation (3.7) in our results later. Now that we know how to estimate the flux, we can now estimate the number of BDM signal, $N_{\rm sig}^{\rm GC}$,

$$N_{\rm sig}^{\rm GC} = \Delta T N_{\rm target} \Phi_{\rm GC}^{\theta_C}\, \sigma_{1e}. \tag{3.10}$$

The first three factors on the right hand side of the above equation are respectively the exposure time of the experiment, the number of target electrons within the detector and the GC flux due to a cone of angle θ_C. The quantity, σ_{1e}, is the total cross section due to BDM scattering off free-at-rest detector electrons: $\chi_1\, e^- \to \chi_1\, e^-$ which at tree level has only one t-channel diagram depicted by the right panel of figure 3.1.

Before proceeding, it is important to note that the electrons within the detector are not generically free particles. They indeed are bound to the detector atoms. However, there are two reasons to justify free-at-rest treatment of electrons. First, in order to detect the BDM, the scattered electron energy has to be sufficiently greater than the threshold energy of detectors which are tens of MeV, far above the electron mass. The maximum electron energy, $E_e^{\rm max}$, can be derived from basic kinematics when the incoming BDM momentum is

---

[8] It might be more realistic to consider a profile that respects the fact that heavy states are SIDM particles. However, it has been shown that profiles based on SIDM in the region of our interest is comparable to NFW, see for example Ref. [114].

parallel to the outgoing one as:

$$E_e^{\max} = m_e \, \frac{(E_1 + m_e)^2 + (E_1^2 - m_1^2)}{(E_1 + m_e)^2 - (E_1^2 - m_1^2)}. \tag{3.11}$$

Note that, the energy E_1 is fixed equal to the mass m_0 due to tho mono-energetic assumption above. Therefore the maximum electron energy is dictated by only two parameters. To insure signal detection, $E_e^{\max}$ has to be sufficiently greater than $E_{\rm th}$. That means, roughly, $m_0/m_1 > \mathcal{O}(10)$ is needed for a minimal signal. The second reason is that the effects that describe the ionization of electrons manifest itself on what is known as the ionization form factor, which is relevant in the keV electron recoil region. In our case with a 10 MeV BDM mass we have order of 100 MeV energy far above this scale. In a nutshell, the BDM we are considering here leads to very high recoil electron energies and consequently to very suppressed atomic effects. Finally, there are other scenarios in our model where interesting low electron recoil signals are possible. We will delay the discussion of such scenarios until the next chapter in which we provide a detailed study of the atomic physics effects such as the ionization form factor and prove why such a free-at-rest electron assumption is valid here.

3.4.2 Detection Prospects

In this subsection we focus on the sensitivity of the three detectors, SK, HK and DUNE in detecting BDM from the GC. We do that by estimating the signal significance which we take as [9]

$$\sigma = \sqrt{2\left(N_{\rm sig} + N_{\rm BG}\right)\log\left(1 + \frac{N_{\rm sig}}{N_{\rm BG}}\right) - 2N_{\rm sig}}. \tag{3.12}$$

Here the number of signal events is estimated by equation (3.10) and the background is provided in table 3.2. However, before we explore what sensitivity is expected let us estimate

---

[9] This is a result of taking the log-likelihood ratio of signal and background assuming their number of events follow a Poisson distribution, see for example Ref. [117].

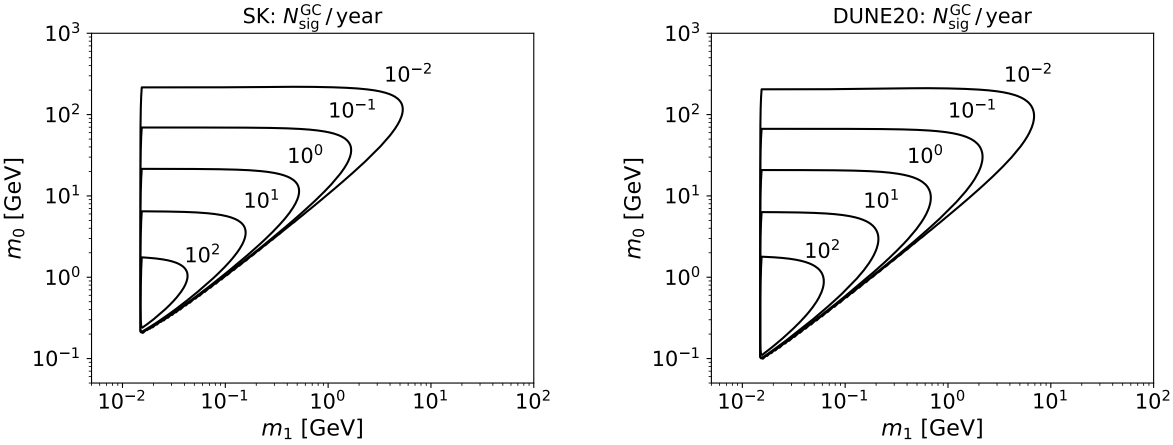

Figure 3.2: Annual number of BDM signal events expected from the GC at SK on the left and DUNE20 on the right. The numerical label above each contour indicates the minimum annual $N_{\rm sig}^{\rm GC}$ that any point in a parameter space enclosed by the same contour will produce.

the number of BDM signal events one would expect annually per detector. We will adopt the BMP defined in equation (3.4) and we will compare SK (22.5 kTon of H2O) to DUNE20 (20 kTon of LAr). In terms of number of signal events, comparison with HK and DUNE40 is straightforward, for example events in HK are scaled by its volume ratio with respect to SK and DUNE40 will be scaled by its volume ratio with respect to DUNE20.

In figure 3.2 we present the annual number of BDM signal events for SK and DUNE20 on the left and right panel respectively. We observe the similarity in the overall behavior of the contour shapes. For example, the left side of the contours always respect the fact that $m_1 > m_V$ which we chose earlier as a case study. We will generalize this case in the next chapter and explore some other interesting parameter space. The top edge of the contours are related to the GC flux that decreases with increasing m_0 mass. This also explains why the number of signal events decreases while moving towards the outermost contour. The right diagonal edge represents the mass splitting between heavy and light dark states, $m_0 > m_1$. But as we can see the slope is greater than 1, which means in addition to $m_0 > m_1$, the scattered electron should have an energy enough to cause a signal above the threshold energy $E_{\rm th}$. That means the maximum scattered energy which is solely determined by the masses m_0

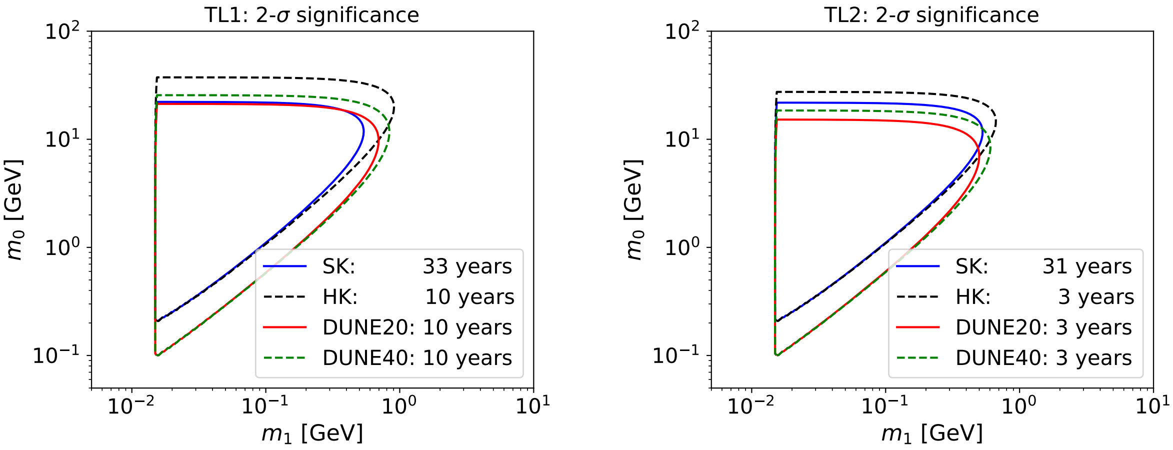

Figure 3.3: Two-σ significance comparison between all four detectors considering TL1 and TL2 on left and right panel respectively. SK, HK, DUNE20 and DUNE40 are represented by solid blue, dashed black, solid red and dashed green respectively.

and m_1 as described by equation (5.4) should be greater than E_{th}. As we argued before, m_0 has to be roughly greater than $\mathcal{O}(10)m_1$ subject to the threshold energy of a given detector. In fact, there is a slight difference in the slopes of contours representing DUNE20 and those representing SK due to the difference in the threshold energies of the two detectors. Also, the bottom corner in the right plot is smaller than that of the left one giving DUNE20 extra advantage to probe the parameter space of small masses due to its smaller threshold energy. Finally, both DUNE20 and SK are almost comparable with more possibility for DUNE20 to probe a slightly wider parameter space due to its lower threshold energy. Now we turn to the question of the signal sensitivity. DUNE and HK are future experiments which are compared to SK that has been collecting data for almost 18 years now. According to Ref. [112], DUNE will start collecting data in 2026 with 20 kTon volume i.e., DUNE20 and about 3 years later DUNE40 will be available. That means, realistically, by the time DUNE20 starts data collection, SK would have been collecting data for about 23 years. We would like to assume two scenarios: timeline 1 (TL1) assumes DUNE20 starts collecting data as planned and runs for 10 years. That means, we are comparing 10 years worth of data at DUNE20 vs 33 years at SK. The second timeline (TL2) DUNE takes longer time to construct and less time to run, for example 10 years of construction and 3 years of running. That means DUNE20 will have 3 years worth of data vs 31 years of data for SK. For straightforward comparison we treat both HK and DUNE40 on an equal footing with DUNE20 in both timelines.

Figure 3.3 compares the sensitivity of the different detectors at the two timelines TL1 and TL2. The contours represent the 2-σ significance i.e., when equation (3.12) is equal to 2. Both plots show the great capability of DUNE in general when compared to SK/HK. The left panel shows that DUNE20 with a running time less than one third of that of SK is more capable of constraining the parameter space. This is certainly because of the comparability of the annual number of signal events while background events are much smaller at DUNE20 due to its great angular resolution and particle identification capability. Even if we consider TL2 on the right panel, DUNE20 provides a very comparable result to SK though they cover two slightly different parts of the parameter space.

3.5 The Sun as a Source

In this section we focus on the BDM signal and take the Sun as a source. The Sun in fact is a very interesting source, though the BDM flux may be suppressed due to its small mass when compared to the GC, its shorter distance and geometrical consideration as a point-like source provides a very unique signal. For example, when a detector has a great angular resolution, all one needs to do is to point the detector into the direction of the Sun leading to almost no atmospheric neutrino background.

3.5.1 BDM Solar Flux and Signal

The general treatment here is similar to that of the galactic center, for example the number of signal events is estimated in a similar manner as in equation (3.10) however with different flux this time. In contrast to GC whose dark matter halo profile is well-explored and hence makes the flux estimation straightforward, one needs to study the BDM solar flux differently.

We need to first study the evolution of dark matter in the Sun and quantify its presence by properly accounting for the different effects such as capture rate, annihilation rate and self interaction. According to Ref. [88], the BDM solar flux is considered as:

$$\frac{d\Phi_{\text{Sun}}}{dE_1} = \frac{\Gamma^{\chi_0}}{4\pi R_{\text{Sun}}^2}\frac{dN_1}{dE_1}, \tag{3.13}$$

where R_{Sun} is the distance between Earth and the Sun and the last factor on the right side is treated in a similar manner as before: $\frac{dN_1}{dE_1} = 2\delta\left(E_1 - m_0\right)$. In order to estimate the solar flux, we need to properly consider the BDM solar annihilation rate, C_{a}, which is defined through $\Gamma^{\chi_0} = \frac{C_{\text{a}}}{2}N_{\chi_0}^2\left(t_\odot\right)$ where $N_{\chi_0}\left(t_\odot\right)$ is the number of heavy state particles that are captured inside the Sun and evolved throughout the age of the Sun, $t_\odot$. According to Ref. [118]

$$\frac{dN_{\chi_0}}{dt} = C_{\text{c}} + \left(C_{\text{s}} - C_{\text{e}}\right)N_{\chi_0} - \left(C_a + C_{\text{se}}\right)N_{\chi_0}^2. \tag{3.14}$$

There are five parameters in the above equation that account for the different effects of dark matter evolution in the Sun: first, C_{c} is the capture rate of dark matter due to the gravitational potential of the Sun which depends on the amount of dark matter in the solar neighborhood, the higher this parameter the higher the number of dark matter captured inside the Sun. Second, C_{s} is the capture rate due to the fact that a sizable self interaction is considered among χ_0's. Third C_{e} is an evaporation rate due to scattering of dark matter with nuclei in the Sun and the minus sign is to indicate that dark matter will decrease when this parameter is high. Fourth, C_{se} is the evaporation rate due to self interaction, the opposite of C_{c}. Finally, C_{a} dictates the production of BDM in the Sun and hence it is a crucial parameter to estimate the BDM solar flux. For definition of these parameters please refer to Ref. [88] and references therein. The solution of such equation is achieved by an initial condition $N_{\chi_0}(t = 0) = 0$ and characterized by a time scale at which dark matter reach an equilibrium between accumulation (C_{c} and C_{s}) and dissipation (C_{e}, C_{se} and C_{a}). It has been shown [88] that allowing a minimum amount of self interaction among heavy

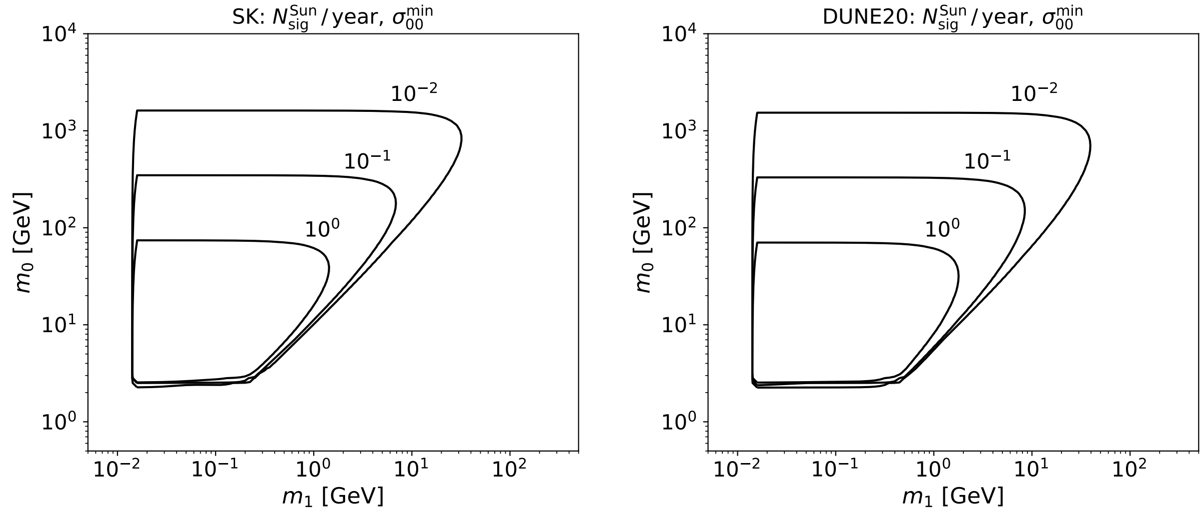

Figure 3.4: Annual number of BDM signal events expected from the Sun at SK on the left and DUNE20 on the right with $\sigma_{00}^{\rm min}$. The numerical label above each contour indicates the minimum annual $N_{\rm sig}^{\rm Sun}$ that any point in the parameter space enclosed by the same contour will produce.

states increases the number of dark matter particles in the Sun by a few order of magnitudes and it is increased even more if a maximum self interaction is considered. Once the flux is estimated, the number of BDM signal events at detector has this familiar form as before

$$N_{\rm sig}^{\rm Sun} = \Delta T N_{\rm target} \Phi_{\rm Sun}\, \sigma_{1e}. \tag{3.15}$$

3.5.2 Detection Prospects

Let us now examine the annual number of BDM signal events we can expect from the Sun. We will do this for SK and DUNE20 making generalization to HK and DUNE40 a matter of volume scaling. In figure 3.4 we present the annual number of BDM signals for SK on the left panel and for DUNE20 on the right panel. Overall both experiments are comparable to each other and similar remarks can be made about their shapes as in subsection 3.4.2. The major difference in the contour shapes between those of the GC and those here is in the bottom edge. This is mainly related to the evolution of heavy states in the Sun. The number of heavy states in the Sun, N_{χ_0}, is heavily dependent on the mass m_0, see figure

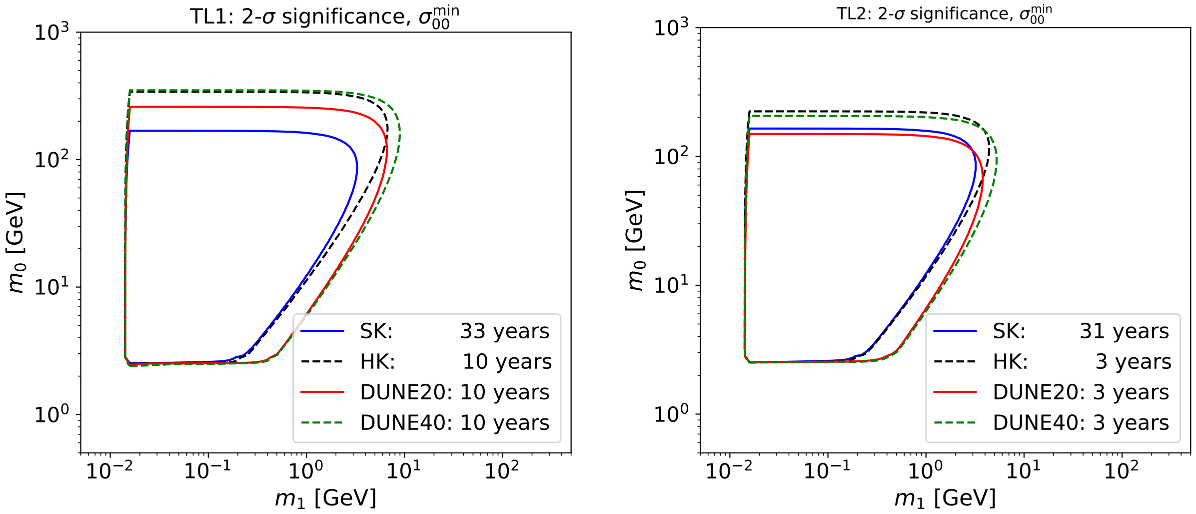

Figure 3.5: Two-σ significance comparison between all four detectors considering TL1 and TL2 on left and right panel respectively in detecting BDM from the Sun. SK, HK, DUNE20 and DUNE40 are represented by solid blue, dashed black, solid red and dashed green respectively. Here we assume minimum amount of self interaction.

2 in Ref. [88]. With a BMP similar to ours, N_{χ_0} drops significantly while decreasing m_0 to somewhere around a few GeV which is consistent with what we see in figure 3.4. Note that, we only assumed a minimum amount of self interaction, $\sigma_{00}^{\rm min}$, in fact the annual signal increases by roughly a factor of 100 if we use $\sigma_{00}^{\rm max}$ instead. Similarly as before, we estimate the sensitivity reach to all of the four detectors considering two possible timelines. In figure 3.5 (3.6), we present the parameter space that would be reached with a 2-σ significance by the four detectors assuming $\sigma_{00}^{\rm min}$ ($\sigma_{00}^{\rm max}$) self interaction. In both figures left panel and right panel represent TL1 and TL2 respectively. What we observe generally is that DUNE20 could outperform SK even in a pessimistic scenario such as TL2. With only 3 years of running, DUNE20 indeed proves better than SK with 31 years worth of data. This is mainly attributed to DUNE's excellent angular resolution which is a factor of 3 smaller than that of SK/HK. This excellent resolution is very important in rejecting background when studying point-like sources such as the Sun as we can see in table 3.2. This point can be more clearly demonstrated by comparing HK (560 kTon) to DUNE40 (40 kTon). In the Sun case, DUNE is always better than HK even though HK is 14 times greater in terms of volume. The

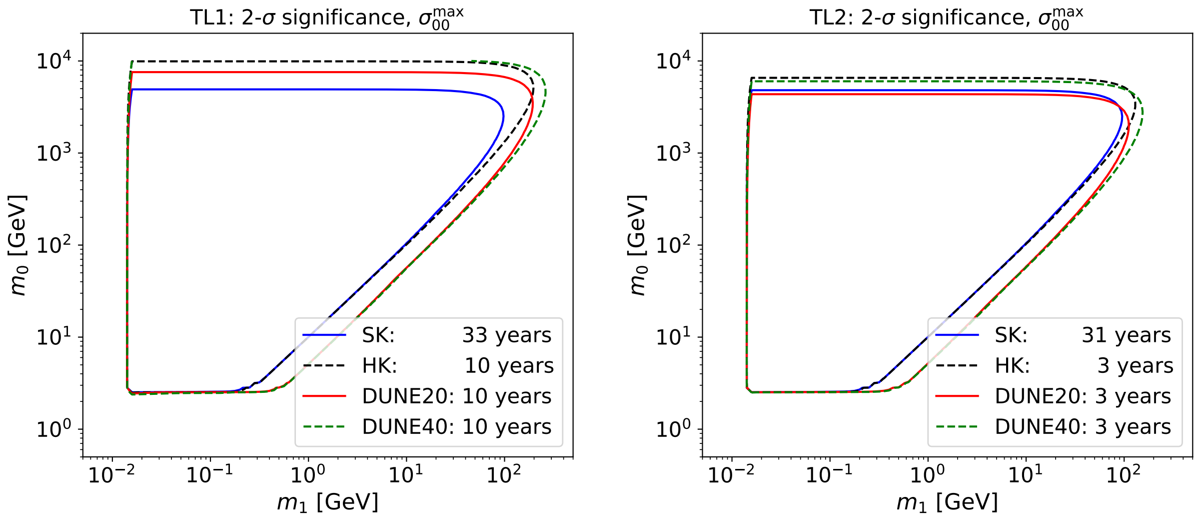

Figure 3.6: Two-σ significance comparison between all four detectors considering TL1 and TL2 on left and right panel respectively in detecting BDM from the Sun. SK, HK, DUNE20 and DUNE40 are represented by solid blue, dashed black, solid red and dashed green respectively. Here we assume maximum amount of self interaction.

effect of angular resolution proves significant in point-like sources. On the other hand, if we consider GC such as in figure 3.3 we see that HK and DUNE40 are complementary to each other since they cover slightly different parts of the parameter space.

3.6 Discussion

Before we summarize this chapter it is exciting to note that the SK collaboration had conducted an analysis on experimental data to study and set limits on BDM in general [119]. The analysis was carried out on 161.9 kiloton-years worth of data. As a benchmark value, the collaboration considered $m_1 = 200$ MeV, $g^V_{\chi_1} = 0.5$ and $m_V = 20$ MeV. The results were presented as a 90% confidence interval upper limit on the parameter space given by a (m_0, ϵ) plane which we roughly reproduce in figure 3.7.

In this chapter we studied a simple multi-component dark matter with two particles having a mass splitting such that $m_0 > m_1$. The heavy particle was taken as a dominant dark component in the universe. It has no direct interaction with the SM and hence evades

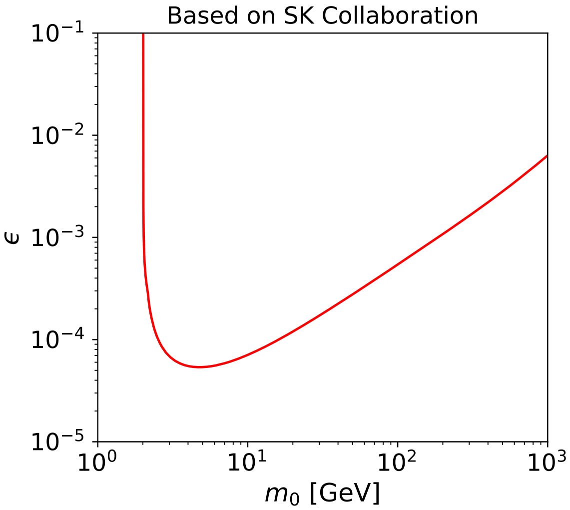

Figure 3.7: A rough reproduction of the results presented by the SK collaboration based on the discussion of the previous section.

the stringent limit from direct detection experiments. The annihilation of χ_0's into χ_1's makes the latter boosted due to the sufficient mass difference between the two. We considered the GC and the Sun as two possible sources of BDM and studied their detection prospects via interaction with electrons at deep underground neutrino detectors. We took the current SK and compared it to the future DUNE20, DUNE40 and HK detectors while considering two timelines of data taking. When compared to SK, we found that DUNE20 is very comparable (and sometimes better) even if we considered a very pessimistic timeline. DUNE in general is capable of probing more parameter space than SK/HK due to its lower energy threshold, excellent angular resolution and particle identification capabilities. These properties make DUNE a great detector to study point like sources. For example, DUNE40 had proven to outperform HK when studying BDM from the Sun even given that its volume is 14 times smaller than that of HK.

In the next chapter, we will relax the condition that the mass difference: $m_0 > \mathcal{O}(10)m_1$ to just $m_0 > m_1$. As we argued in subsection 3.4.1, this brings into the calculation important atomic physics effects due to electron binding energy and atomic structure.

Chapter 4

Low Energy Electron Recoil in the Dark Matter Electron Scattering

Now that we showed in the previous chapter one particular scenario of BDM: $m_0 > m_1 > m_V$, with one particular model: fermionic dark matter and vector mediator, it is of an interest to generalize our discussion to broader scenarios. Our previous treatment is only valid if one considers high electron recoil energy. In this chapter we provide a generalized treatment in which atomic physics effects such as binding energy and atomic structures are taken into consideration. Though our approach can be applied to any atom, we will take xenon (Xe) and argon (Ar) as examples when presenting numerical results. We start by introducing the basic kinematic setup and introduce our notation in section 4.1, we then discuss the differential cross section including atomic effects in section 4.2 and finally provide the ionization form factor in section 4.3 by comparing relativistic vs non-relativistic as well as studying different potentials and different dark matter mediators.

4.1 Basic Kinematics Setup

Here, we discuss the kinematics of a generic dark matter particle denoted by DM of mass m_1 scattering off an electron that is bound to an atom. The kinematics is different from that of free scattering and a special treatment should be carried out. We will attempt to provide a general overview and derive some basic relations. The interaction is assumed to

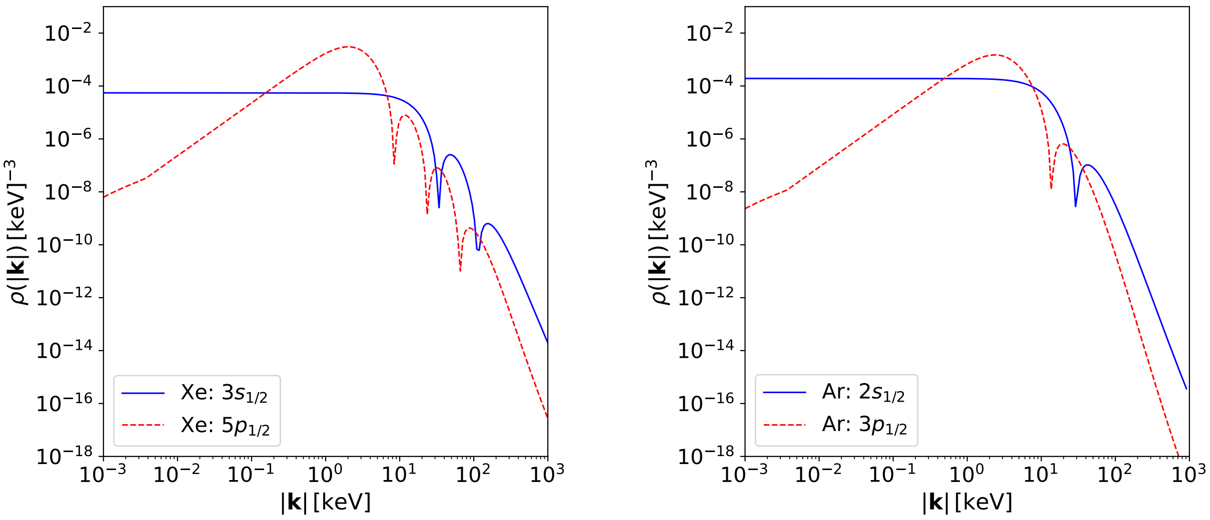

Figure 4.1: Relativistic electron momentum density, left: for $3s$ and $5p_{1/2}$ of Xe atom and right: for $2s$ and $3p_{1/2}$ of Ar atom.

be an elastic scattering as follows:

$$\mathrm{DM}(p)\ e(k) \to \mathrm{DM}(p')\ e(k'). \tag{4.1}$$

Where the momenta are defined as

$$p = (E_1;\ \mathbf{p}), \quad p' = (E_1';\ \mathbf{p}'), \quad k = (E_e;\ \mathbf{0}), \quad \text{and} \quad k' = (E_e';\ \mathbf{k}'). \tag{4.2}$$

How do we justify the choice of the electron being at rest? First of all electrons in the atom have arbitrary momenta, $\mathbf{k}$, and their magnitudes can be very high. However, the probability of having very large momenta is very small. In fact, it can be shown by looking at the momentum distribution density of electrons, $\rho(\mathbf{k})$. This density is defined as the the product of the bound electron wave function with its complex conjugate in momentum space. For spherically symmetric potentials, the density turns out to be spherically symmetric as well, $\rho(\mathbf{k}) = \rho(|\mathbf{k}|)$. In figure 4.1 we show the momentum density as a function of the magnitude of the electron momentum for two representative shells of the Xe and Ar atoms. We notice that the momentum density falls rapidly around 10 keV and the majority of electrons have relatively small momenta. Therefore, if the dark matter particle has a momentum of MeV order then $|\mathbf{k}|/|\mathbf{p}| \lesssim 10^{-2}$ and such an assumption is valid.

Before scattering, the electron is bound to the atom with energy

$$E_e = m_e - |E^B_{n\ell}|, \tag{4.3}$$

where $E^B_{n\ell}$ is the atomic binding energy which depends on the principal (orbital) quantum number n (ℓ) [10]. From energy conservation, we have

$$E'_1 = E_1 + E_e - E'_e \tag{4.4}$$

The momentum transfer is $q = k' - k$ and Mandelstam variable $s = (p+k)^2$. We are interested in finding a relation between the scattered electron energy, E'_e and the magnitude of the momentum transfer vector, $|\mathbf{q}|$. We do this by expressing the Mandelstam variable, t, in two different ways. First:

$$t = q^2 = (k' - k)^2 = m_e^2 + E_e^2 - 2E_e E'_e, \tag{4.5}$$

and second:

$$t = q^2 = E_q^2 - |\mathbf{q}|^2 = (E'_e - E_e)^2 - |\mathbf{q}|^2. \tag{4.6}$$

Equating the last two equations, we get

$$|\mathbf{q}| = \sqrt{E'^2_e - m_e^2}. \tag{4.7}$$

When the incoming dark matter particle is parallel to the outgoing one $(\mathbf{p} \parallel \mathbf{p}')$ the scattered

---

[10] As we will see later, in relativistic case, the binding energy depends also on the total angular momentum j.

electron energy reaches its maximum (minimum) according to

$$2m_1^2 - 2E_1E'_1 + 2\sqrt{E_1^2 - m_1^2}\,\sqrt{{E'_1}^2 - m_1^2} = m_e^2 + E_e^2 - 2E_eE'_e. \tag{4.8}$$

The scattering electron energy that solves the above equation is denoted by ${E'_e}^{\max/\min}$ and expressed as:

$${E'_e}^{\max/\min} = \frac{(E_e + E_1)\,(\mathcal{E}^2 + m_e^2) \pm \sqrt{(E_1^2 - m_1^2)\,\left[\mathcal{E}^2 - m_e(m_e + 2m_1)\right]\,\left[\mathcal{E}^2 - m_e(m_e - 2m_1)\right]}}{2(\mathcal{E}^2 + m_1^2)}, \tag{4.9}$$

where we defined $\mathcal{E}^2 \equiv E_e(E_e + 2E_1)$. One may observe that if the electron is free before scattering, namely if $E_e = m_e$, we get:

$$\left({E'_e}^{\max}\right)_{E_e=m_e} = m_e\,\frac{(E_1 + m_e)^2 + (E_1^2 - m_1^2)}{(E_1 + m_e)^2 - (E_1^2 - m_1^2)} \qquad \text{and} \qquad \left({E'_e}^{\min}\right)_{E_e=m_e} = m_e \tag{4.10}$$

in agreement with what we expressed in equation (3.11). Equation (4.9) can be complex when the argument of the square root is negative. We would like here to extract the conditions that ensure real values of ${E'_e}^{\max/\min}$. There are two cases:

- *case 1:* if $m_1 \geq \frac{m_e}{2}$, the condition is

$$\mathcal{E}^2 \geq m_e(m_e + 2m_1). \tag{4.11}$$

- *case 2:* if $m_1 < \frac{m_e}{2}$, the condition is

$$\mathcal{E}^2 \geq m_e(m_e + 2m_1) \quad \text{or} \quad \mathcal{E}^2 \leq m_e(m_e - 2m_1). \tag{4.12}$$

One thing we want to emphasize here is that these conditions on $\mathcal{E}^2$ are actually conditions on the electron energy before scattering and hence applies on the Binding energy, $|E^B_{n\ell}|$. In other words, once the parameters such as masses and energies are fixed, one would find a set of allowed energy levels $\{n\ell\}_{\text{allowed}}$ that leaves equation (4.9) real.

4.2 Differential Cross Section

After introducing the kinematics, let us now focus on a particular case where the dark matter particle is a fermion interacting with the electron through a t-channel exchange of a vector boson of mass m_V. The couplings of the vector boson to dark matter and electron are respectively g_1^V and g_e^V. The Lorentz-invariant matrix element is expressed in terms of the Mandelstam variables as

$$|\mathcal{M}|^2 = 2\left(g_1^V g_e^V\right)^2 \; \frac{2m_1^4 + 2m_e^4 + 4m_1^2(m_e^2 - s) - 4m_e^2 s + 2s^2 + 2s\,t + t^2}{(m_V^2 - t)^2}. \tag{4.13}$$

In what follows, we would like to discuss the differential cross section inspired by a similar treatment as in Ref. [120]. But we have to remind our selves that whenever we refer to the matrix element we are implying that it is expressed in terms of $|\mathbf{q}|$ using the kinematics discussion above. For example the Mandelstam variable should appropriately be expressed in $|\mathbf{q}|$ and the maximum/minimum scattering energy of the electron $E_e'^{\,\text{max/min}}$ is translated into a maximum/minimum condition on the magnitude of the momentum transfer vector $|\mathbf{q}|^{\text{max/min}}$. With this in mind and in analogy with equation (31) in Ref. [120] we are equipped to write

$$d\sigma_{1e}^{n\ell} = \frac{1}{64\pi^2 E_1 E_1' E_e E_e'} \frac{|\mathcal{M}|^2}{v_{1e}} \frac{1}{(2\pi)^3}\, \delta(E_1' - (E_1 + E_e - E_e'))\; |f_{e_i \to e_f}(\mathbf{q})|^2 \; d^3\mathbf{q} d^3\mathbf{k}'. \tag{4.14}$$

Where, $|f_{e_i \to e_f}(\mathbf{q})|^2$ is the factor that takes into account the transition from an initial bound electron to a final free electron. It is clear that if both initial and final electron states are free the following replacement $|f_{e_i \to e_f}(\mathbf{q})|^2 \to (2\pi)^3\, \delta^3(\mathbf{p} + \mathbf{k} - \mathbf{p}' - \mathbf{k}')$ will result in the free elastic scattering case. We will discuss this factor in more detail shortly. But before going any farther, let us first integrate out the delta function. Note that

$$\delta(E_1' - (E_1 + E_e - E_e')) = \delta(\sqrt{m_1^2 + |\mathbf{p}|^2 + |\mathbf{q}|^2 - 2|\mathbf{p}||\mathbf{q}|\cos\theta} - (E_1 + E_e - E_e')). \quad (4.15)$$

Taking the derivative of the argument of the delta function with respect to θ one can simplify the above equation to

$$\delta(E_1' - (E_1 + E_e - E_e')) = \frac{E_1'}{|\mathbf{p}||\mathbf{q}|\sin\theta}\ \delta(\theta). \quad (4.16)$$

Now, we can integrate out the delta function in (4.14) with the phase space element $d\mathbf{q}^3$

$$d\sigma_{1e}^{n\ell} = \frac{|\mathbf{q}|d|\mathbf{q}|}{32\pi E_1 E_e E_e' \,|\mathbf{p}|}\ \frac{|\mathcal{M}|^2}{v_{1e}}\ \frac{1}{(2\pi)^3}\ \ |f_{e_i\to e_f}(\mathbf{q})|^2\ d^3\mathbf{k}'. \quad (4.17)$$

We now, would like to express the above relation as a differential cross section with respect to the recoil energy $E_r = E_e' - m_e$. To do so, let us use $|\mathbf{k}'| = \sqrt{2m_e E_r + E_r^2}$ and therefore $d^3\mathbf{k}' = (m_e + E_r)\,|\mathbf{k}'|\, d\Omega_{\hat{\mathbf{k}}'}\, dE_r$. With this change of variable, we re-express equation (4.17)

$$\frac{d\sigma_{1e}^{n\ell}}{dE_r} = \frac{|\mathbf{q}|d|\mathbf{q}|}{64\pi E_1 E_e\,|\mathbf{p}|\,|\mathbf{k}'|^2}\ \frac{|\mathcal{M}|^2}{v_{1e}}\ \left[\frac{2\,|\mathbf{k}'|^3}{(2\pi)^3}\ \int d\Omega_{\hat{\mathbf{k}}'}\,|f_{e_i\to e_f}(\mathbf{q})|^2\ \right]. \quad (4.18)$$

The quantity in the square bracket above is the ionization form factor and will be denoted by $|f_{ion}(E_r,\,|\mathbf{q}|)|^2$. Finally, we write equation (4.18) in an explicit form as

$$\frac{d\sigma_{1e}^{n\ell}}{dE_r} = \frac{1}{64\pi v_{1e}}\ \frac{1}{E_1 E_r(2m_e + E_r)(m_e - |E_{n\ell}^B|)\sqrt{E_1^2 - m_1^2}}\ \int_{|\mathbf{q}|^{\min}}^{|\mathbf{q}|^{\max}} d|\mathbf{q}|\ \ |\mathbf{q}|\,|\mathcal{M}|^2\,|f_{ion}(E_r,\,|\mathbf{q}|)|^2. \quad (4.19)$$

Where v_{1e} is the relative velocity between the incoming dark matter particle and the electron. Eventually, one is interested in adding the different contributions from different shells of an atom, therefore:

$$\frac{d\sigma_{1e}}{dE_r} = \sum_{n,\ell} \frac{d\sigma_{1e}^{n\ell}}{dE_r}. \quad (4.20)$$

4.3 Atomic Ionization Form Factor

Here, we would like to discuss how we approached the estimation of the ionization form factor. We review a few different approximations and categorize them into non-relativistic and relativistic approximations. Let us first restate the dimensionless form factor

$$|f_{ion}(E_r,\, |\mathbf{q}|)|^2 = \frac{2\,|\mathbf{k}'|^3}{(2\pi)^3} \int d\Omega_{\hat{\mathbf{k}}'}\, |f_{e_i\to e_f}(\mathbf{q})|^2. \tag{4.21}$$

We are now concern with how to estimate the transition factor, $|f_{e_i\to e_f}(\mathbf{q})|^2$. For now, let us continue assuming that the dark matter mediator is a vector boson and will generalize the discussion later for other types of mediators. Therefor,

$$f_{e_i\to e_f}(\mathbf{q}) = \langle e_f|e^{i\mathbf{q}\cdot\mathbf{r}}|e_i\rangle = \int d^3\mathbf{r}\,\langle e_f|\mathbf{r}\rangle\, e^{i\mathbf{q}\cdot\mathbf{r}}\,\langle \mathbf{r}|e_i\rangle = \int d^3\mathbf{r}\,\psi^*_{e_f}(\mathbf{r})\, e^{i\mathbf{q}\cdot\mathbf{r}}\,\psi_{e_i}(\mathbf{r}). \tag{4.22}$$

The approximations that we are about to discuss are similar in the fact that they all attempt to estimate the above equation but different in the way they approach the bound and free electron wave functions $\psi_{e_i}(\mathbf{r})$ and $\psi_{e_f}(\mathbf{r})$ respectively.

4.3.1 Non-relativistic Approximations

In the non-relativistic case we are considering two different approximations according to how the ionized electron wave function is assumed.

- *Plane Wave*

  The first simplest approximation is the case where the scattered or ionized electron is described by a plane wave, such a case will be denoted by PW. In this case the final electron wave function is simply characterized by its momentum, $\psi_{\mathbf{k}'}(\mathbf{r}) = \langle \mathbf{r}|\mathbf{k}'\rangle = e^{i\mathbf{k}'\cdot\mathbf{r}}$. The bound state electrons wave functions are taken to be Roothaan-Hartree-Fock (RHF) wave functions whose radial components are given as linear combination of Slater-type orbitals that are tabulated in Ref. [121]. In that case, the wave function must be characterized by the three quantum numbers as $\psi_{n\ell m}(\mathbf{r}) = \langle \mathbf{r}|n\ell m\rangle$. This allows one to express equation (4.22) as

$$f^{\mathrm{PW}}_{e_i\to e_f}(\mathbf{q}) = \int d^3\mathbf{r}\, e^{-i\mathbf{k}'\cdot\mathbf{r}}\, e^{i\mathbf{q}\cdot\mathbf{r}}\, \psi_{n\ell m}(\mathbf{r}). \tag{4.23}$$

Using plane wave expansion in terms of spherical Bessel function, j_L, and spherical harmonics, Y_L^M:

$$e^{i\,\mathbf{Q}\cdot\mathbf{r}} = 4\pi \sum_{L,M} i^L\, j_L(|\mathbf{Q}|r)\, Y_L^{M*}(\hat{\mathbf{Q}})\, Y_L^M(\hat{\mathbf{r}}), \tag{4.24}$$

equation (4.23) with $\psi_{n\ell m}(\mathbf{r}) = R_{n\ell}(r)\, Y_l^m(\hat{\mathbf{r}})$ can be written as:

$$\begin{aligned} f^{\mathrm{PW}}_{e_i\to e_f}(\mathbf{q}) = & \sum_{\ell'=0}^{\ell'=\infty} \sum_{m'=-\ell'}^{m'=+\ell'} \sum_{L=0}^{L=\infty} \sum_{M=-L}^{M=+L} (4\pi)^2 (-1)^{m'} (-i)^{\ell'} i^L\, \mathcal{F}^{\ell}_{\ell' L} \\ & \times Y_{\ell'}^{m'}(\hat{\mathbf{k}'})\, Y_L^{M*}(\hat{\mathbf{q}}) \int d\Omega_{\hat{\mathbf{r}}}\, Y_\ell^m(\hat{\mathbf{r}})\, Y_{\ell'}^{-m'}(\hat{\mathbf{r}})\, Y_L^M(\hat{\mathbf{r}}), \end{aligned} \tag{4.25}$$

where we have used $Y_{\ell'}^{m'*} = (-1)^{m'}\, Y_{\ell'}^{-m'}$ and defined $\mathcal{F}^{\ell}_{\ell' L}$ as

$$\mathcal{F}^{\ell}_{\ell' L} \equiv \int_0^\infty dr\, r^2\, R_{n\ell}(r)\, j_{\ell'}(|\mathbf{k}'|r)\, j_L(|\mathbf{q}|r). \tag{4.26}$$

The integration over the three spherical harmonics above can be performed in terms of the Wigner 3j-symbol according to.

$$\frac{\int d\Omega Y_{\ell_1}^{m_1} Y_{\ell_2}^{m_2}\, Y_{\ell_3}^{m_3}}{\sqrt{\frac{(2\ell_1+1)(2\ell_2+1)(2\ell_3+1)}{4\pi}}} = \begin{pmatrix} \ell_1 & \ell_2 & \ell_3 \\ 0 & 0 & 0 \end{pmatrix} \begin{pmatrix} \ell_1 & \ell_2 & \ell_3 \\ m_1 & m_2 & m_3 \end{pmatrix}. \tag{4.27}$$

If we return to equation (4.21), we are interested in the absolute square, $|f^{\mathrm{PW}}_{e_i\to e_f}(\mathbf{q})|^2$ as well as an integration over the solid angle of the outgoing electron [11] which takes the form $\int d\Omega_{\hat{\mathbf{k}'}} |Y_{\ell'}^{m'}(\hat{\mathbf{k}'})|^2 = 1$. With this in mind, we can now use equation (4.25) to

---

[11] Notice the major difference between the PW approximation and the other approximations below. In the PW approximation, we showed that the transition factor squared is dependent on the angles of the outgoing electron however the others are not.

express equation (4.21) as

$$
\begin{aligned}
|f_{ion}(E_r,\, |\mathbf{q}|)|^2_{\mathrm{PW}} = & \, 32|\mathbf{k}'|^3 \sum_{\ell'=0}^{\ell'=\infty} \sum_{L=|\ell-\ell'|}^{L=\ell+\ell'} \sum_{M=-L}^{M=+L} \sum_{L'=|\ell-\ell'|}^{L'=\ell+\ell'} \sum_{M'=-L'}^{M'=+L'} (i)^L (-i)^{L'} \, (2\ell+1)\,(2\ell'+1) \\
& \times \sqrt{(2L+1)\,(2L'+1)}\, \mathcal{F}^{\ell}_{\ell' L} \mathcal{F}^{\ell *}_{\ell' L'} \begin{pmatrix} \ell & \ell' & L \\ 0 & 0 & 0 \end{pmatrix} \begin{pmatrix} \ell & \ell' & L' \\ 0 & 0 & 0 \end{pmatrix} \\
& \times Y_L^{M^*}(\hat{\mathbf{q}}) Y_{L'}^{M'}(\hat{\mathbf{q}}) \sum_{m=-\ell}^{m=\ell} \sum_{m'=-\ell'}^{m'=+\ell'} \begin{pmatrix} \ell & \ell' & L \\ m & -m' & M \end{pmatrix} \begin{pmatrix} \ell & \ell' & L' \\ m & -m' & M' \end{pmatrix}.
\end{aligned}
\tag{4.28}
$$

Notice the introduction of an extra factor of 2 to account for the spin and the summation over the magnetic quantum number for the initial electron. Also notice the summation limit of the numbers L and L' in the first line which are required by the Wigner 3j-symbols in the second line to insure non-vanishing quantity. The orthogonality of the 3j-symbol:

$$
\sum_{m_1, m_2} \begin{pmatrix} \ell_1 & \ell_2 & \ell \\ m_1 & m_2 & m \end{pmatrix} \begin{pmatrix} \ell_1 & \ell_2 & \ell' \\ m_1 & m_2 & m' \end{pmatrix} = \frac{\delta_{\ell\ell'}\delta_{mm'}}{(2\ell+1)} \tag{4.29}
$$

and the addition theorem of the spherical harmonics: $\sum_{m=-\ell}^{m=+\ell} Y_\ell^m Y_\ell^{m^*} = (2\ell+1)/4\pi$, can be used in the third line to further simplify equation (4.28) to

$$
|f_{ion}(E_r,\, |\mathbf{q}|)|^2_{\mathrm{PW}} = \frac{8|\mathbf{k}'|^3}{\pi} \sum_{\ell'=0}^{\ell'=\infty} \sum_{L=|\ell-\ell'|}^{L=\ell+\ell'} \mathcal{A}^{\ell}_{\ell' L} \, |\mathcal{F}^{\ell}_{\ell' L}|^2, \tag{4.30}
$$

where we have defined

$$
\mathcal{A}^{\ell}_{\ell' L} \equiv (2\ell+1)\,(2\ell'+1)\,(2L+1) \begin{pmatrix} \ell & \ell' & L \\ 0 & 0 & 0 \end{pmatrix}^2 . \tag{4.31}
$$

For $\ell = 0$, we find our calculation for the PW approximation in a very good agree-

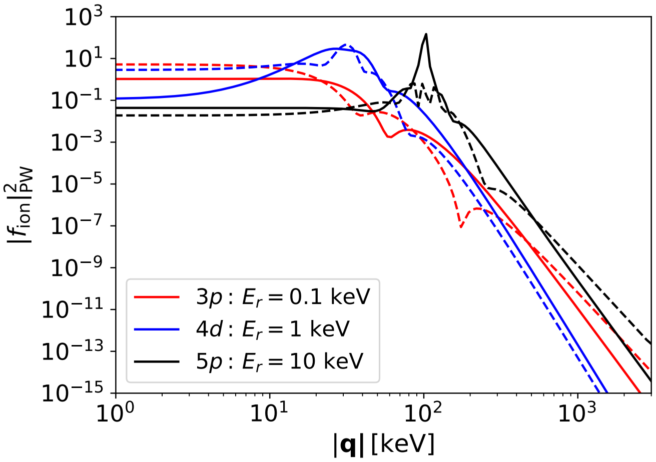

Figure 4.2: The PW approximation for the ionization form factor for a representative shells of Xe atom at different recoil energies. The solid curves represent equation (4.32) while the dashed ones represent our calculation in equation (4.30).

ment with that used in the literature such as in Refs. [120, 122, 123], however for higher ℓ, a disagreement is observed. We illustrate this disagreement in figure 4.2 for a representative shells of the Xe atom at different recoil energies. For the rest of this thesis and in consistency with the current literature, instead of equation (4.30), we will use [120, 122, 123]:

$$|f_{ion}^{n\ell}(E_r,\, |\mathbf{q}|)|^2_{\rm PW} = \frac{(2\ell+1)|\mathbf{k}'|^2}{4\pi^3|\mathbf{q}|}\int d|\mathbf{k}|\; |\mathbf{k}||\chi_{n\ell}(|\mathbf{k}|)|^2, \tag{4.32}$$

with integration limit $||\mathbf{k}'| \pm |\mathbf{q}||$. The momentum space wave function is related to the radial component of the RHF wave function as, $\chi_{n\ell}(|\mathbf{k}|) = 4\pi i^L \int drr^2 R_{n\ell}(r) j_L(|\mathbf{k}|, r)$, for more details also see Ref. [124]. As a numerical cross-check of our implementation, in figure 4.3 we consider Xe atom in the left panel and plot its $5p$ shell contribution to the ionization factor at different recoil energies. We found that the red curve is in a great agreement with figure 1 in Ref. [123]. For comparison, we also present Ar $3p$ shell on the right panel.

- *Schrödinger Continuum Energy*

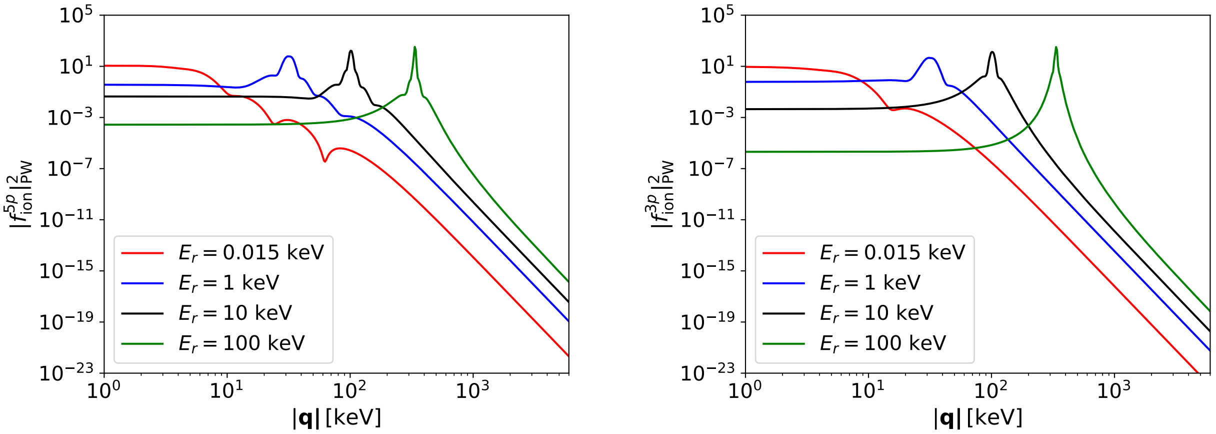

Figure 4.3: The PW ionization factor contribution from $5p$ ($3p$) shell of the Xe (Ar) atom on the left (right) panel. Different colors represent different examples of the electron recoil energy: red, blue, black and green correspond to $E_r = 0.015$ keV, 1 keV, 10 keV and 100 keV respectively. We purposefully chose the red curve to represent $E_r = 0.015$ keV to validate against existing literature, see main text.

Second, we use the same RHF bound electron wave functions as in the PW case however the ionized electron is described by continuum energy solution of the Schrödinger equation with a Coulomb-like potential [125], such a case will be denoted SCE. Even though the ionized electron is free it is still obeys the Schrödinger equation and hence carries angular quantum numbers that we will denote by $\ell' m'$. However, the energy will be a free positive parameter that is denoted by E_r. In this scenario we can write $\psi_{E_r \ell' m'}(\mathbf{r}) = \langle \mathbf{r} | E_r \ell' m' \rangle$ and the transition factor is then

$$f^{\rm SCE}_{e_i \to e_f}(\mathbf{q}) = \int d^3\mathbf{r}\, \psi^*_{E_r \ell' m'}(\mathbf{r})\, e^{i\mathbf{q}\cdot\mathbf{r}}\, \psi_{n\ell m}(\mathbf{r}). \tag{4.33}$$

Proceeding on similar manner as the PW, an expansion of $e^{i\mathbf{q}\cdot\mathbf{r}}$ into a linear combination of spherical waves is performed and the wave functions are parameterized into radial and angular component. For example $\psi_{E_r \ell' m'}(\mathbf{r}) = R_{E_r \ell'}(r) Y_{\ell' m'}(\theta, \phi)$. In contrast to the PW approximation, it can be shown that the above expression is indeed independent of the solid angle $\Omega_{\hat{\mathbf{k}}'}$. Without going into much details on the derivation, we rather refer the reader to the excellent aforementioned reference and instead write

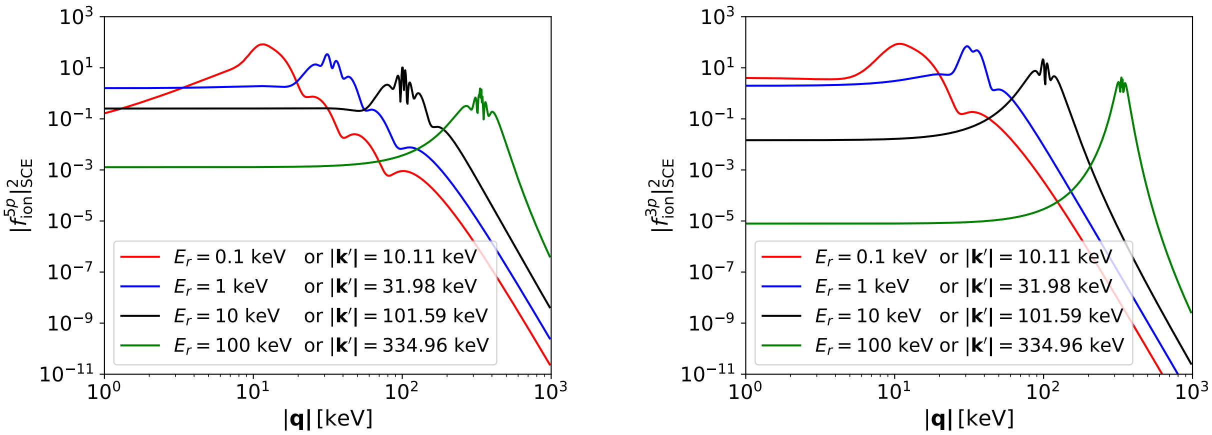

Figure 4.4: The SCE ionization form factor: $5p$ shell of Xe on the left panel and the $3p$ shell of the Ar on the right panel. Different colors represent different examples of the electron recoil energy: red, blue, black and green correspond to $E_r = 0.1$ keV, 1 keV, 10 keV and 100 keV respectively.

down the final expression factoring out a general coefficient, $\mathcal{A}^{\ell}_{\ell' L}$ for convenience. In view of equation (4.21) we have

$$|f^{n\ell}_{ion}(E_r,\, |\mathbf{q}|)|^2_{\rm SCE} = \frac{|\mathbf{k}'|^3}{\pi^2} \sum_{\ell'=0}^{\infty} \sum_{L=|\ell-\ell'|}^{\ell+\ell'} \mathcal{A}^{\ell}_{\ell' L} \left| \int_0^\infty dr\, r^2 j_L(|\mathbf{q}|r) R^*_{E_r\ell'}(r) R_{n\ell}(r) \right|^2 . \quad (4.34)$$

Both bound and free electron radial functions are provided in the same reference above and the coefficient is defined in equation (4.31). The summation over ℓ' is truncated at $\ell'_{\rm max} = 7$ given that a convergence is achieved.

In figure 4.4 we cross check our numerical implementation by presenting the ionization factor in equation (4.34) for $5p$ shell of Xe on the left and $3p$ shell of Ar on the right. We compare these results with those of Ref. [125] and find that they agree with each other overall. We emphasize here that equation (4.21) is conventionally different from the corresponding one in Ref. [125], ours is greater by a factor of 2π.

4.3.2 Relativistic Treatment: Dirac Continuum Energy

Since the previous two approximations are both non-relativistic, we are also considering a third approximation in which both bound and ionized electron are described by wave functions that are solutions to the Dirac equation in a spherically symmetric potential. We will denote this case by DCE. In what follow we will briefly discuss how the Dirac Hamiltonian is considered and in particular how did we choose the potential. For clarity, we are going to denote the potential as an effective potential $V_{\text{eff}}(r)$ where r is the distance of the electron from the center of the atom. The Hamiltonian that describes this approach is then

$$\hat{h} = \boldsymbol{\alpha} \cdot \mathbf{p} + m_e\,(\beta - 1) + V_{\text{eff}}(r) \tag{4.35}$$

where $\boldsymbol{\alpha}$ and β are the Dirac matrices in the standard representation. The wave function in general is decomposed into

$$\psi_{n\kappa m}(\mathbf{r}) = \frac{1}{r}\begin{pmatrix} P_{n\kappa}(r)\,\Omega_{\kappa m}(\hat{\mathbf{r}}) \\ iQ_{n\kappa}(r)\,\Omega_{-\kappa m}(\hat{\mathbf{r}}) \end{pmatrix}, \tag{4.36}$$

Where Ω represents the two-component spherical spinor and $P_{n\kappa}$ ($Q_{n\kappa}$) is the large (small) Dirac radial component. Note that the radial components depend on two integers n: the principal quantum number and κ: the Dirac quantum number. In addition, it depends on the absolute distance r and no spherical dependence is present. This decomposition of the wave function allows one to remove the spherical dependence when solving the eigenvalue problem. Therefore, it is safe to denote the wave function and the energy by only two quantum numbers. One then would seek a solution to the eigenvalue problem

$$\hat{h}\psi_{n\kappa} = E_{n\kappa}\psi_{n\kappa}. \tag{4.37}$$

This will lead to a coupled first order ordinary differential equation. It is important at this level to remind our selves that the eigenvalue $E_{n\kappa}$ does not include the rest mass of the electron as it is evident in the Hamiltonian above. The coupled differential equations can be solved analytically for simple potential such as $V_{\text{eff}}(r) \propto -1/r$. However, we are going to deal with potentials that take into account the nuclear size and structure of the atom which naturally lead to more complicated potential. For, this reason we will seek a numerical solution. We will consider two different approaches for the effective potential. We remind the reader, for a full description please refer to the cited references below. First, we consider a straightforward approach in which the effective potential is provided in a parameterized formulae in which the parameters are optimized and determined through a particular numerical method. We consider here two different methods.

i. *EXP*: this method [126] provides the potential in the following form

$$V_{\text{eff}}(r) = \begin{cases} -\frac{Z}{2R}\left(3 - \frac{r^2}{R^2}\right) & r < R \\ -\frac{1}{r}\{Z - N + 1 + (N-1)f(r)\} & r \geq R \end{cases} \tag{4.38}$$

where Z, N and R are the atomic number, number of electrons and $R = 2.2677 \times 10^{-5} A^{1/3}$ in Bohr radius while A is the mass number. The coefficients and the parameters of the function f given by $f(r) = \sum_{k=1}^{n_c} c_k r^{n_k} e^{-\beta_k r}$ is then variationally optimized by minimizing the expectation value of the Hamiltonian. A list of these parameters are tabulated for different atoms $Z \in [2, 88]$ and provided in Ref. [127]

ii. *ERF*: this method introduced in Ref. [128] provides another parameterized formulae for an effective potential with the form

$$V_{\text{eff}}(r) = -\frac{Z}{r} + \sum_{i=1}^{n} c_i \frac{\operatorname{erf}(\sqrt{a_i}\, r)}{r}, \tag{4.39}$$

with the parameters are optimized by minimizing a particular measure. This mea-

> sure finds the difference between an effective density function based on the above assumed potential and the Hartree-Fock density function. The optimized parameters and the optimization procedure are provided in Ref. [128]. We would like to note here that the first term in the above potential is our interpretation of what the authors of the aforementioned reference denote by bare nuclear potential.

The naming of these two methods *EXP* and *ERF* does not reflect the physics behind them but rather a convenient choice we make for later reference. Second, we consider the Dirac-Hartree-Fock-Slater (DHFS) self consistent method provided in the package `RADIAL` [129]. The potential in this method consists of three different contributions:

$$V_{\text{eff}}(r) = V_{\text{DHFS}}(r) = V_{\text{nuc}}(r) + V_{\text{el}}(r) + V_{\text{ex}}(r) \tag{4.40}$$

The first term on the right side of the above equation is the nuclear potential which takes care of the electrostatic interaction between the nucleus and the electron at a given distance r. This potential is approximated by Fermi distribution to the proton density. The second and third terms are the electric and exchange potential respectively. Both of these terms are related to the electron density $\rho(r)$ given by

$$\rho(\mathbf{r}) = \sum_{\text{OS}} = \psi^{\dagger}_{n\kappa m}(\mathbf{r})\psi_{n\kappa m}(\mathbf{r}), \tag{4.41}$$

where OS stands for occupied orbitals. The method then is concerned with finding an optimized form for the electric density which consequently gives an effective potential. The way this optimization work is to assume an in initial electric density $\rho(r) = \rho_0$ given by a parameterization of Thomas-Fermi potential of neutral atoms. This initial density allows to write an initial potential, V_0, for equation (4.40) which then enables a numerical solution to the eigenvalue problem in equation (4.37). Once the wave functions are determined a new version ρ_1 of the electric density, equation (4.41) is achieved and lead to a new version of the potential, V_1. Now the new potential that inters the eigenvalue problem is a weighted

state			Xe absolute ionization energy in atomic units (27.211 eV).				
$n_{\ell j}$	n	κ	-Z/r	[130]	$V_{\rm eff}^{ERF}$ [126, 127]	$V_{\rm eff}^{EXP}$ [128]	$V_{\rm eff}^{DHFS}$ [129]
$1_{s_{1/2}}$	1	-1	1519	1277	1261	1263	1270
$2_{s_{1/2}}$	2	-1	383.8	202.5	196.4	196.2	199.1
$2_{p_{1/2}}$	2	1	383.8	189.7	184.5	184.2	187.6
$2_{p_{3/2}}$	2	-2	368.1	177.7	172.6	172.3	175.5
$3_{s_{1/2}}$	3	-1	168.8	43.01	40.39	40.36	41.24
$3_{p_{1/2}}$	3	1	168.8	37.66	35.44	35.43	36.37
$3_{p_{3/2}}$	3	-2	164.1	35.33	33.17	33.15	34.05
$3_{d_{3/2}}$	3	2	164.1	26.02	24.48	24.50	25.39
$3_{d_{5/2}}$	3	-3	162.7	25.54	24.00	24.03	24.89
$4_{s_{1/2}}$	4	-1	94.21	8.430	7.401	7.445	7.662
$4_{p_{1/2}}$	4	1	94.21	6.453	5.649	5.701	5.909
$4_{p_{3/2}}$	4	-2	92.25	5.983	5.203	5.251	5.438
$4_{d_{3/2}}$	4	2	92.25	2.711	2.368	2.425	2.566
$4_{d_{5/2}}$	4	-3	91.65	2.634	2.296	2.353	2.488
$5_{s_{1/2}}$	5	-1	59.97	1.010	0.851	0.869	0.869
$5_{p_{1/2}}$	5	1	59.97	0.493	0.465	0.479	0.454
$5_{p_{3/2}}$	5	-2	58.97	0.440	0.422	0.434	0.403

Table 4.1: The absolute values of the ionization energy of different shells for the Xe atom comparing different types of method for estimating the potential.

average of V_0 and V_1. These steps are iterated until a convergence in the updated potentials sequence is achieved. In what follows, we would like to compare the above three different potentials $V_{\rm eff}^{EXP}$, $V_{\rm eff}^{ERF}$ and $V_{\rm eff}^{DHFS}$ in terms of the ionization energy of different orbitals of Xe and Ar atom. We emphasize that all the subsequent calculations are made using the package `RADIAL` which in addition to estimating the DHFS potential, it also solves the Dirac equation for arbitrary input potential and provides a numerical values for the eigenvalues and eigenfunctions. Therefore, for $V_{\rm eff}^{EXP}$ and $V_{\rm eff}^{ERF}$ we will use the parameterized form as explained above and for $V_{\rm eff}^{DHFS}$ we will rely on the pre-implemented DHFS method in `RADIAL`. In table 4.1 we compare the absolute ionization energy of the Xe atom shells for these three methods. Also for comparison we list out in the second column the results provided in Ref. [130]. For numerical implementation consistency we also estimate in the first column the well-known analytically estimated energies when the potential is very simple. For the third and fourth columns, we also cross checked our implementation by considering another numerical package, `dftatom` [131], that is designed to solve the eigenvalue problem in equation (4.37) and we found exact similar results. We also estimate the ionization energy for Ar and present it in table 4.2.

state			Ar absolute ionization energy in atomic units (27.211 eV).			
$n_{\ell j}$	n	κ	-Z/r	V_{eff}^{ERF} [126,127]	V_{eff}^{EXP} [128]	V_{eff}^{DHFS} [129]
$1_{s_{1/2}}$	1	-1	162.7	114.5	114.3	116.8
$2_{s_{1/2}}$	2	-1	40.72	11.09	11.16	11.52
$2_{p_{1/2}}$	2	1	40.72	8.637	8.723	9.167
$2_{p_{3/2}}$	2	-2	40.54	8.556	8.644	9.080
$3_{s_{1/2}}$	3	-1	18.08	1.046	1.082	1.063
$3_{p_{1/2}}$	3	1	18.08	0.530	0.561	0.537
$3_{p_{3/2}}$	3	-2	18.03	0.524	0.555	0.530

Table 4.2: The absolute values of the ionization energy of different shells for the Ar atom comparing different types of method for estimating the potential.

Our point of interest is to estimate the ionization form factor in a fully relativistic picture. The ionized electron is a free electron but still satisfies the eigenvalue problem (4.37), however, the energy will be a free positive continuous parameter rather a discrete quantum number. For clarity and in comparison with equation (4.36) we denote these states by the recoil energy E_r as follows:

$$\psi_{E_r\kappa m}(\mathbf{r}) = \frac{1}{r}\begin{pmatrix} P_{E_r\kappa}(r)\,\Omega_{\kappa m}(\hat{\mathbf{r}}) \\ iQ_{E_r\kappa}(r)\,\Omega_{-\kappa m}(\hat{\mathbf{r}}) \end{pmatrix}, \tag{4.42}$$

where $P_{E_r\kappa}$ ($Q_{E_r\kappa}$) is the large (small) Dirac radial component of the free state. Now, we turn into the calculation of the ionization form factor, $|f_{ion}^{n\kappa}(E_r,\,|\mathbf{q}|)|^2$. Before doing so, we need to specify the form of transition factor as in equation (4.22) which will have a very similar form as SCE case in equation (4.33)

$$f^{\text{DCE}}_{e_i\to e_f}(\mathbf{q}) = \int d^3\mathbf{r}\, \psi^{\dagger}_{E_r\ell' m'}(\mathbf{r})\, e^{i\mathbf{q}\cdot\mathbf{r}}\, \psi_{n\ell m}(\mathbf{r}). \tag{4.43}$$

Keep in mind that the Dirac wave functions are four-dimensional vectors and the operator in the middle decides the form of the interaction. In this current discussion we still assuming that the dark matter mediator is a vector boson that interacts with electron through a vector coupling. In this case the operator in the middle is just $e^{i\mathbf{q}\cdot\mathbf{r}}$ times a 4-by-4 identity matrix which will leave the large and small component unmixed when performing the dot product above. Therefore, and without spending much time on how to factorize the angular component that is coming either from the spherical spinors Ω or spherical wave expansion of $e^{i\mathbf{q}\cdot\mathbf{r}}$, the transition factor squared is found in Ref. [130] as:

$$\left| f^{\text{DCE}}_{e_i\to e_f}(\mathbf{q}) \right|^2_{\text{V}} = \sum_{\kappa'} \sum_{L} C^{L}_{\kappa\kappa'}\, (R_P + R_Q)^2, \tag{4.44}$$

with subscript on the left denoting vector interaction and the radial integrals R_P and R_Q given by

$$R_P = \int_0^\infty P_{E_r\kappa'} P_{n\kappa} j_L(|\mathbf{q}|\, r) dr \tag{4.45}$$

and

$$R_Q = \int_0^\infty Q_{E_r\kappa'} Q_{n\kappa} j_L(|\mathbf{q}|\, r) dr, \tag{4.46}$$

where $C^{L}_{\kappa\kappa'}$ defined in Ref. [130] is an overall angular coefficient that is independent of the solid angle $\Omega_{\hat{\mathbf{k}}'}$ and $\kappa\,(\kappa')$ is the Dirac quantum number for bound (free) state. Note that the summation over κ' is in fact a summation over $\{\ell' j'\}$ where for every value of ℓ' there is a set of allowed values of j'. In estimating the radial integrals, the radial functions for free and bound states are outputs of the package `RADIAL`. We then perform the integral numerically over r starting from 0 and stops at some maximum value. For illustration, let us denote the integrand generically by $\mathcal{I}(r)$. The free state radial functions tend to oscillate rapidly at high

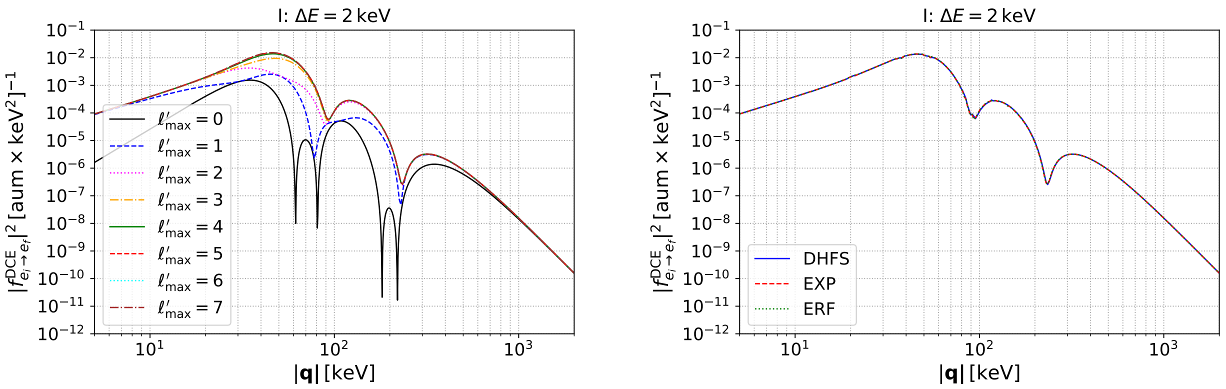

Figure 4.5: Transition factor for iodine $3s$ shell as a function of the momentum transfer at $\Delta E = 2$keV. Left: we test the convergence of the summation over κ' by fixing one potential method. Right we compare the transition factor given different methods for the potential.

distances while the bound state ones approaches zero. This allows the peak of oscillation of the overall integrand to become smaller with distances. We perform the integral over segments of r such that each segment is given by one Bohr radius, a_0, as

$$R = \sum_{i=0}^{i_{\max}} \int_{ia_0}^{(i+1)a_0} \mathcal{I}(r) dr. \tag{4.47}$$

This summation is truncated when the ratio between the term at which we truncate and the entire summation is less than 10^{-5}. In what follows we test our calculations by comparing our results to [130]. For comparison we use the full deposited energy ΔE that is responsible to free an electron with an absolute bound energy $|E^B_{n\kappa}|$ to a free state of energy E_r. In figure 4.5 we consider the transition factor for iodine energy shell $3s$ and $\Delta E = 2$keV as a function of $|\mathbf{q}|$. On the Left we show that by varying the upper limit $\ell'_{\max}$ for the summation over κ' in equation (4.44) while fixing the potential V^{ERF}_{eff}. On the right side we chose $\ell'_{\max} = 7$ and consider different methods for the potential. The unit aum stands for atomic unit of momentum. We see a very good agreement with [130] and a consistency between the different potential methods. In figure 4.6 on the left side we see the consistency between the different potential methods persist for high momentum transfer values. On the right side we see the different contributions of many energy shells of Xe using one potential method,

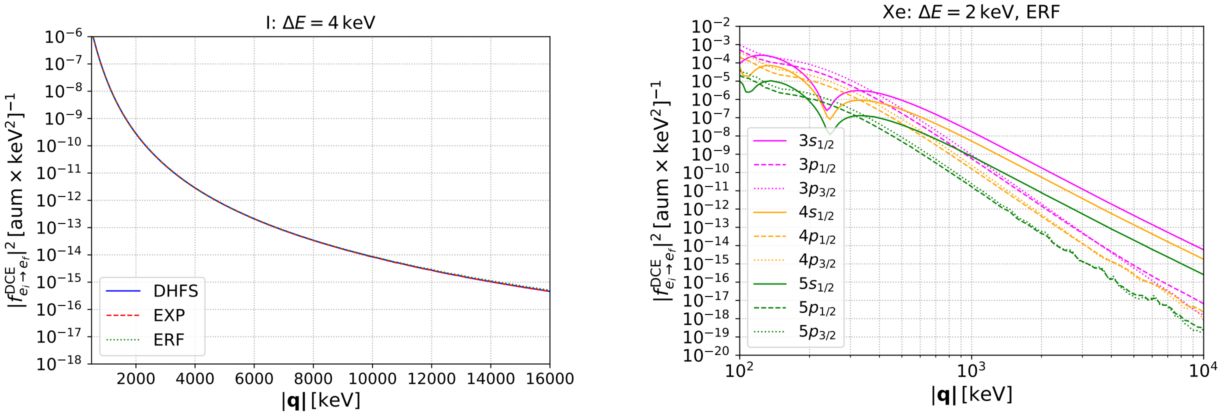

Figure 4.6: Left iodine $3s$ transition factor as a function of the momentum transfer at $\Delta E =$ 4keV for different potential methods. Right: Xe ionization form factor with contributions at $\Delta E =$ 2keV from different energy shells.

V_{eff}^{ERF}. We notice that at high momentum transfer some deeper energy shells such as $3s$ has higher contribution than others. In fact, we can also consider the case when the dark matter mediator interacts with electron through scalar (γ^0), axial-vector (γ_5) or pseudo-scalar ($\gamma^0\gamma_5$) with the matrices in the previous brackets replacing the identity matrix in equation (4.43) as in Ref. [130]. They are respectively given as

$$\begin{aligned} \left|f^{\text{DCE}}_{e_i \to e_f}(\mathbf{q})\right|^2_{\text{S}} &= \sum_{\kappa'} \sum_{L} C^L_{\kappa\kappa'} \left(R_P - R_Q\right)^2 \\ \left|f^{\text{DCE}}_{e_i \to e_f}(\mathbf{q})\right|^2_{\text{A}} &= \sum_{\kappa'} \sum_{L} D^L_{\kappa\kappa'} \left(R_{PQ} - R_{QP}\right)^2 \\ \left|f^{\text{DCE}}_{e_i \to e_f}(\mathbf{q})\right|^2_{\text{P}} &= \sum_{\kappa'} \sum_{L} D^L_{\kappa\kappa'} \left(R_{PQ} + R_{QP}\right)^2, \end{aligned} \tag{4.48}$$

with $D^L_{\kappa\kappa'}$ is an angular coefficient while R_{PQ} and R_{QP} are the radial integrals

$$R_{PQ} = \int_0^\infty P_{E_r\kappa'} Q_{n\kappa} j_L(|\mathbf{q}|\, r) dr \tag{4.49}$$

and

$$R_{QP} = \int_0^\infty Q_{E_r\kappa'} P_{n\kappa} j_L(|\mathbf{q}|\, r) dr, \tag{4.50}$$

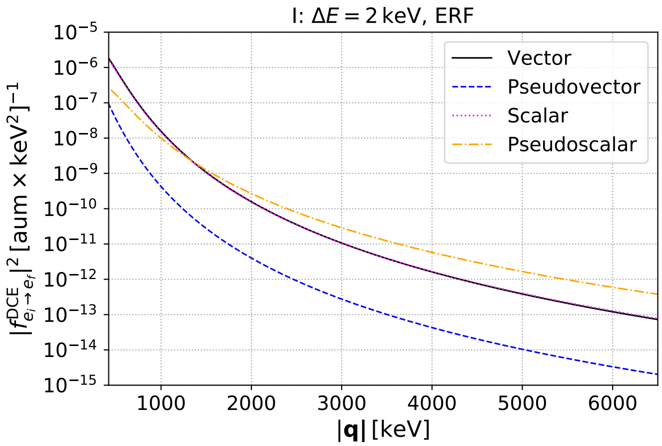

Figure 4.7: Different transition factors that correspond to different mediator types.

respectively. As may have been anticipated, the presence of the γ_5 is responsible for the mixing between the small and large Dirac component in the last two lines of equation (4.48). In figure 4.7 we compare transition factors that correspond to different mediators. We see that pseudo-scalar case has larger values when compared to others at high momentum transfer. The one corresponds to the axial-vector is very suppressed while vector and scalar are very similar. In fact, and in order to understand the differences between transition factors corresponding to different mediators, one has to observe the radial integrals in equation (4.46) and (4.50). The key is the relative contribution between the large (P) and small (Q) Dirac components. For example, in the case of the vector and scalar mediators, there are two terms proportional to $R_P R_Q$ and R_Q^2 where the former has Q^2 and the latter has Q^4 dependence. These terms are suppressed when compared to the last one that depends on the large Dirac component, R_P^2 which has 4 powers of P. For the case of axial-vector and pseudo-scalar all terms have same powers of P and Q and hence the suppression of axial-vector case is attributed to relative minus sign. We would like to emphasize that, this was a rough argument to understand the differences between the transition factors. One has to keep in mind that things are much more complicated and a sophisticated analysis has to be considered. For example, the role of the spherical Bessel function must be understood since it tends to oscillate very rapidly at large qr. Moreover, the ionized electron whose wave

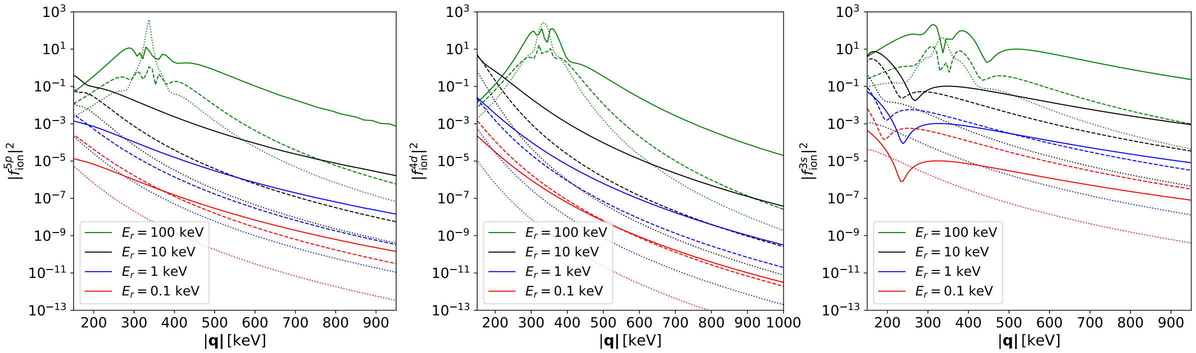

Figure 4.8: Xe ionization form factor as a function of the momentum transfer at different electron recoil energies represented by different colors. Left, center and right panels correspond to $5p$, $4d$ and $3s$ shells respectively. The dotted, dashed and solid line represent the PW, SCE and DCE approximations restrictively. Different colors represent different examples of the electron recoil energy: red, blue, black and green correspond to $E_r = 0.1$ keV, 1 keV, 10 keV and 100 keV respectively.

functions is a solution to the Dirac equation in the continuum positive energy oscillates very rapidly at large radii.

To conclude the ionization form factor estimation, it is very important to compare the aforementioned three approximations to each other. First, let us write the form factor in its final form for relativistic case

$$\left|f_{ion}^{\kappa\ell}(E_r\,|\mathbf{q}|)\right|^2_{\mathrm{DCE},\,i} = \frac{|\mathbf{k}'|^3}{\pi^2}\,\left|f_{e_i\to e_f}^{\mathrm{DCE}}(\mathbf{q})\right|^2_i, \tag{4.51}$$

where the subscript i corresponds to the different 4 mediators we considered above. Notice that the DCE is similar to the SCE in which the transition factor squared is independent of the angles of the outgoing electron in contrast to the PW.

Now in comparing the three approximation PW, SCE, and DCE we would like to focus on the regions where the relativistic corrections are more pronounced and take vector mediator as an example. These regions of course depend on the value of the recoil electron energy and in our case they are roughly greater than $|\mathbf{q}| \backsim 100$ keV. In figure 4.8 we compare the dependence of $|f_{ion}(E_r,\,|\mathbf{q}|)|^2$ for the three approximations on the momentum transfer at different values of recoil energies of the ionized electrons. We show this for the $5p$, $4d$ and

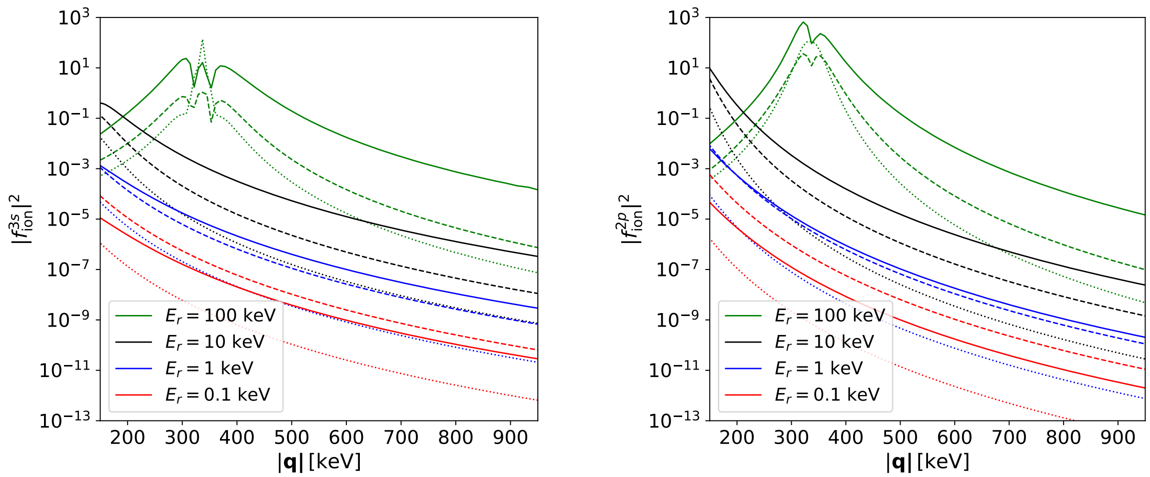

Figure 4.9: Ar ionization form factor as a function of the momentum transfer at different electron recoil energies represented by different colors. Left (right) panel corresponds to $3s$ ($2p$) shell. The dotted, dashed and solid line represent the PW, SCE and DCE approximations restrictively. Different colors represent different examples of the electron recoil energy: red, blue, black and green correspond to $E_r = 0.1$ keV, 1 keV, 10 keV and 100 keV respectively.

$3s$ shells of Xe. The dotted, dashed and solid line respectively represents the PW, SCE and DCE approximation while different colors represent different electron recoil energies. We repeat the same thing in figure 4.9 but this time for $3s$ and $2p$ shells of Ar. In the relativistic case, when referring to a shell by its principal and orbital angular momentum quantum numbers, $n\ell$, we in practice assume the addition of contributions from different total angular momentum quantum numbers. For example, $3p = 3p_{1/2} + 3p_{3/2}$. We see overall that the DCE approximation is more dominant at high momentum transfer. As has been noted in Refs. [132, 133], we see in some cases such as those of small recoil energies, the difference between the different approximations could be few order of magnitudes. This is a very important point, especially when the physics of interest has high momentum transfer.

4.3.3 The Free Particle Limit of the Ionization Form Factor

In this subsection we are interested in the asymptotic form of the ionization form factor. This will validate a very important assumption we made in the previous chapter when we treated

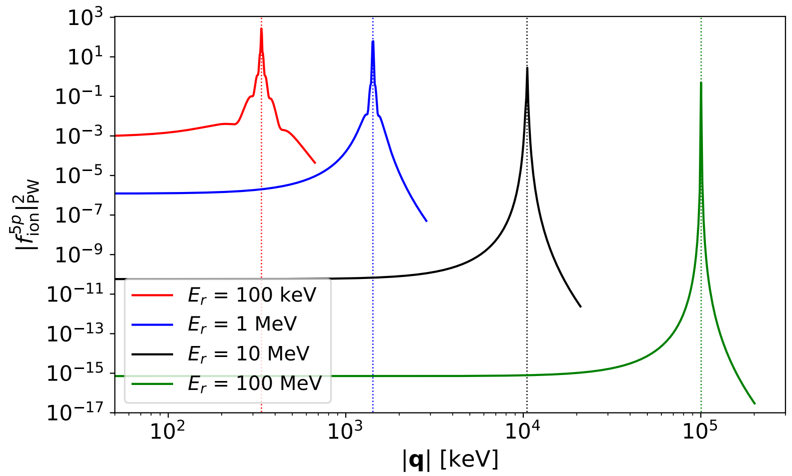

Figure 4.10: The asymptotic behavior of the ionization form factor as the recoil energy is increased. Different colors represent different examples of the electron recoil energy: red, blue, black and green correspond to $E_r = 100$ keV, 1 MeV, 10 MeV and 100 MeV respectively. The dotted lines represent the corresponding $|\mathbf{k}'|$ values given by $\sqrt{2m_eE_r + E_r^2}$.

electrons as free particles. In equation (4.14) we started with a free scattering differential cross section while making the following replacement

$$\delta^3(\mathbf{p} + \mathbf{k} - \mathbf{p}' - \mathbf{k}') \to |f_{e_i \to e_f}(\mathbf{q})|^2/(2\pi)^3, \tag{4.52}$$

to account for the atomic effects by introducing the transition factor, $|f_{e_i\to e_f}(\mathbf{q})|^2$. We later defined the ionization form factor in equation (4.21). The above replacement is needed when we lower the recoil energy, however as we increase the recoil energy the above replacement is flipped:

$$\text{as } E_r \text{ increases}: \;\; |f_{e_i \to e_f}(\mathbf{q})|^2/(2\pi)^3 \to \delta^3(\mathbf{p} + \mathbf{k} - \mathbf{p}' - \mathbf{k}'). \tag{4.53}$$

That means the transition factor and consequently the ionization form factor should asymptotically behave as a delta function as we increase E_r. To gain such high recoil energy the incoming momentum $\mathbf{p}$ should be very high which allows one to effectively set $\mathbf{k}$ to zero, i.e., the delta function becomes $\delta^3(\mathbf{q} - \mathbf{k}')$. Therefore we anticipate:

$$\text{as } E_r \text{ increases}: \;\; |f_{ion}(E_r,\, |\mathbf{q}|)|^2 \to 8\pi\, |\mathbf{k}'|^3\, \delta^3(\mathbf{q} - \mathbf{k}'). \tag{4.54}$$

In figure 4.10 we demonstrate the asymptotic behavior of the ionization form factor by taking $5p$ shell of Xe and using the PW approximation as an example. We see that as we increase the recoil energy, indeed the form factor behave as a delta function centered at the $|\mathbf{k}'|$ as expected by equation (4.54). This is on the other hand validates the assumption we made in the previous chapter when we considered the electron as free particles given that a high recoil energy is required because of the threshold energy of the experiments. Such an assumption shall not be valid when we consider low recoil energy in the next chapters.

In this chapter, we have introduced a very general formalism for the elastic scattering differential cross section of a generic dark matter particle with the electron. We incorporated effects from binding energy as well as the atomic structure by introducing the transition factor and hence the ionization form factor. We explored few different approximations for the ionization form factor and categorized them into non-relativistic and relativistic ones. When investigating the relativistic case, we have explored different ways of representing the potential energy of the atoms and achieved great agreement between them as well as cross checked against existing literature. We took the mediator of the dark matter to be a vector boson as an example throughout the chapter and later generalized the discussion to other mediators such as scalar, pseudo-scalar and axial-vector. We also compared the different approximations for the ionization form factor to each other and observed the significant corrections at high momentum transfer due to relativistic treatment. Finally, we presented a short discussion on the asymptotic behavior of the ionization form factor by showing the energy scale at which it behaves as a delta function justifying an assumption made earlier in the previous chapter.

Chapter 5

Boosted Dark Matter at Direct Detection Experiments: Low Energy Electron Recoil

In this chapter, we generalize the discussion of BDM we had earlier on two fronts. First, we relax the condition $m_0 > m_1 > m_V$ to just $m_0 > m_1$ and allow the degenerate scenario. Second, we generalize dark vector mediator and fermionic BDM to a class of 7 different models. We begin the chapter by introducing the models and study their energy spectral shapes in terms of benchmark points which encapsulate different features of the kinematics. We then incorporate the low recoil treatment introduced in the previous chapter and investigate the impact of the ionization form factor on the BDM phenomenology. In terms of detection, and complementary to chapter 3, we focus on low electron recoil experiments and take the recent XENON1T excess as an example. We discuss how the interpretation of such an excess can be explained by several BDM model and moreover how the ionization form factor can severely change the results.

5.1 Shape Analysis

5.1.1 The Models

Since we are in place to discuss low electron recoil as a result of scattering by a fast moving dark matter particle, it is of an interest to study the recoil energy spectrum of different simple dark matter scenarios. These scenarios will be classified according to the particle and interaction nature of both the dark matter particle and the mediator. We will begin our

case	mediator	DM	$\mathcal{L}_{int}$	$\overline{\lvert\mathcal{A}\rvert}^2$
VF	V_μ	χ_1	$\left(g_e^V \bar{e}\gamma^\mu e + g_\chi^V \bar{\chi}_1 \gamma^\mu \chi_1\right) V_\mu$	$8m_e \left\{m_e \left(2E_1^2 - 2E_1 E_r + E_r^2\right) - \left(m_e^2 + m_1^2\right) E_r\right\}$
VS	V_μ	φ_1	$\left(g_e^V \bar{e}\gamma^\mu e + g_\varphi^V \varphi_1^* \partial^\mu \varphi_1 + \text{h.c.}\right) V_\mu$	$8m_e \left\{2m_e E_1 \left(E_1 - E_r\right) - m_1^2 E_r\right\}$
AF	A_μ	χ_1	$\left(g_e^A \bar{e}\gamma^\mu \gamma^5 e + g_\chi^A \bar{\chi}_1 \gamma^\mu \gamma^5 \chi_1\right) A_\mu$	$8m_e \left\{m_e \left(2E_1^2 - 2E_1 E_r + E_r^2\right) + \left(m_e^2 + m_1^2\right) E_r\right\}$ $+32 m_e^2 m_1^2 \left(2\frac{E_r^2 m_e^2}{m_A^4} + 2\frac{E_r m_e}{m_A^2} + 1\right)$
PF	a	χ_1	$\left(i g_e^a \bar{e}\gamma^5 e + i g_\chi^a \bar{\chi}_1 \gamma^5 \chi_1\right) a$	$4m_e^2 E_r^2$
PS	a	φ_1	$\left(i g_e^a \bar{e}\gamma^5 e + i g_\varphi^a m_1 \varphi_1^* \varphi_1\right) a$	$8m_e m_1^2 E_r$
SF	ϕ	χ_1	$\left(g_e^\phi \bar{e} e + g_\chi^\phi \bar{\chi}_1 \chi_1\right) \phi$	$4m_e \left(E_r + 2m_e\right)\left(2m_1^2 + m_e E_r\right)$
SS	ϕ	φ_1	$\left(g_e^\phi \bar{e} e + g_\varphi^\phi m_1 \varphi_1^* \varphi_1\right) \phi$	$8m_e m_1^2 \left(E_r + 2m_e\right)$

Table 5.1: Scenarios of simple dark matter interaction with electron.

description by considering a simple t-channel scattering of a dark matter particle that is either a fermion χ_1 or a complex scalar φ_1. The exchange particle or the mediator is either vector V_μ, axial-vector A_μ, pseudo-scalar a or scalar ϕ. We are concerned with only renormalizable Lorentz invariant interactions. Therefor, from the set of two dark matter particles $\{\chi_1, \varphi_1\}$ that interacts with electron e through the set of mediators $\{V_\mu, A_\mu, a, \phi\}$ there are 7 different scenarios for the interaction that will be denoted generically by a Lagrangian $\mathcal{L}_{\text{int}}$. For clarity and for future reference, we abbreviate these 7 scenarios by two characters, the first represents what type of mediator and the second represents what type of dark matter. For example, AF, means that dark matter is considered to be a fermion while the mediator is axial-vector. The coupling constants are denoted by g sub-scripted by the external particle type and super-scripted by the mediator type. For example, the coupling constant of fermion dark matter with the scalar mediator is denoted by g_χ^ϕ. In table 5.1 we summarize these different scenarios and provide a list of the corresponding interaction Lagrangian in the fourth column. Note that we chose the dimensionful couplings of both PS and SS cases to be normalized to the dark matter mass.

For the purpose of the shape analysis, let us assume that the electron is free and at rest given that dark matter is fast enough. In that case the differential cross section with respect to the electron recoil energy is given by equation (4.19) with the free limit provided in equation (4.54) and negligible binding energy:

$$\frac{d\sigma_{1e}}{dE_r} = \frac{1}{64\pi}\,\frac{1}{|\mathbf{k}'|^2 m_e (E_1^2 - m_1^2)} \int_{|\mathbf{q}|^{\min}}^{|\mathbf{q}|^{\max}} d|\mathbf{q}|\;\; |\mathbf{q}|\, |\mathcal{M}|^2\, \frac{8\pi|\mathbf{k}'|^3\,\delta(|\mathbf{q}| - |\mathbf{k}'|)}{4\pi|\mathbf{q}|^2}, \tag{5.1}$$

where we have used $v_{1e} = \sqrt{1 - m_1^2/E_1^2}$, $|\mathbf{k}'|^2 = 2m_e E_r + E_r^2$ and the fact that the matrix element squared is spherically symmetric in $\mathbf{q}$. Using $\lambda\left(s, m_e^2, m_1^2\right) = 4m_e^2(E_1^2 - m_1^2)$, this will lead to a familiar form

$$\frac{d\sigma_{1e}}{dE_r} = \frac{m_e\,|\mathcal{M}|^2}{8\pi\,\lambda\left(s, m_e^2, m_1^2\right)}. \tag{5.2}$$

Finally, and to make comparison between different models transparent we use:

$$\frac{d\sigma_{1e}}{dE_r} = \frac{\left(g_j^i g_e^i\right)^2 m_e}{8\pi\lambda\left(s, m_e^2, m_1^2\right)\left(2m_e E_r + m_i^2\right)^2}\overline{|\mathcal{A}|}^2, \tag{5.3}$$

where $i \in \{V, A, a, \phi\}$, $j \in \{\chi, \varphi\}$, and $\lambda(x, y, z) = (x - y - z)^2 - 4yz$. Where we have used $\overline{|\mathcal{A}|}^2$ to denote the averaged matrix element squared without the couplings and the propagator. The differential cross section above has an end point that is given merely by the kinematics according to

$$E_r^{\max} = \frac{2m_e|\mathbf{p}|^2}{s}\,, \tag{5.4}$$

where the Lorentz invariant variable $s = m_1^2 + m_e^2 + 2m_e E_1$ and $|\mathbf{p}|$ is the magnitude of the incoming dark matter momentum that is given by the on-shell condition. Note that the above equation is equivalent to (3.11) but written in a more compact form. Also note that the λ factor in the denominator can be simplified as

$$\lambda\left(s, m_e^2, m_1^2\right) = 4m_e^2|\mathbf{p}|^2. \tag{5.5}$$

We summarize the expressions for the amplitudes of the different scenarios in the last column of table 5.1. Finally it is important to note that there are 4 free parameters for a given model

$$\text{model parameters} = \{g^i_j g^i_e, E_1, m_1, m_i\}. \tag{5.6}$$

In fact, the number of independent parameters are 5, but because the couplings are always a multiple of each other we consider them as one parameter. What we are interested in now is to investigate the recoil electron spectral shapes of the aforementioned scenarios. For simplicity, let us consider normalized differential cross section and hence we do not worry about the couplings at least for now. In order to study all the physics aspects of a particular model, a 4-dimensional scan over the model parameters should be performed. Since this is a tedious and inefficient approach, we rather focus on a set of a representative benchmark points (BMP) that reflects different physics aspects. Before deciding what these BMPs are, it is helpful to think about some general kinematics such as the velocity of dark matter, v_{1e} and $E_r^{\max}$. We are considering fast moving dark matter, i.e., v_{1e} should be relatively close to the speed of light, $v_{1e} \gtrsim 0.1$ c. In addition to this, we are interested in a relatively low recoil electron energy and in particular those whose $E_r^{\max} \gtrsim 1$ keV for reasons that will become obvious when we study dark matter detection phenomenology later. As can be easily verified, both v_{1e} and $E_r^{\max}$ are fully determined by two model parameters, m_1 and E_1. To illustrate the parameter space of interest, in figure 5.1 we perform a scan over two model parameters m_1 and E_1 by plotting the curves that correspond to $E_r^{\max}$ and v_{1e}. The black dotted, dashed and solid lines show the velocity of dark matter $v_{1e}/c = 0.1, 0.9$ and 0.99 respectively while solid blue, red and green show the $E_r^{\max}$ curves. The maximum recoil curves all exhibit some linear asymptotic behavior that they become parallel to the v_{1e} curves at high mass and energy. Moreover, cases with relatively low $E_r^{\max}$ will asymptotically align with $v_{1e} = 0.1$ c curve with a slope equivalent to one. These interesting regions are those corresponding to the degeneracy between dark matter masses, i.e., $m_0/m_1 \approx 1$. This ratio increases once we start moving diagonally to the top left part of the parameter space away from the black

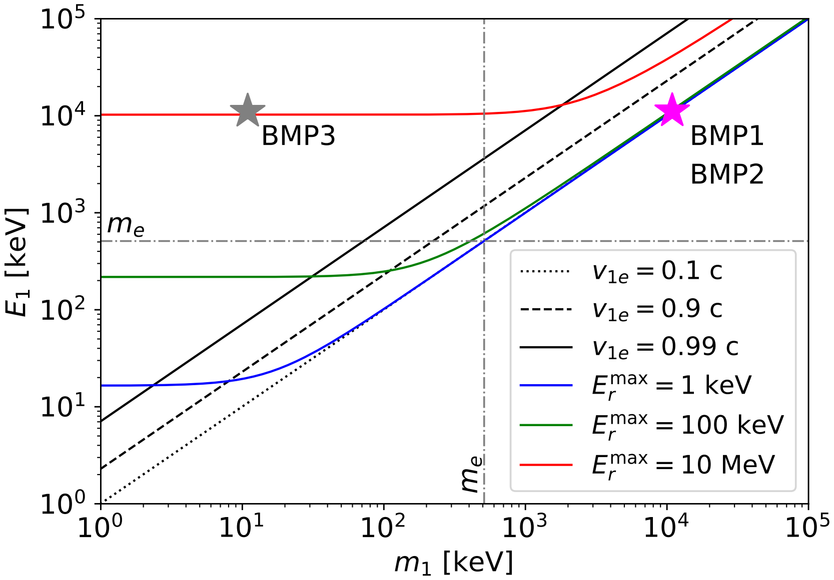

Figure 5.1: Parameter space of m_1 and E_1 showing the curves that correspond to $E_r^{\max} = 1$ keV, 10 keV and 10 MeV in solid blue, green and red respectively. Also shows the curves that correspond to $v_{1e}/c = 0.1, 0.9$ and 0.99 in black dotted, dashed and solid respectively.

dotted line. For our purpose and as we have discussed above, we will focus on the region that is located roughly to the left of the blue curve to ensure both $v_{1e} \gtrsim 0.1$ c and $E_r^{\max} \gtrsim 1$ keV.

5.1.2 Case Studies: Vector Mediator and Fermionic Dark Matter

Since we are concerned with the normalized electron spectral shapes, in addition to m_1 and E_1 we should also consider m_i. Also remember $E_1 = m_0$. In the first two cases we investigate the low-boosted region around the magenta star on the right side of figure 5.1 by looking at different mediator masses. In the last case we explore the high-boosted territory around the gray star on the left side of the same figure. This particular region is of a very important interest since at first glance it may indicate that a low electron recoil is hard to achieve, however, and as we will show below that is not the case. We represent these three cases as:

$$\begin{aligned} \text{BMP1}: \quad & m_0 \approx m_1 \gg m_e,\, m_i \gg m_e, \\ \text{BMP2}: \quad & m_0 \approx m_1 \gg m_e,\, m_i < m_e, \\ \text{BMP3}: \quad & m_0 \gg m_e > m_1,\, m_i < m_e. \end{aligned} \tag{5.7}$$

In what follows, we present a summary of equation (5.3) for the models in table 5.1 in the three limiting cases given by the BMPs above. Let us consider first the VF case and rewrite equation (5.3) as

$$\frac{d\sigma_{1e}}{dE_r} = \frac{\left(g_\chi^V g_e^V\right)^2}{32\pi m_e |\mathbf{p}|^2} \frac{\overline{|\mathcal{A}|}^2}{\left(2m_e E_r + m_V^2\right)^2}. \tag{5.8}$$

- BMP1: here we apply the first BMP conditions on equation (5.8). For convenience, let us parameterize the squared amplitude as:

  $$\overline{|\mathcal{A}|}^2 = 8m_e^2 E_1^2 \left\{ 2 - \left(2\frac{m_e}{E_1} + \frac{m_e^2}{E_1^2} + \frac{m_1^2}{E_1^2} \right) \frac{E_r}{m_e} + \frac{E_r^2}{E_1^2} \right\}. \tag{5.9}$$

  In the same time, we can see that in the region around the magenta star in figure 5.1, a choice of the maximum recoil energy can easily be made such that $E_r \ll m_e$. Therefore, and with the help of the above parametrization, one can approximate the numerator and the denominator of the second factor of equation (5.8) as

  $$\overline{|\mathcal{A}|}^2 \approx 16 m_e^2 E_1^2, \tag{5.10}$$

  and

  $$\left(2m_e E_r + m_V^2\right)^2 \approx m_V^4, \tag{5.11}$$

  where we have dropped out terms that are proportional to $\frac{E_r}{m_e}$ and $\frac{E_r^2}{E_1^2}$ given that their corresponding coefficients are smaller than or equal to 1. Eventually, we approximate the differential cross section by

$$\frac{d\sigma_{1e}}{dE_r} \approx \frac{\left(g_\chi^V g_e^V\right)^2 m_e E_1^2}{2\pi |\mathbf{p}|^2 m_V^4}. \tag{5.12}$$

Which means that the spectrum should be approximately flat.

- BMP2: this case is very similar to BMP1, but the only difference here is that $m_V < m_e$ which means that the mediator mass could be in the same order of recoil energy. Therefore, one can not simply remove terms that are proportional to $\frac{E_r}{m_V}$. That consequently mean, the amplitude will be exactly the same as before while the denominator that is coming from the propagator should not be approximated.

$$\frac{d\sigma_{1e}}{dE_r} \approx \frac{\left(g_\chi^V g_e^V\right)^2 meE_1^2}{2\pi |\mathbf{p}|^2 (2m_e E_r + m_V^2)^2}. \tag{5.13}$$

- BMP3: this case is kinematically different since it is located in the high boost region. In fact, this case is still similar to BMP2 at least in the mediator mass in the denominator. However it is different in the squared amplitude. Let us rewrite equation (5.9) as:

$$\overline{|\mathcal{A}|}^2 = 8m_e^2 E_1^2 \left\{ 2 - \left[2 + \frac{m_e}{E_1} + \frac{m_1^2}{m_e E_1} \right] \frac{E_r}{E_1} + \frac{E_r^2}{E_1^2} \right\}. \tag{5.14}$$

According to the third line in equation (5.7), the square bracket is effectively approximated by 2. Also notice that in this BMP, $E_r^{\max}$ is is relatively in the same order of E_1 though smaller. Therefore, we can approximate the differential cross section by

$$\frac{d\sigma_{1e}}{dE_r} \approx \frac{\left(g_\chi^V g_e^V\right)^2 meE_1^2}{2\pi |\mathbf{p}|^2 (2m_e E_r + m_V^2)^2} \left[1 - \frac{E_r}{E_1} \right], \tag{5.15}$$

where we have dropped the term that is proportional to $\frac{E_r^2}{E_1^2}$. In practice, if the differential cross section peaks at low E_r and exhibits a falling behavior with increasing E_r, it is safe to drop the square bracket completely from the above equation. Which means that in some limit BMP3 becomes similar to BMP2.

5.1.3 Case Studies: all other Models

For each of the 7 models provided in table 5.1, we can repeat the same analysis we have done above in three limiting cases given by the BMPs in equation (5.7). To avoid a lot of repetition, we rather provide a summary of the final expressions of the differential cross section as well as some general comments. We first remark that, for any given model with mediator mass m_i, the denominator of the propagator will always be approximated by m_i^4 for BMP1 however no approximation is made for the other two BMPs. We also note that the squared amplitude is different from a model to another. But it is helpful to see that as long as it has no dependence on the mass of the mediator, $\overline{|\mathcal{A}|}^2$ has the same form for both BMP1 and BMP2.

As done for the VF case in equation (5.12), (5.13) and (5.15), in table 5.2 we summarize the final expressions of the differential cross section for all the 7 models we considered above. We do that for the three limiting cases given by the BMPs in equation (5.7). We observe the similarity between the vector, axial-vector and scalar mediators, 5 models in total. For instance, in BMP1, all of them give rise to a flat distribution. They also have very similar form for BMP2 and BMP3, for example when $E_r \gg m_i^2/2m_e$ they all exhibit a falling distribution with increasing E_r. On the other hand, when $E_r \ll m_i^2/2m_e$ they all tend to have a flat distribution with decreasing E_r. In figure 5.2 we show two examples of these 5 cases, namely VF (AF) case in the left (right) panel. For BMP1 (red solid curve), we chose the numerical values of the parameters m_1 and E_1 in the degenerate regime to be in the center of the magenta star in the right side of figure 5.1 with $m_i = 15$ MeV. For BMP2 (green solid curve), we do the same as BMP1 but change the mass of the mediator to $m_i = 30$ keV. For BMP3 (blue solid curve), we chose the value of the parameters m_1 and E_1 in the highly boosted region to be in the center of the gray star on the left side of figure 5.1 with

	$\frac{d\sigma_{1e}}{dE_r} \approx \frac{\left(g_j^i g_e^i\right)^2 m_e}{2\pi\lvert\mathbf{p}\rvert^2} \times$		
case	BMP1	BMP2	BMP3
VF/VS	$\frac{E_1^2}{m_V^4}$	$\frac{E_1^2}{(2m_e E_r+m_V^2)^2}$	$\frac{E_1^2\,(1-\frac{E_r}{E_1})}{(2m_e E_r+m_V^2)^2}$
AF	$\frac{E_1^2+2m_1^2}{m_A^4}$	$\frac{E_1^2\left\{1+\frac{2m_1^2}{E_1^2}\left(1+2\frac{m_e E_r}{m_A^2}+2\frac{m_e^2 E_r^2}{m_A^4}\right)\right\}}{(2m_e E_r+m_A^2)^2}$	table 5.1
PF	$\frac{E_r^2}{4m_a^4}$	$\frac{E_r^2}{4(2m_e E_r+m_a^2)^2}$	$\frac{E_r^2}{4(2m_e E_r+m_a^2)^2}$
PS	$\frac{m_1^2 E_r}{2m_e m_a^4}$	$\frac{m_1^2 E_r}{2m_e(2m_e E_r+m_a^2)^2}$	$\frac{m_1^2 E_r}{2m_e(2m_e E_r+m_a^2)^2}$
SF	$\frac{m_1^2}{m_\phi^4}$	$\frac{m_1^2}{(2m_e E_r+m_\phi^2)^2}$	$\frac{m_1^2\left(\frac{E_r}{2m_e}+\frac{E_r^2}{4m_1^2}\right)}{(2m_e E_r+m_\phi^2)^2}$
SS	$\frac{m_1^2}{m_\phi^4}$	$\frac{m_1^2}{(2m_e E_r+m_\phi^2)^2}$	$\frac{m_1^2\left(1+\frac{E_r}{2m_e}\right)}{(2m_e E_r+m_\phi^2)^2}$

Table 5.2: Approximation of the differential cross section with respect to electron recoil energy for the 7 model scenarios in table 5.1 estimated at the three BMPs given by equation (5.7).

$m_i = 30$ keV. For clarity, throughout our numerical analysis we use:

$$\begin{aligned} \mathrm{BMP1:} \quad & m_0 = 1.002\, m_1 = 10\,\mathrm{MeV},\ m_i = 15\,\mathrm{MeV}, \\ \mathrm{BMP2:} \quad & m_0 = 1.002\, m_1 = 10\,\mathrm{MeV},\ m_i = 30\,\mathrm{keV}, \\ \mathrm{BMP3:} \quad & m_0 = 10^3\, m_1 = 10\,\mathrm{MeV},\ m_i = 30\,\mathrm{keV}. \end{aligned} \tag{5.16}$$

We note that in making these plots, we used the full expressions as in table 5.1 rather than the approximated expressions in table 5.2. As we have analyzed above, we see that indeed the first BMP exhibits a flat distribution while the other tend to have a falling distributions.

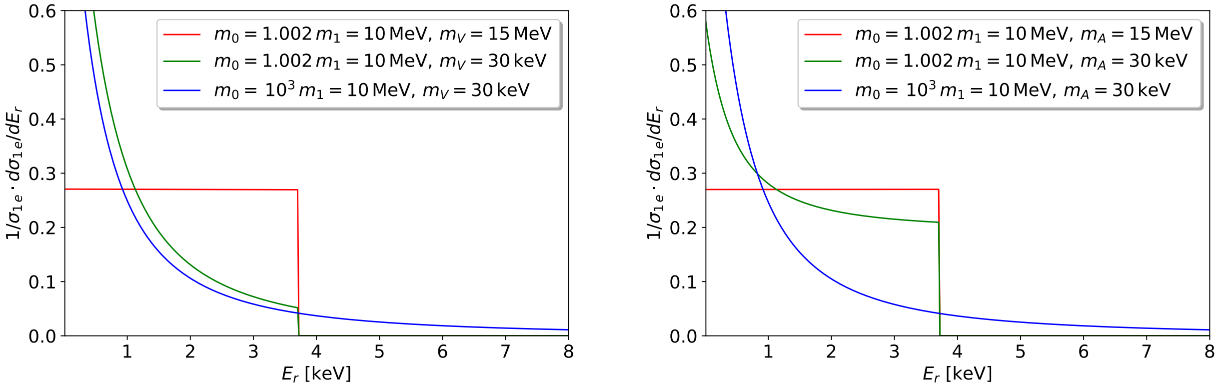

Figure 5.2: Differential cross section with respect to the electron recoil energy normalized to the total cross section. Left (right) panel corresponds to the VF (AF) scenarios while red, green and blue solid curves represent the first, second and third BMPs respectively.

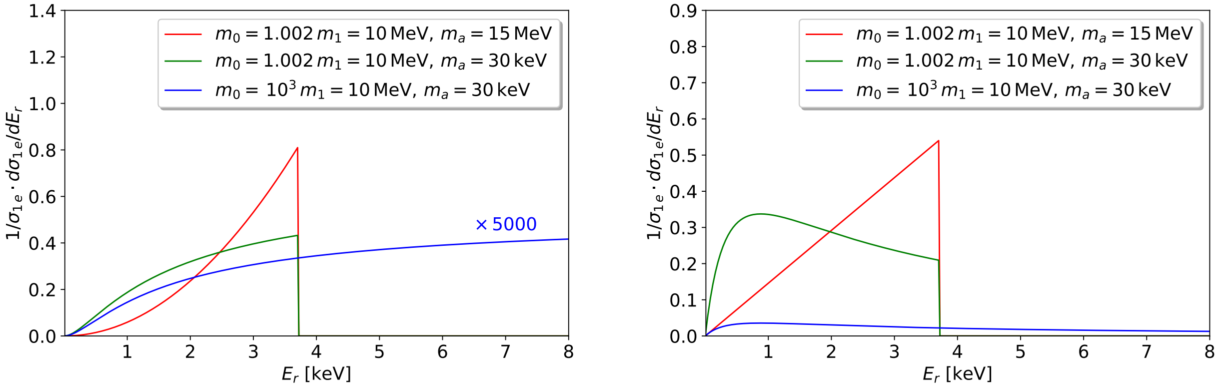

Figure 5.3: Differential cross section with respect to the electron recoil energy normalized to the total cross section. Left (right) panel corresponds to the PF (PS) scenarios while red, green and blue solid curves represent the first, second and third BMPs respectively.

Notice that red and green curves have an end point somewhere around 3.7 keV that is because the first and second BMPs share the same kinematics as we explained in figure 5.1. In other words the maximum recoil energy is solely determined by m_0 and m_1.

In contrast to other mediators, pseudo-scalar mediator (two cases) exhibits a rising distribution for the first BMP. More precisely, the distribution rise as a linear and quadratic function in E_r for scalar and fermionic dark matter respectively. For the second and third BMPs, the PF case distribution rises with increasing E_r in a quadratic form in the region where $E_r \ll m_a^2/2m_e$. As E_r continue increasing beyond $m_a^2/2m_e$ the distributions start to become flat. The PS case is also similar in the sense that its distributions rise, though linearly, in the region where $E_r \ll m_a^2/2m_e$ however it exhibits a falling distribution beyond $m_a^2/2m_e$. We show the pseudo-scalar mediator for fermionic and scalar dark matter in the left and right panels of figure 5.3. Since the blue curve (BMP3) has an end point at extremely large E_r, we see that the normalized distribution in the PF case has a very slow increase and has to be artificially enhanced.

5.2 Scattering Energy Spectrum at Low Electron Recoil

At this level of the analysis, it is very important to highlight the effects of the ionization form factor we discussed in the previous chapter. Since all of the important details had been worked out above, all one needs to do is to replace equation (5.1) with equation (4.19) which takes care of low recoil effects. For direct comparison with the discussion in the previous section, we will continue presenting the numerical results in view of the three BMPs as in equation (5.17). These BMPs, spans 5 order of magnitudes in the transfer momentum, $|\mathbf{q}|$. In figure 5.4, we compare the three ionization form factors: PW (dotted black), SCE (dashed black) and DCE (solid) with the latter having four types of mediators: V (black), A (blue), S (green) and P (red). We notice the overall differences between non-relativistic approximation and relativistic one. For example, at low $|\mathbf{q}|$, non-relativistic approximations has significantly high values in contrast to the relativistic case. On the other hand, at high momentum transfer, the relativistic approximation is dominant. At momentum transfer close to the $|\mathbf{k}'|$ value all approximation seem to overlap with each other.

Now we can numerically discuss theses effects and their implications on the normalized differential cross section. We take the Xe atom and particularly the contribution from its 3 outermost shell as an example. We study how the shapes of the energy spectrum changes when including different approximations for the ionization form factor and compare it to the free scattering case as discussed in the previous section. In figure 5.5 we repeat the same (solid curves) as in figure 5.2 in which we take the VF case on the left and the AF case on

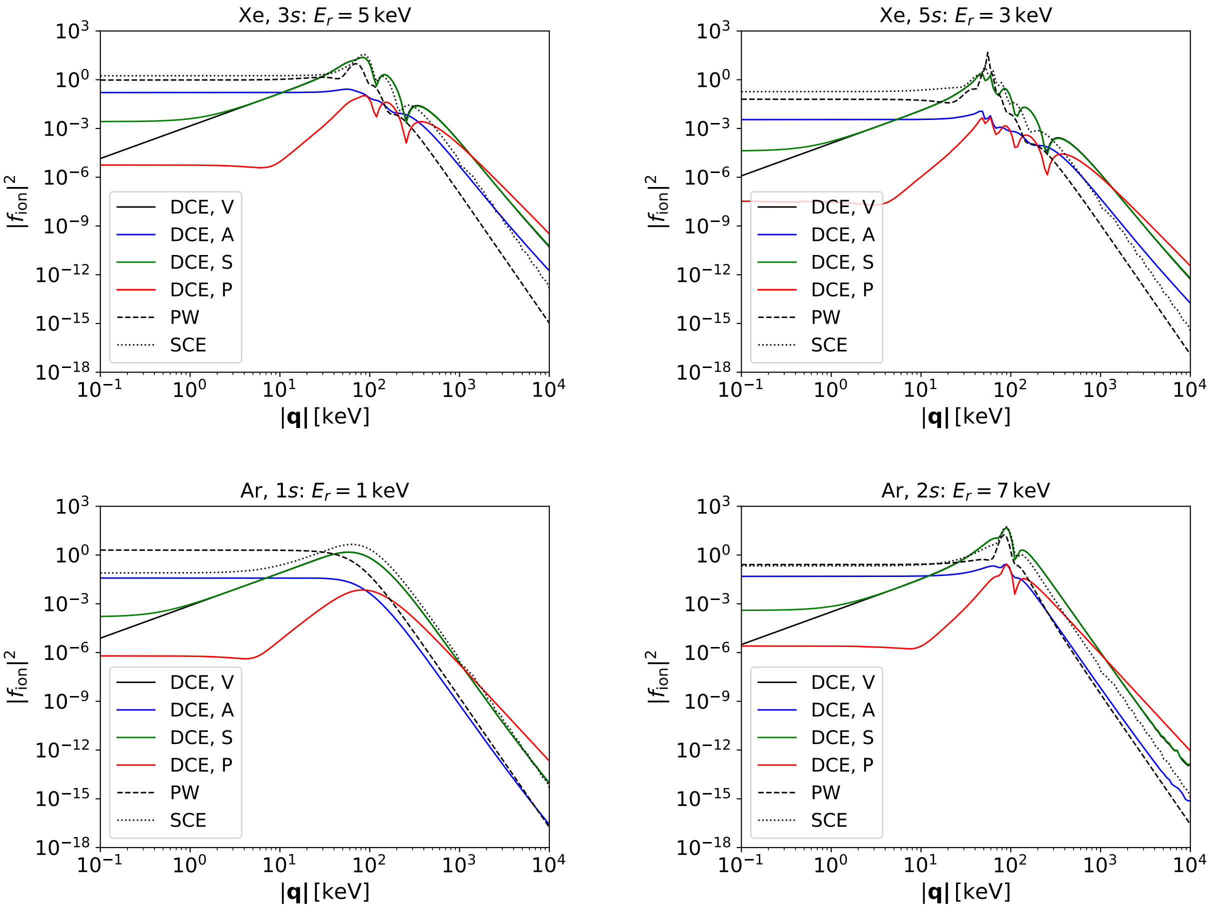

Figure 5.4: Top: Xe 3s and 5s shells in the left and right panels respectively. Notice the wide range of interest for the momentum transfer, $|\mathbf{q}|$. For first and second BMPs we are interested in the region where $|\mathbf{q}| < 60$ keV. For the third BMP, we are interested in the entire range. Bottom: the same as the top panel but for Ar 1s and 2s in the left and right panels respectively.

the right panel however this time we add the ionization form factor effects due to the PW approximation (dashed curves) and the DCE approximation in (dotted curves). Generally, we observe a very similar behavior between the free and PW cases. In other words, it appears that the PW approximation does not dramatically deform the energy spectrum at least for the 3 considered shell. We think that this is due to the PW behavior in the top right panel of figure 5.4 which dominantly is flat with a sharp peak at $|\mathbf{q}| \sim |\mathbf{k}'|$ making it somehow similar to a delta function behavior. On the other hand the DCE approximation highly depends on the mediator type and can deform the shapes significantly. For example, BMP1 (red)

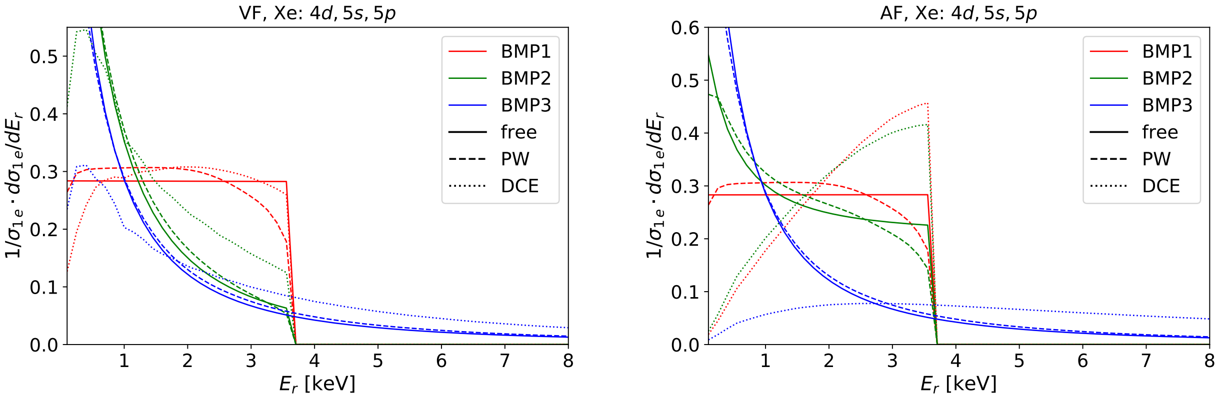

Figure 5.5: Differential cross section with respect to the electron recoil energy normalized to the total cross section. Left (right) panel corresponds to the VF (AF) scenarios while red, green and blue solid curves represent the first, second and third BMPs respectively. The solid curves correspond to the free scattering (the same as in figure 5.2), the dashed curves includes the PW approximation and the dotted curves include the DCE approximation.

has exactly the same shape in VF and AF in free scattering however we observe that as a result of the DCE approximation, the AF case transforms from a flat distribution to linearly increasing one! Similar conclusion is drawn on the other BMPs (green and red). Also in comparison with previous section, in figure 5.6 we repeat the same as in figure 5.5 but this time for the PF case on the left and the PS on the right panel. We still observe the overall similarity between the PW and the free case. However, the DCE is again case dependent. For example, in the PS case, the peak of BMP2 distribution (green) shifts to the opposite side after including the DCE approximation. In contrast to the previous figure, here the mediator type is fixed but the DCE case still lead to different behavior in different models. That means that the deformation in spectrum shape does not only depend on the mediator type but it is also sensitive to the matrix element squared due to the convolution in equation (4.19).

5.3 The XENON1T Excess

In application to the previous discussion so for and as a phenomenological example, we would like to take the recent excess observed by the XENON1T experiment as a case study

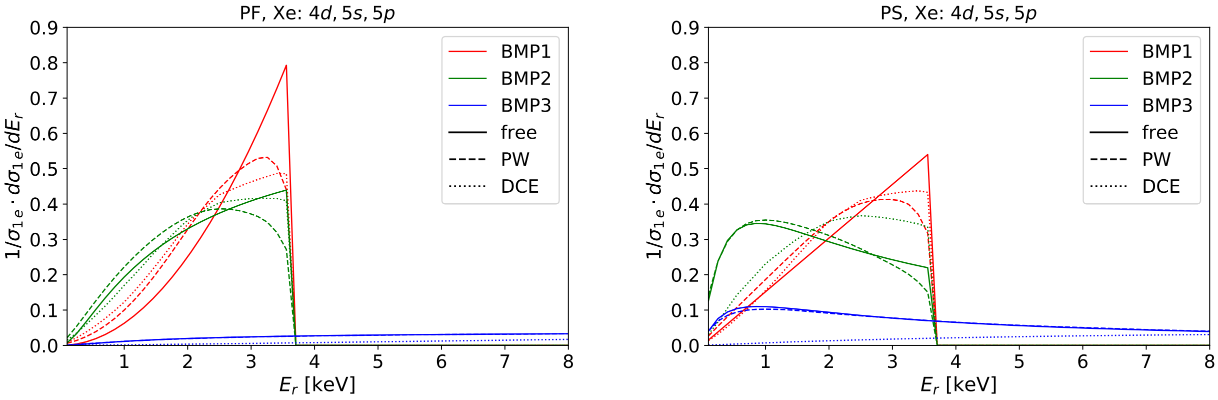

Figure 5.6: Differential cross section with respect to the electron recoil energy normalized to the total cross section. Left (right) panel corresponds to the PF (PS) scenarios while red, green and blue solid curves represent the first, second and third BMPs respectively. The solid curves correspond to the free scattering (the same as in figure 5.3), the dashed curves includes the PW approximation and the dotted curves include the DCE approximation.

for this section [134]. The excess was reported at electron recoil energy below 7 keV with a noticeable excess ($\sim$ 50 events) between 2 keV and 3 keV with 0.65 ton×year exposure. Though unresolved β decays of tritium according to the XENON Collaboration and other backgrounds [135] may explain the excess, it is still an interesting exercise to consider BDM from the GC [12] as a source for the excess. And since this excess takes place at relatively small recoil energies, it would be of a great importance to demonstrate the effects of the ionization form factor. For dark matter interpretation to the XENON1T excess, see for example Refs. [136–141].

In spirit of equation (3.10) we can readily write the differential distribution of the number of expected BDM signal with respect to the electron recoil energy as

$$\frac{dN_{\rm sig}}{dE_r} = \Delta T\,\Phi_1\,N_{\rm Xe}\times\begin{cases} N_e^{\rm eff}\frac{d\sigma_{1e}}{dE_r} & \text{free scattering,}\\ \sum_{n,\ell}\frac{d\sigma_{1e}^{n\ell}}{dE_r} & \text{PW, SCE and DCE.}\end{cases} \tag{5.17}$$

Where the first three factors on the right side are respectively the exposure time of the

---

[12] There is nothing special about the GC, one can also consider other sources. We only take the GC as an example.

experiment, the BDM flux and the number of target atoms: there are roughly 4.6×10^{27} atoms in 1 ton of Xe. The top line corresponds to the free scattering with effective number of electrons per Xe atom, N_e^{eff} and the differential cross section is defined in equation (5.3). The bottom line corresponds to differential cross section when including the ionization form factor as in equation (4.19). Throughout the analysis of this section we will always fix the the BDM-mediator coupling, g_1^i, to unity and adjust the electron-mediator coupling, g_e^i, to produce enough amount of events as desired by the XENON1T excess. For the other parameters, we stick with three BMPs numerically defined in equation (5.17). We also consider detector effects that are suitable for the XENON1T. For example we use a Gaussian, f_{res}, for the detector resolution and define it as:

$$f_{\text{res}}\left(E_r, \tilde{E}_r\right) = \frac{1}{\sigma_{\text{res}}\sqrt{2\pi}} \exp\left[-\frac{\left(E_r - \tilde{E}_r\right)^2}{2\sigma_{\text{res}}^2}\right], \tag{5.18}$$

with the tilde symbol indicating non-smeared quantities. For the parameter σ_{res}, we use the energy dependent resolution defined in Ref. [134]. We use a detector efficiency, f_{eff}, [134] and represent the differential cross section generically as

$$\frac{d\sigma_{1e}}{dE_r} = f_{\text{eff}}\left(E_r\right) \int_0^{E_r^{\max}} d\tilde{E}_r f_{\text{res}}\left(E_r, \tilde{E}_r\right) \frac{d\sigma_{1e}}{d\tilde{E}_r}. \tag{5.19}$$

In what follows, we show the number of BDM signal events (equation (5.17)) after applying the detector effects above at the XENON1T detector normalized by ton×year of exposure. We focus on examples that lead to tens of events in the region around 2-3 keV of electron recoil. For comparison with the previous discussion of this chapter, we will present four example models: VF, AF, PF and PS. In figure 5.7, top, we show the VF (AF) model in the left (right) panel for free scattering assuming $N_e^{\text{eff}} = 18$ electrons for three BMPs with the parameter values and color representation as in the previous section. We report the total cross section as well as the coupling value that is needed to generate the number of signal

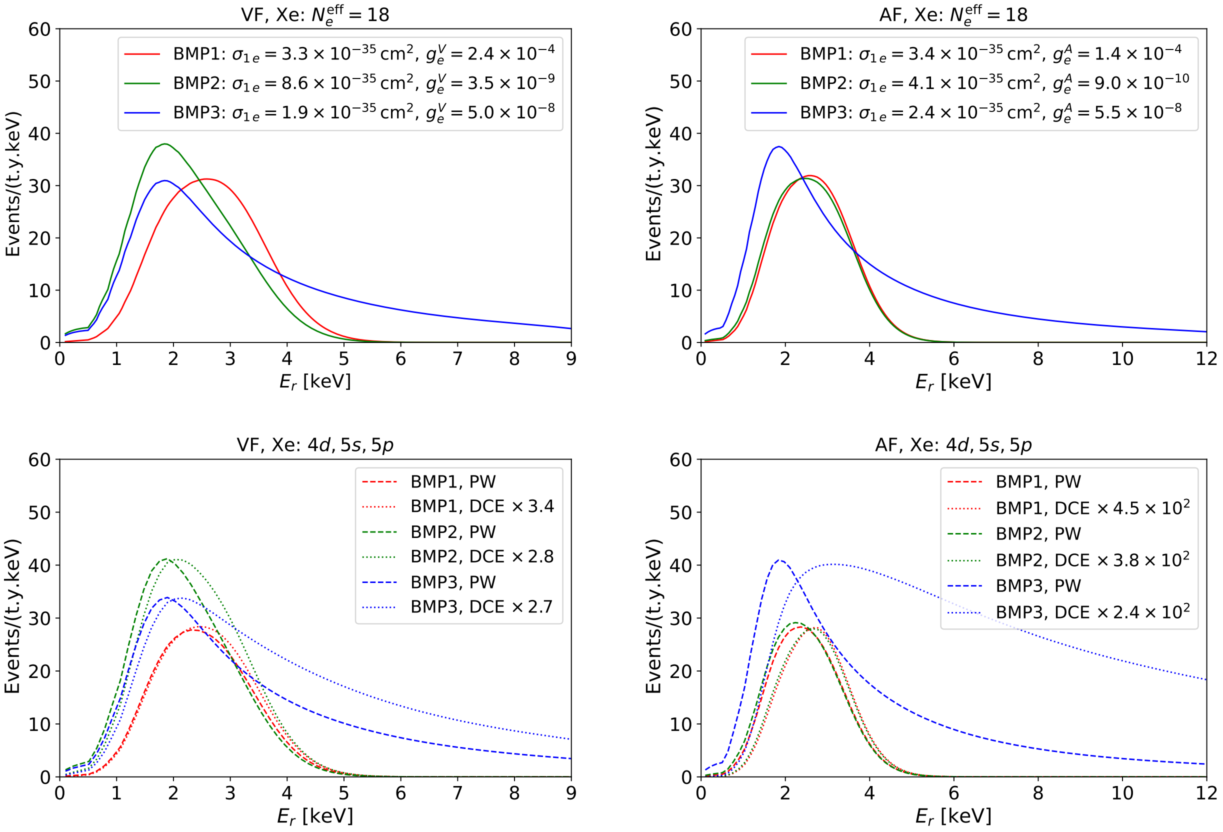

Figure 5.7: Number of dark matter signal at XENON1T for the two models: VF and AF in the left and right panel respectively. Red, green and blue represent first, second and third BMP respectively. The top row corresponds to the treatment explained in section 5.1 where electron is assumed free with $N_e^{\rm eff} = 18$.. The bottom row consider the effects from binding energy as well as atomic effects, i.e., including the ionization form factor. Where dashed curves assume the PW approximation while dotted assume the DCE approximation. It only counts contributions from the outermost 3 shells of the Xe atom.

excess desired by the XENON1T. In the bottom panel of the same figure, we repeat the same as the top however we consider ionization form factor effects from the PW approximation (dashed curves) and the DCE approximation (dotted curve). The curves solid, dashed and dotted should be compared correspondingly for different models to that of figure 5.5, however, this time we added the detector effects and plotted the number of signal events instead of the cross section. We also observe the generic distortion in the shape of the distributions due to the introduction of the ionization form factor. But the differences unfortunately are

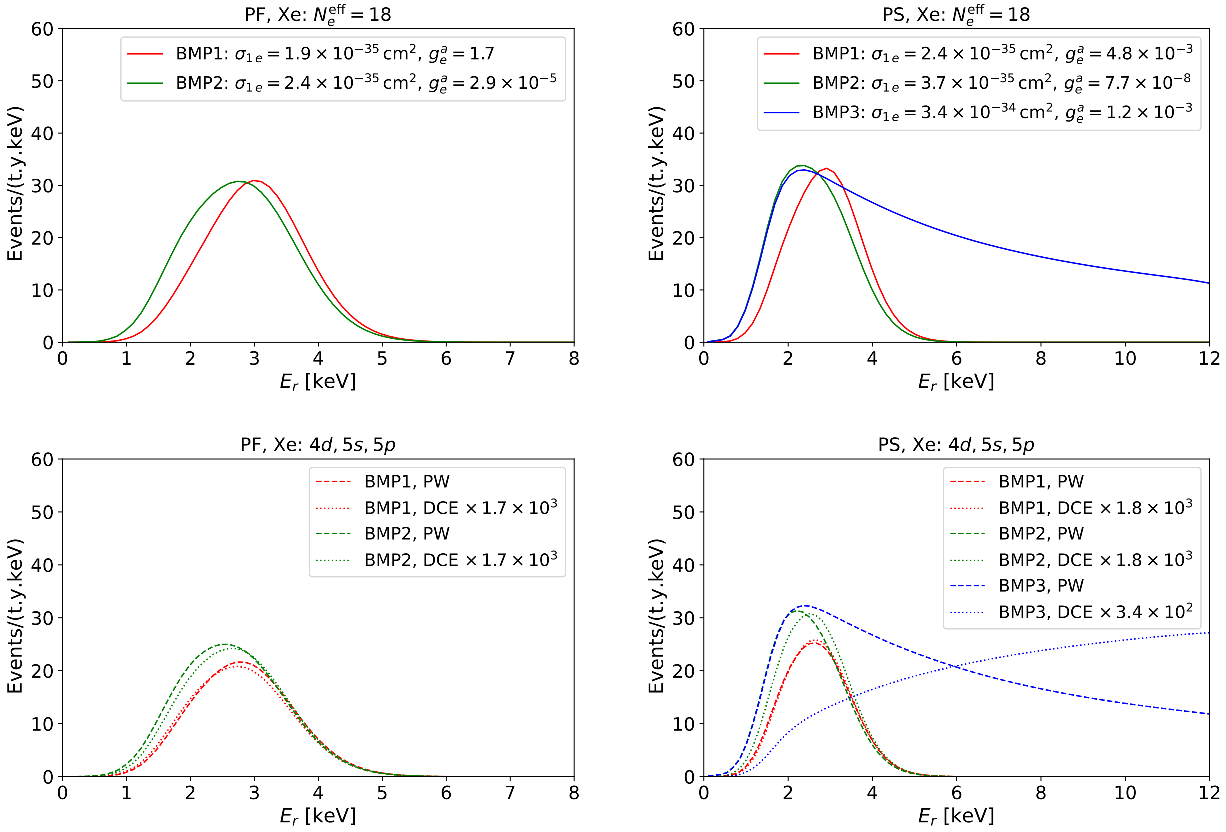

Figure 5.8: Number of dark matter signal at XENON1T for the two models: PF and PS in the left and right panel respectively. Red, green and blue represent first, second and third BMP respectively. The top row corresponds to the treatment explained in section 5.1 where electron is assumed free with $N_e^{\rm eff} = 18$. The bottom row consider the effects from binding energy as well as atomic effects, i.e., including the ionization form factor. Where dashed curves assume the PW approximation while dotted assume the DCE approximation. It only counts contributions from the outermost 3 shells of the Xe atom.

not very distinct in some cases due to the presence of the detector effects. For example, in AF case of figure 5.5, we noticed that different ionization form factors dramatically lead to different distributions in BMP1 and BMP2, however, due to detector effects this difference is not so pronounced in figure 5.7. On the other hand, differences in BMP3 distributions still persist even after detector effect due to the fact that BMP3 has much wider distribution. Another thing that is very significant to highlight is the effect of the mediator type, see figure 5.4. One major difference between the PW and DCE is that the latter is relativistic while the former is non-relativistic, additionally, the DCE, is capable of describing different types of mediators while the PW is not. This makes the PW not suitable for mediators such as pseudo-scalar or axial-vector because the different Lorentz structure they bring to the transition factor of the previous chapter. In order to compare the PW to the DCE, in figure 5.7, we artificially multiply the DCE case by an overall factor (see the legends of the bottom panel). Notice that for the VF model, an order of 1 number is needed while 2 order of magnitude is needed for the AF model. This highlights the fact that the PW is indeed not suitable to mediators other than vector or scalar. In figure 5.8, we repeat the same thing as in figure 5.7 however this time for model PF in the left panel and PS in the right panel. Similar conclusions are drawn as above. For example, the pronounced shape difference in the PS model between PW and DCE in figure 5.6 especially for BMP1 and BMP2 becomes less pronounced due to detector effects while the difference still persist for BMP3 due to its wider distribution. Also notice that the PW approximation overestimates the number of signal events by more than 3 order of magnitudes making it unsuitable for pseudo-scalar mediator. Finally, we intentionally dropped the third BMP from the left panel since it will lead to a shape that raises over a long range of electron recoil causing an excess far beyond the desired one by XENON1T, see figure 5.3.

By looking at the last two figures, we can say that different models of BDM are generally capable of interpreting the XENON1T excess, however, the presence of the ionization form factor can first severely change the shape of the expected distribution from free scattering and second can reduce the number of expected signal events quite significantly.

Before concluding this section, it is important to highlight the effects of including all allowed shells to our discussion above. We learned in section 4.1 that based on the kinematics, there are allowed shells that contribute to the differential cross section denoted by $\{n\ell\}_{\text{allowed}}$. Since BMP1 and BMP2 generate relatively low electron recoil in contrast to BMP3, we anticipate that the number of BDM signal should increase in BMP3 in comparison to the others due to the possibility of exciting electrons deeper in the Xe atom. We demonstrate

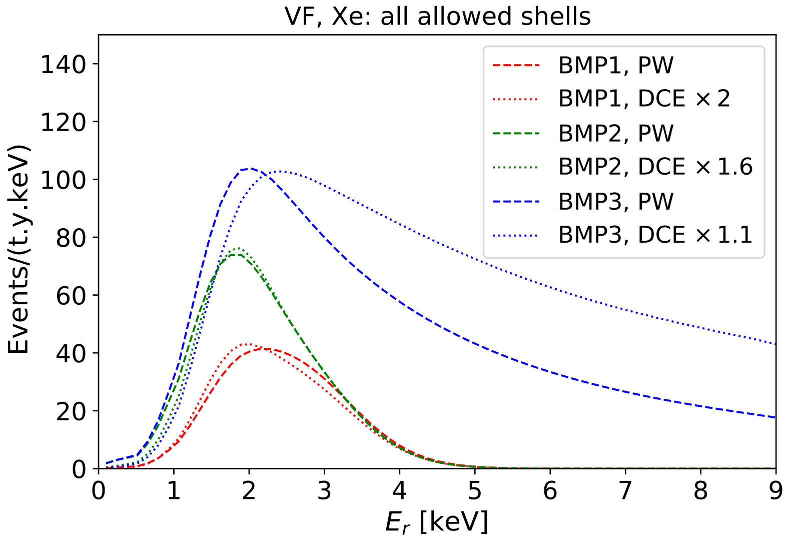

Figure 5.9: Number of dark matter signal at XENON1T for VF model including the ionization form factor with allowed Xe shells where dashed curves assume the PW approximation while dotted assume the DCE approximation. Red, green and blue represent first, second and third BMP respectively.

this for the VF case in figure 5.9 by including all allowed shells: for BMP1 and BMP2, $\{n\ell\}_{\text{allowed}} = \{3p, 3d, 4s, 4p, 4d, 5s, 5p\}$ while for BMP3 all shells are allowed. The curves of this figure should be compared to those of the the bottom left panel of figure 5.7. As has been anticipated, the number of BDM signal had increased overall with a higher increase in BMP3. It is also noticeable to mention that the shapes had deformed slightly, for example, the peak of BMP1 curve corresponding to the DCE approximation shifts slightly to the left side. Moreover, we observe that the relative proportionality between the two approximation has changed, see the artificial numerical factors in the legend, they are smaller when including all allowed shells indicating the different behaviors of the ionization form factor shell by shell for different approximations.

In summary of this chapter, we have considered a class of BDM models as a generalization to chapter 3 as well as relaxing the mass hierarchy condition to $m_0 > m_1$ only and allowing degenerate cases. While studying the parameter space, we noticed the need of some special treatment at low electron recoil energies. We did apply the ionization form factor treatment developed earlier in chapter 4 by first deriving the free scattering limit, analyzing the parameter space into case studies and eventually study the electron recoil spectrum for the different models. Additionally, we investigated how the ionization form factor can dramatically change the shape of the energy spectrum not only by deforming it but in some cases transforming it to totally different shape. Finally, we took the recent excess observed by XENON1T as a proof of principle exercise to probe BDM at direct detection experiment by scattering off an electron and showed the importance of the ionization form factor and how different approximations could lead to very different conclusions.

Chapter 6

Generic Fast Moving Dark Matter

As we have demonstrated in the previous chapters, BDM provides an interesting phenomenology at different experiments. Though we were able to generalize our discussion from the very particular scenario of chapter 3 (mass hierarchy and high electron recoil energy) to a class of different models (while relaxing the hierarchy mass assumption) leading to a phenomenology at low electron recoil energy in chapter 5, we are still considering a particular mechanism to explain the high speed of dark matter. In this chapter we intend to generalize our discussion even more by considering somewhat simple mechanism independent scenario where the speed of dark matter is not fixed to a particular mechanism as in BDM. Therefore, we will generically refer to a dark matter with high speed to a fast moving dark matter without focusing on the reasons why it is fast.

6.1 General Framework

With the formalism we have introduced in the previous chapters, we are in a position to provide some general comments on fast moving dark matter. What we have done so far was the case where the velocity, v_{1e}, of the boosted dark matter particle was a consequence of the mass difference between the heavy and light particles in the dark sector. As we have explained above, the velocity is related to the energy, E_1, and hence to the mass, m_0, of the heavy state in the dark sector. Moreover, an assumption on how the heavy states annihilate to the light states was considered. This makes our approach somewhat mechanism dependent. However, without a severe modification to our formalism, we can still introduce a general class of dark matter models irrespective of the interpretation of the dark matter velocity. Therefore, and without focusing on any particular mechanism, we start by assuming that there exist a dark matter particle with velocity v_{1e} that can be relativistic in general. To make the transition from our previous formalism more transparent and mechanism independent, we remove the dependence on the heavy states parameters such as m_0 from our formalism. We can do that by re-writing equation (4.19) and instead parameterize it in the velocity v_{1e} as follows

$$\frac{d\sigma_{1e}^{n\ell}}{dE_r} = \frac{1}{64\pi}\,\frac{1-v_{1e}^2}{v_{1e}^2}\,\frac{1}{m_1^2 E_r(2m_e+E_r)(m_e-|E_{n\ell}^B|)}\int_{|\mathbf{q}|^{\min}}^{|\mathbf{q}|^{\max}} d|\mathbf{q}|\;\;|\mathbf{q}|\,|\mathcal{M}|^2\,|f_{ion}(E_r,\,|\mathbf{q}|)|^2. \tag{6.1}$$

Sometimes, one is interested in estimating the cross section differential rate by factoring out the momentum transfer dependence from the matrix element square in equation (4.13). As in Refs. [120, 122, 123], this factorization takes the following form

$$|\mathcal{M}|^2 = |\mathcal{M}|^2_{|\mathbf{q}|=\alpha m_e} \times |F_{\rm DM}(|\mathbf{q}|)|^2, \tag{6.2}$$

where $|F_{\rm DM}(|\mathbf{q}|)|^2$ is a dark matter form factor that carries the momentum transfer dependence while the prefactor is related to the dark matter elastic scattering cross section with the electron according to

$$\bar{\sigma}_{1e} = \frac{\mu_{1e}^2}{16\pi m_e^2 m_1^2}\,|\mathcal{M}|^2_{|\mathbf{q}|=\alpha m_e}, \tag{6.3}$$

where μ_{1e}^2 is the dark matter electron reduced mass. With this modification, our expression in equation (6.1) changes to

$$\frac{d\sigma_{1e}^{n\ell}}{dE_r} = \frac{\bar{\sigma}_{1e}}{8\mu_{1e}^2}\,\frac{1-v_{1e}^2}{v_{1e}^2}\,\frac{1}{E_r(1+E_r/2m_e)(1-|E_{n\ell}^B|/m_e)}\int_{|\mathbf{q}|^{\min}}^{|\mathbf{q}|^{\max}} d|\mathbf{q}|\,|\mathbf{q}||F_{\rm DM}(|\mathbf{q}|)|^2|f_{ion}^{n\ell}(E_r,|\mathbf{q}|)|^2. \tag{6.4}$$

Finally, in the limit where $v_{1e}^2 \ll 1$, $E_r \ll m_e$ and $|E_{n\ell}^B| \ll m_e$ we can immediately retrieve

$$\frac{d\sigma_{1e}^{n\ell}\,v_{1e}}{dE_r} \approx \frac{\bar{\sigma}_{1e}}{8\mu_{1e}^2 v_{1e} E_r}\int_{|\mathbf{q}|^{\min}}^{|\mathbf{q}|^{\max}} d|\mathbf{q}|\;\;|\mathbf{q}|\,|F_{\rm DM}(|\mathbf{q}|)|^2\,|f_{ion}^{n\ell}(E_r,\,|\mathbf{q}|)|^2, \tag{6.5}$$

which is the the same when ignoring the velocity averaging as in Refs. [120, 122, 123]. Note that in this expression, the limits of integration over the momentum transfer shall be modified to the non-relativistic ones, see for example Ref. [130]

$$|\mathbf{q}|^{\mathrm{max/min}} = m_1 v_{1e} \pm \sqrt{m_1^2 v_{1e}^2 - 2m_1(E_r + |E^B_{n\ell}|)}, \tag{6.6}$$

and not those given in section 4.1.

6.2 The XENON1T Excess Revisited

At this stage it is important to note the major difference between what we are following here and that used in references such as Refs. [133, 136, 142]. For example, in Ref. [136], the equation that is equivalent to equation (6.5) has the form

$$\left(\frac{d\sigma^{n\ell}_{1e}\, v_{1e}}{dE_r}\right)_* = \frac{\bar{\sigma}_{1e}}{2m_e v_{1e}} \int_{|\mathbf{q}|^{\mathrm{min}}}^{|\mathbf{q}|^{\mathrm{max}}} d|\mathbf{q}|\; a_0^2\, |\mathbf{q}|\, |F_{\mathrm{DM}}(|\mathbf{q}|)|^2\, K, \tag{6.7}$$

where K introduced in Ref. [130] as the “atomic kernel” is equivalent to the transition factor $|f_{e_i \to e_f}(\mathbf{q})|^2$ of equation (4.21) which we know is a dimensionful quantity with units $=$ [momentum^{-3}]. Since K is a dimensionless quantity in the above equation, we interpret $K = |f_{e_i \to e_f}(\mathbf{q})|^2 / a_0^3$. Therefore, while $E_r \ll me$, we can re-express the above equation in view of equation (4.21) as

$$\left(\frac{d\sigma^{n\ell}_{1e}\, v_{1e}}{dE_r}\right)_* \approx \frac{1}{8(meE_r)^{3/2}}\, \frac{(2\pi)^3\alpha}{\sqrt{2}}\, \frac{\bar{\sigma}_{1e}}{v_{1e}} \int_{|\mathbf{q}|^{\mathrm{min}}}^{|\mathbf{q}|^{\mathrm{max}}} d|\mathbf{q}|\; |\mathbf{q}|\, |F_{\mathrm{DM}}(|\mathbf{q}|)|^2\, |f^{n\ell}_{ion}(E_r,\, |\mathbf{q}|)|^2, \tag{6.8}$$

where we have used $a_0 = 1/\alpha m_e$. Note that $\frac{(2\pi)^3\alpha}{\sqrt{2}} = \mathcal{O}(1)$, an order of 1 number. Finally we compare the expression in equation (6.5) to the above one and we find that the ratio depends on the square root of the electron recoil energy:

$$\frac{d\sigma^{n\ell}_{1e}\, v_{1e}}{dE_r} \Big/ \left(\frac{d\sigma^{n\ell}_{1e}\, v_{1e}}{dE_r}\right)_* \approx \sqrt{E_r/m_e}. \tag{6.9}$$

In expressing this ratio we assumed μ_{1e} can be approximated by m_e for dark masses way above the electron mass. We think that this square root difference originated in equation (6) of Ref. [133] which is similar to equation (6.7) but with velocity averaging. The authors claimed that they used Ref. [143] whose equation (2) is similar to our equation (6.5) but with velocity averaging. It is clear that in the original expression, equation (2) of Ref. [143], the differential cross section with respect to E_r (not $\log E_r$) depends explicitly on E_r as $|\mathbf{k}'|^3/E_r$ which grows as $\sqrt{E_r}$. The reader can see that clearly by looking at equation (6.5) and (4.21). On the other hand, equation (6) of Ref. [133] does not explicitly depend on E_r.

As a cross check, Ref. [130] states that a Born approximation of a fermionic dark matter scattering off an electron via a vector mediator can be approximated by a Yukawa-type interaction. The matrix element squared of such an interaction can be written as

$$|\mathcal{M}|^2_{\mathrm{VF,\,non-rel.}} = \frac{16\, g^4\, m_e^2\, m_1^2}{(|\mathbf{q}|^2 + m_V^2)^2}, \tag{6.10}$$

where g represents a generic coupling. Now we use the above expression as well as the limit $v_{1e}^2 \ll 1$, $E_r \ll m_e$ and $|E^B_{n\ell}| \ll m_e$ to rewrite equation (6.1)

$$\frac{d\sigma^{n\ell}_{1e}}{dE_r} = \frac{4\alpha_\chi^2}{\pi}\, \frac{m_e\sqrt{2m_eE_r}}{v_{1e}^2} \int_{|\mathbf{q}|^{\min}}^{|\mathbf{q}|^{\max}} d|\mathbf{q}|\, \frac{|\mathbf{q}|}{(|\mathbf{q}|^2 + m_V^2)^2}\, |f_{e_i\to e_f}(\mathbf{q})|^2. \tag{6.11}$$

Note that we have used equation (4.21) and the expression for $|\mathbf{k}'|$. The above equation is in exact agreement with equation (8) in Ref. [130] when using $g = \sqrt{4\pi\alpha_\chi}$ and ignoring velocity averaging, it shows also the explicit dependence on $\sqrt{E_r}$. For clarity, Ref. [130] uses ΔE which in our notation is $E_r + |E^B_{n\ell}|$.

Finally, we briefly visit the XENON1T excess example once again, see section 5.3 for details. In order to highlight the discrepancy we observe between equation (6.5) and that in Ref. [136] i.e., equation (6.7), we would like to first reproduce some of the results presented in Ref. [136]. We do that by plotting the expected dark matter rate at the XENON1T based on equation (6.7) when the dark matter form factor is set to unity for two cases in the left

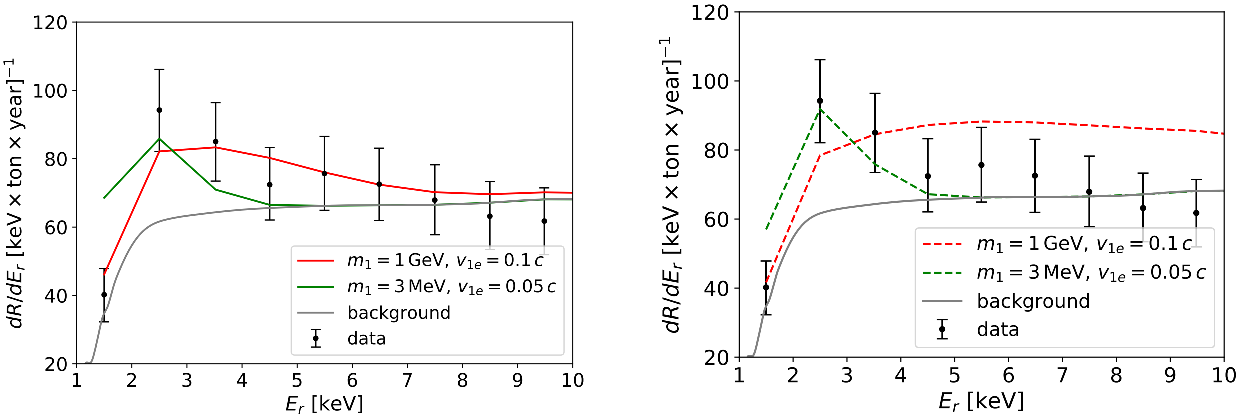

Figure 6.1: The dark matter rate at XENON1T based on Ref. [136] where left panel adopts equation (6.7) while right panel adopts equation (6.5). The background in grey and data points correspond to those reported by the XENON1T collaboration [134]. Detector effects such as resolution and efficiency are discussed in section 5.3.

panel of figure 6.1. We note that we are able to reproduce similar results given that the rates are normalized based on the first 4 bins of the observed data. The ionization form factor we considered here is the one given by the DCE approximation and the contribution to the cross section was taken only from $3s$ and $4s$ shells. Both of the two cases: red ($m_1 = 1\,\mathrm{GeV}$, $v_{1e} = 0.1\,c$) and green ($m_1 = 3\,\mathrm{MeV}$, $v_{1e} = 0.05\,c$) give rise to rates desired by the observed excess. On the right panel, we repeat the same however this time we use our derived equation (6.5) and notice the discrepancy pointed out above especially with the case represented by the red curve. Therefore, we think that the allowed parameter space that is concluded to fit the XENON1T excess should be reconsidered with proper treatment.

This example motivates us to have a much generalized discussion (apart from the XENON1T excess) where in the next section we take into account the full calculation based on the generic equation (6.1) as well as contribution from various energy shells.

6.3 Prospects at Direct Detection Experiments

Now let us express the rate, $\mathcal{R}$, of a generic fast moving dark matter interacting with electrons as

$$\frac{d\mathcal{R}_{1e}^{n\ell}}{dE_r} = n_T \, n_{\rm DM} \, \frac{d\sigma_{1e}^{n\ell} \, v_{1e}}{dE_r}, \tag{6.12}$$

where $n_{\rm T}$ is given by the the number density of the target electrons and $n_{\rm DM}$ is the number density of fast moving dark matter which we parameterize by

$$n_{\rm DM} = f_1 \, \frac{\rho_{\rm DM}}{m_1}, \tag{6.13}$$

with $\rho_{\rm DM} \approx 0.3 \, \frac{\rm GeV}{\rm cm^3}$ is the dark matter local density. The factor, f_1, is the "fraction" that dictates the amount of fast moving dark matter and we take it as a free constant parameter for simplicity. Eventually we are interested in the total rate, $\mathcal{R}^{\rm tot}$, which corresponds to the sum over all shells in a given atom and integration over the recoil energy range of equation (6.5). In this case we have 5 effective parameters: the mass of dark matter, m_1, the mass of the mediator m_i, the velocity of dark matter v_{1e}, the couplings $g_e^i \times g_1^i$ and the fast moving fraction of dark matter f_1. We are more concerned with the shape of the total rate rather than the amount of the rate itself. For this reason, we are going to present the numerical results in terms of the rate normalized to the couplings and the factor f_1 i.e., $\mathcal{R}^{\rm tot}/(g_e^i g_1^i)^2/f_1$. We will then perform a 2 dimensional scan over the mass and the velocity of the dark matter while fixing the mass of the mediator. We consider a Xe based detector and take detector effects of the XENON1T experiment as an example, see section 5.3.

In the subsequent figures of this section we show $\log\left[\mathcal{R}^{\rm tot}/(g_e^i g_1^i)^2/f_1 \times ({\rm ton} \times {\rm year})\right]$ as contours in (m_1, v_{1e}) plane. In figure 6.2 we consider the VF model with $m_V = 15$ MeV and compare the total rate of fast moving dark matter in four different considerations. The top left panel assumes free electron scattering while the others take into account the ionization form factor effects: PW approximation in top right panel, SCE approximation in left bottom panel and finally the DCE in the right bottom panel. We only consider contribution from

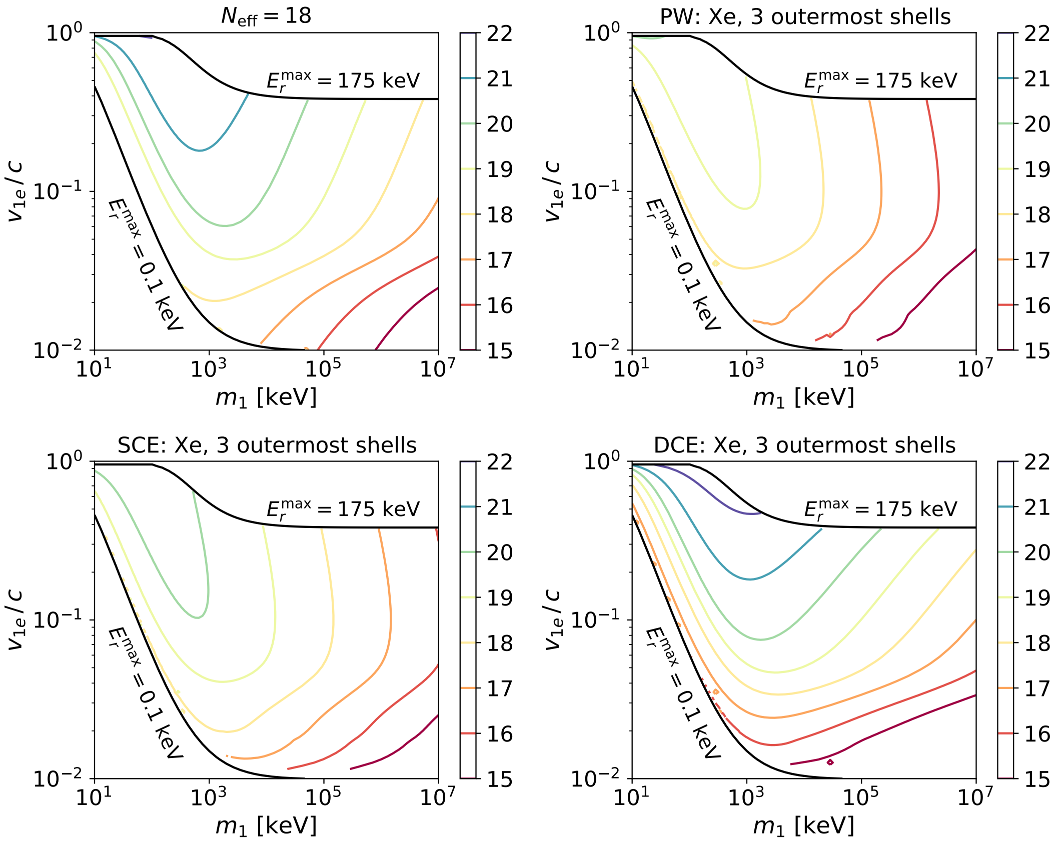

Figure 6.2: The log total rate of fast moving dark matter represented by colored contours for the VF model with mediator mass of 15 MeV. The four panels respectively represent the free scattering, PW, SCE and DCE cases. Only contributions from Xe 3 outermost shells are considered.

the three outermost shells of Xe atom for now. The black contours are there to indicate that we only select points with $0.1\,\mathrm{keV} < E_r^{\max} < 175\,\mathrm{keV}$[13]. We observe that total rate always increase towards the high speed but low mass region as anticipated from equation (6.12). But we shall keep in mind that there is always suppression in the total rate around $E_r^{\max} = 0.1$ keV due to detector effects. Additionally, we also see the deformation of the contour shapes due to the inclusion of the ionization form factor and we notice that the non-relativistic cases (PW and SCE) share very similar shapes while the relativistic one is

---

[13] In principle one can go beyond this region, however due to the detector effects of XENON1T, we chose to restrict the analysis to this range since the detector efficiency drops significantly below 1 keV and to avoid extrapolation beyond ~ 200 keV recoil energy.

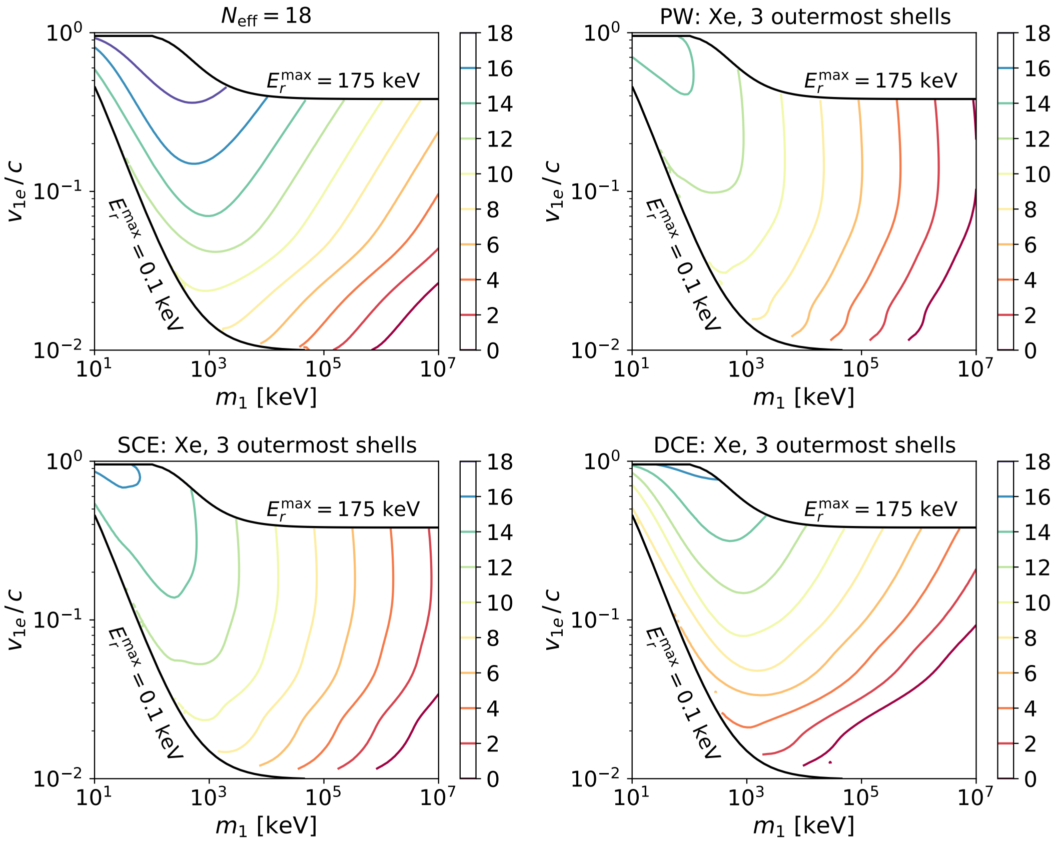

Figure 6.3: The log total rate of fast moving dark matter represented by colored contours for the PF model with mediator mass of 15 MeV. The four panels respectively represent the free scattering, PW, SCE and DCE cases. Only contributions from Xe 3 outermost shells are considered.

different. It is interesting to observe that, the contours shape of the relativistic case at high velocities has a great resemblance to that of free scattering, an indication of an asymptotic behavior of the cross section at high energies. Finally, notice when including ionization form factor, the contour lines have a clear cut-off near the bottom edge due to the fact that the incoming dark matter particle does not have enough energy to excite electrons. The kinks in the contours (except free scattering case) are due to the opening of different shells of Xe atom. In figure 6.3 we repeat the same as the previous one however this time we consider PF as the model with the mediator mass $m_a = 15$ MeV. In addition to the same remarks

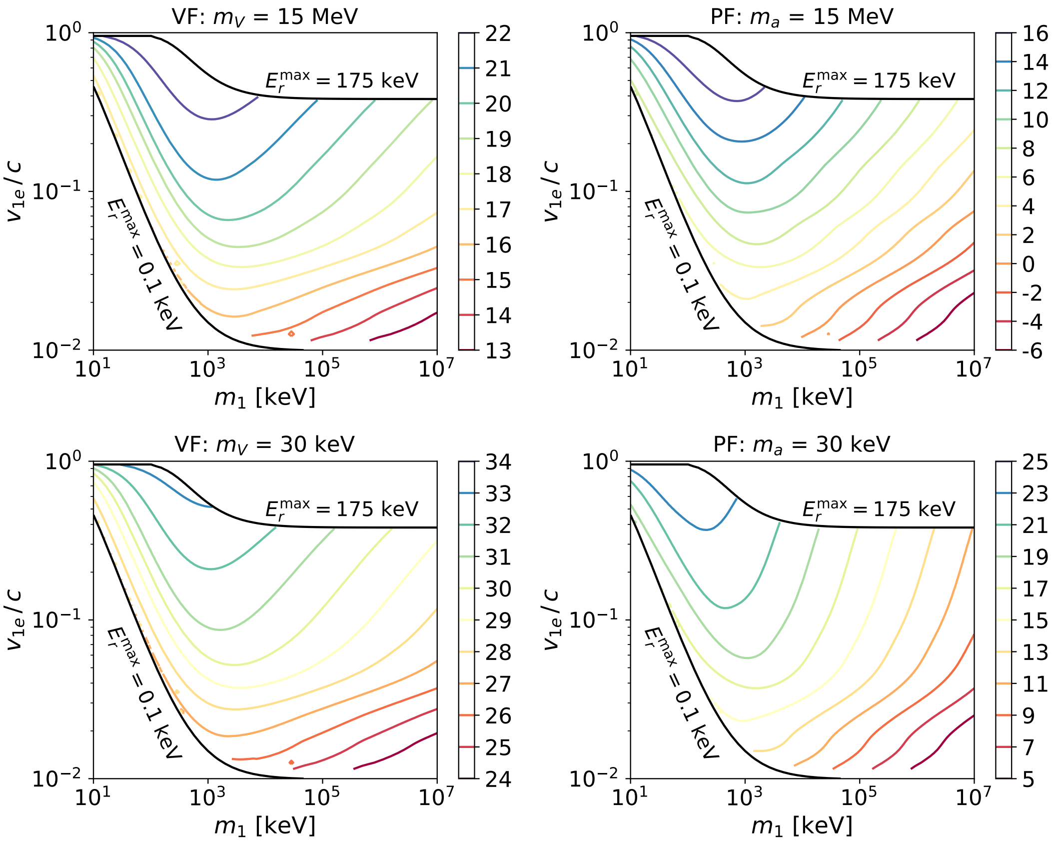

Figure 6.4: Comparison between VF and PF models in the left and right panel respectively with the mediator mass changing from 15 MeV in the top panel to 30 keV in the bottom panel. We only consider relativistic ionization form factor and contribution from all Xe atom shells.

as the VF case, notice the overall suppressed rate and its enormous range. As we noted in the previous chapter, we should keep in mind that the PW and the SCE are not suitable to the pseudo-scalar mediator since they are defined for vector and scalar mediators. Of course the above two figures can be repeated for all of the different models we considered in the previous chapter but to avoid repetition we limited ourselves to the above two cases only.

One other thing that may be worth considering is the inclusion of all allowed shells as well as different mediator masses. In figure 6.4 we include all contributing shells (using DCE approximation) of Xe atom and compare VF in the left panel to PF in the right panel with mediator mass of 15 MeV in the top panel and 30 keV in the bottom panel. We see that the shape of the rates in the VF case is not highly affected by different mediator masses. On the other hand, in the PF case, it is clear that there is substantial difference when considering different mediator masses in a considerable region of the parameter space. As evident in the bottom panel, the rate in general can be significantly enhanced when considering mediator masses well below the electron mass. Depending on the model details such as coupling parameters and the factor f_1, small mediator masses are more likely to be probed at experiments than higher mediator masses.

6.4 Mechanism Dependence: BDM as an Example

The discussion in the previous section is generic up to a choice of the factor f_1. It is generic in the fact that any model of the 7 cases introduced in the previous chapter can be applied as well as effects from the ionization form factors are properly accounted for. The only thing that is left is the factor of the fast moving dark matter component which becomes mechanism and velocity dependent based on how we interpret why dark matter gained such a high velocity. For example in the BDM scenario, f_1 can be recast from equation (3.9) as

$$f_1^{\mathrm{BDM}} \simeq 5.2 \times 10^{-18} \left(\frac{c}{v_{1e}}\right) \left(\frac{m_1}{\mathrm{GeV}}\right) \left(\frac{\langle \sigma_{00\to 11} v \rangle}{3 \times 10^{-26}\ \mathrm{cm}^3/\mathrm{s}}\right) \left(\frac{20\,\mathrm{GeV}}{m_0}\right)^2 . \tag{6.14}$$

This will lead to $f_1^{\mathrm{BDM}} \simeq 10^{-12}$ for BMP1, $f_1^{\mathrm{BDM}} \simeq 10^{-12}$ for BMP2 and $f_1^{\mathrm{BDM}} \simeq 10^{-16}$ for BMP3 of chapter 5. In this section, we will demonstrate how this factor can be included in the BDM scenario allowing any fast moving dark matter to be treated in a very similar manner. We will repeat similar analysis as in the previous section only this time we are going to use equation (6.14) instead of normalizing to f_1. In figure 6.5 we plot $\log\left[f_1^{\mathrm{BDM}}\right]$ and notice that contour values decrease while moving towards high velocity and high mass region as anticipated by equation (6.14) given that m_0 is related to the energy E_1 and hence to the velocity v_{1e} as described in chapter 3. We now repeat figure 6.4 by multiplying its

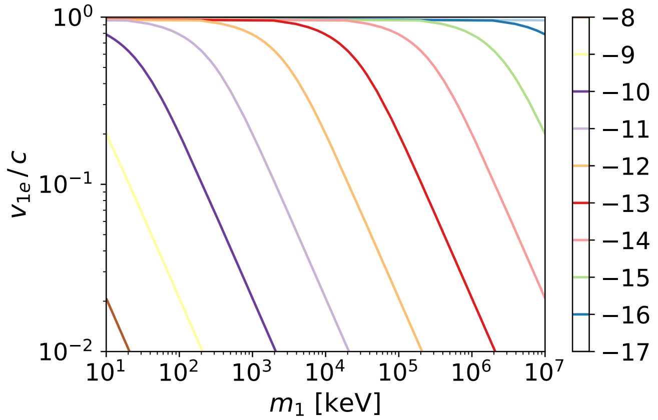

Figure 6.5: The log of the factor f_1^{BDM} that quantifies the amount of fast moving dark matter.

contour lines with those of figure 6.5. We also fix the couplings to: $g_e^i g_1^i = 10^{-4}$ and show the resulting total rate: $\log\left[\mathcal{R}^{\text{tot}} \times (\text{ton} \times \text{year})\right]$ in figure 6.6. First, we observe the overall difference in the shape of the contours due to the inclusion of f_1^{BDM}. They are slightly pushed to smaller mass values due to the effects observed in figure 6.5. Also, the rates are decreased due to suppression from very small values of f_1^{BDM} and the coupling choice. As we anticipated before, low mass mediators are more likely to be probed first due to their higher rates. In addition, at higher mediator masses the VF case is more likely to be studied first in comparison to the PF case which suffers from very small rates. For example, the PF case could at best generate 0.01 event per ton per year. According to our discussion in table 5.2 and figure 5.4, we generically predict models VS, SF and SS to behave in similar manner as the VF case (left panel of figure 6.6).

In summary of this chapter, we began by introducing a formalism for a generic fast moving dark matter particle without focusing on the mechanism that interprets its velocity. We derived a fully relativistic relation and showed that its non-relativistic limit is in agreement with current literature targeting WIMP-like dark matter. We took a very simplified regime in which the "high-speed" mechanism dependence is treated as an overall free constant parameter related to the factor, f_1. We then demonstrated how a specific mechanism, the BDM, can be accounted for in an attempt to provide a full framework for other and future

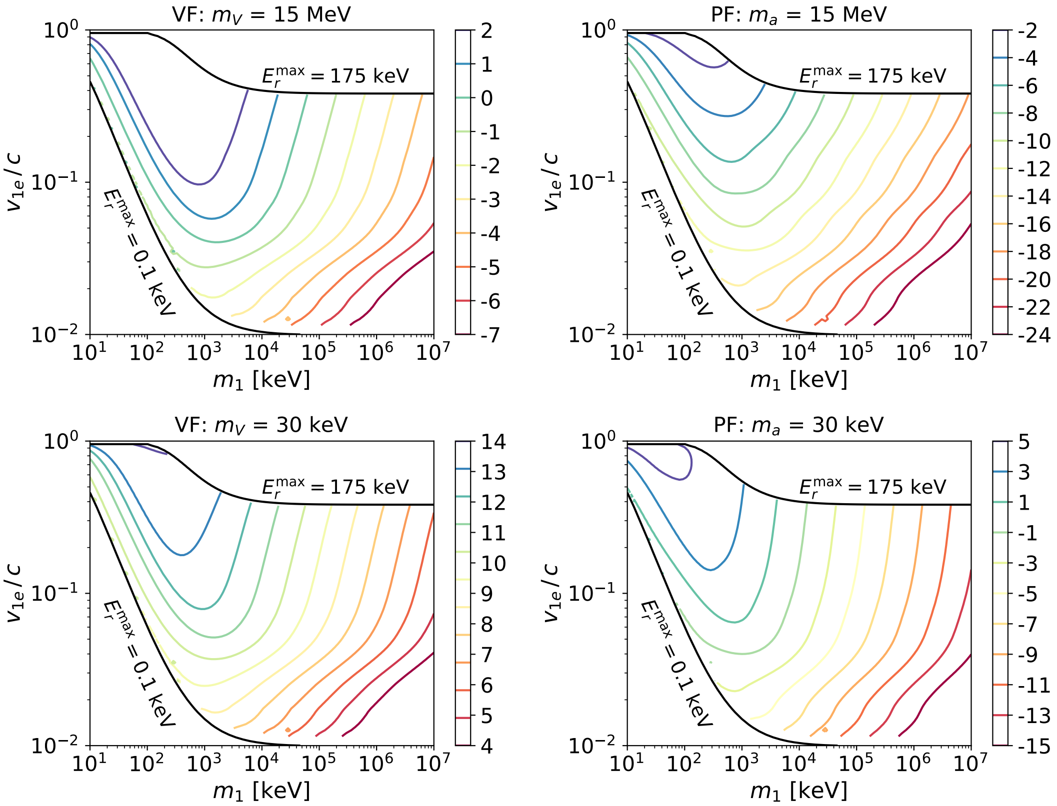

Figure 6.6: The same as figure 6.4 but this time considering BDM scenario by taking the factor in equation (6.14) instead of a fixed constant parameter.

mechanisms to be treated in a similar manner. We found that in the case of BDM, models with mediators that are either scalar or vector are more likely to be studied first at direct detection experiments due to the different effects from the matrix element squared as well as the ionization form factor.

Chapter 7

Conclusions

The universe is an open stage filled with many fundamental mysteries, one of which is the nearly century old dark matter puzzle. From fundamental theories to extraordinary experiments, a series of tireless endeavors to divulge its particle nature concluded with a null result so far. The tightened parameter space provided by direct detection experiments may drive dark matter phenomenology into the beyond-WIMP era.

Encouraged by some cosmological tensions, we motivated a dark matter scenario that remarkably evades the stringent direct detection constraints. Inspired by the sophistication of the SM, an enriched, non-minimal but simple dark sector is considered with different particles and interactions. We studied a model with two stable particles having a mass difference between them identifying the heavier one as the dominant component. While the lighter component is subdominant, we find that with a sufficient mass separation between the two components, a potential signal can be observed at some large-volume but high energy electron recoil experiments upon dark matter interaction with electrons. Because of the sufficient mass difference, when the heavier states annihilate to the lighter states, the lighter state will gain a high velocity “boost” hence named boosted dark matter. Since the signal would originate from the annihilation of two heavy dark matter states, we investigated two possible sources with different geometrical significance that are capable of hosting the heavy state particles with enough abundance. We compare the galactic center with its large geometrical size providing a high possible flux vs the Sun as a point-like source with lower flux but rather precise directionality and closer proximity to detectors on Earth. The setup of our model brings a very distinct but interesting phenomenology at deep underground experiments such as SK, HK and DUNE. For example we find that a unique signal emerging from the Sun could provide a smoking-gun evidence on the dark matter nature. Moreover, we find that the future DUNE detector with its better angular resolution and particle identification capabilities serves as a perfect experiment to study these types of signal broadening its scope beyond its current purpose as a neutrino experiment. Additionally, we conclude that, SK and HK on one hand and DUNE on the other hand can potentially be complementary to each other due to their different energy threshold.

Though it served as a proof of principle, the previous consideration was limited to a specific mass hierarchy in the dark sector. For this reason, we also relaxed the sufficient mass splitting condition as well as to assume an arbitrary mass for the dark mediator. Such a setup allows one to probe dark matter scattering with electrons at low electron recoils, a necessity for exploiting the full boosted dark matter parameter space. However, this on the other hand brings important atomic physics effects into the picture due to the small momentum transfer from dark matter to the electrons. We investigate this effect in the form of the ionization form factor by exploring several approaches serving different relativistic regimes. In contrast to WIMP-like dark matter, we stress that boosted dark matter must be accompanied by relativistic treatment of the atomic physics effects. For this reason, in the entire analysis of this thesis, we implemented a fully relativistic framework to describe dark matter interaction with electrons while providing the necessary comparison with the non-relativistic approach when needed. Moreover, in preparation for extending the previous model into a class of models considering different spins of the dark particles, we highlight the significance of the relativistic treatment. For instance, mediators such as pseudo-scalar and axial-vector find their relativistic treatment more natural. As a case study, we find that the recent XENON1T excess is a motivation and a concrete example of the capability of direct detection experiments to probe such dark matter scenarios providing a complementary search to large volume neutrino experiments.

After we generalized the specific boosted dark matter regime into multiple models and arbitrary mediator mass, we observed that our treatment could be generalized even more to accommodate a generic fast moving dark matter, allowing a mechanism-independent framework. Fully equipped with a relativistic treatment of the atomic physics effects on electron scattering, we derived a generic formula to estimate the dark matter rates and took direct detection experiments as an example for detection prospects. We proved that the non-relativistic limit of our framework results in a relation that agrees with existing ones targeting WIMP-like dark matter. We also demonstrated how such a framework can be used to study mechanism-dependent scenarios such as boosted dark matter. With this demonstration, we allow other and future mechanisms that provide an interpretation of fast moving dark matter to be treated on equal footing.

Finally, extending dark matter to models beyond non-minimal scenarios does not only provide a pathway towards new abstract ideas but rather sheds light on unexplored testable hypotheses. A simple tweak in the assumptions of dark matter leads to an interesting new phenomenology at various experiments. Given the current stringent experimental constraints on traditional dark matter, new ideas of dark matter such as non-minimal scenarios could be the way forward to discover dark matter in the near future.

References

[1] S. van den Bergh, *The Early history of dark matter*, *Publ. Astron. Soc. Pac.* **111** (1999) 657, [`astro-ph/9904251`].

[2] K. Garrett and G. Duda, *Dark Matter: A Primer*, *Adv. Astron.* **2011** (2011) 968283, [`1006.2483`].

[3] G. Bertone and D. Hooper, *History of dark matter*, *Rev. Mod. Phys.* **90** (2018) 045002, [`1605.04909`].

[4] F. Zwicky, *Die Rotverschiebung von extragalaktischen Nebeln*, *Helv. Phys. Acta* **6** (1933) 110–127.

[5] F. Zwicky, *On the Masses of Nebulae and of Clusters of Nebulae*, *Astrophys. J.* **86** (1937) 217–246.

[6] S. Smith, *The Mass of the Virgo Cluster*, *Astrophys. J.* **83** (1936) 23–30.

[7] H. W. Babcock, *The rotation of the Andromeda Nebula*, *Lick Observatory Bulletin* **498** (1939) 41–51.

[8] M. S. Roberts and R. N. Whitehurst, *The rotation curve and geometry of M31 at large galactocentric distances.*, *Astrophys. J.* **201** (oct, 1975) 327–346.

[9] C. Carignan, L. Chemin, W. K. Huchtmeier and F. J. Lockman, *Extended hi rotation curve and mass distribution of m31*, *Astrophys. J. Lett.* **641** (2006) L109–L112, [`astro-ph/0603143`].

[10] D. H. Rogstad and G. S. Shostak, *Gross Properties of Five Scd Galaxies as Determined from 21-CENTIMETER Observations*, *Astrophys. J.* **176** (Sept., 1972) 315.

[11] R. Massey, T. Kitching and J. Richard, *The dark matter of gravitational lensing*, *Rept. Prog. Phys.* **73** (2010) 086901, [`1001.1739`].

[12] R. Ellis, *Gravitational lensing: A unique probe of dark matter and dark energy*, *Philosophical transactions. Series A, Mathematical, physical, and engineering sciences* **368** (03, 2010) 967–87.

[13] A. S. Bolton, S. Burles, L. V. E. Koopmans, T. Treu, R. Gavazzi, L. A. Moustakas et al., *The Sloan Lens ACS Survey. V. The Full ACS Strong-Lens Sample*, *Astrophys. J.* **682** (2008) 964–984, [`0805.1931`].

[14] L. van Waerbeke et al., *Detection of correlated galaxy ellipticities on CFHT data: First evidence for gravitational lensing by large scale structures*, *Astron. Astrophys.* **358** (2000) 30–44, [`astro-ph/0002500`].

[15] N. Kaiser, G. Wilson and G. A. Luppino, *Large scale cosmic shear measurements*, `astro-ph/0003338`.

[16] D. M. Wittman, J. A. Tyson, D. Kirkman, I. Dell'Antonio and G. Bernstein, *Detection of weak gravitational lensing distortions of distant galaxies by cosmic dark matter at large scales*, *Nature* **405** (2000) 143–149, [`astro-ph/0003014`].

[17] D. J. Bacon, A. R. Refregier and R. S. Ellis, *Detection of weak gravitational lensing by large-scale structure*, *Mon. Not. Roy. Astron. Soc.* **318** (2000) 625, [`astro-ph/0003008`].

[18] H. Hoekstra, H. K. C. Yee and M. D. Gladders, *Properties of galaxy dark matter halos from weak lensing*, *Astrophys. J.* **606** (2004) 67–77, [`astro-ph/0306515`].

[19] EROS-2 collaboration, P. Tisserand et al., *Limits on the Macho Content of the Galactic Halo from the EROS-2 Survey of the Magellanic Clouds*, *Astron. Astrophys.* **469** (2007) 387–404, [`astro-ph/0607207`].

[20] Particle Data Group collaboration, M. Tanabashi et al., *Review of Particle Physics*, *Phys. Rev. D* **98** (2018) 030001.

[21] WMAP collaboration, C. L. Bennett et al., *Nine-Year Wilkinson Microwave Anisotropy Probe (WMAP) Observations: Final Maps and Results*, *Astrophys. J. Suppl.* **208** (2013) 20, [`1212.5225`].

[22] Planck collaboration, N. Aghanim et al., *Planck 2018 results. VI. Cosmological parameters*, *Astron. Astrophys.* **641** (2020) A6, [`1807.06209`].

[23] D. Clowe, M. Bradac, A. H. Gonzalez, M. Markevitch, S. W. Randall, C. Jones et al., *A direct empirical proof of the existence of dark matter*, *Astrophys. J. Lett.* **648** (2006) L109–L113, [`astro-ph/0608407`].

[24] M. Bradac, S. W. Allen, T. Treu, H. Ebeling, R. Massey, R. G. Morris et al., *Revealing the properties of dark matter in the merging cluster MACSJ0025.4-1222*, *Astrophys. J.* **687** (2008) 959, [`0806.2320`].

[25] M. Davis, J. Huchra, D. W. Latham and J. Tonry, *A survey of galaxy redshifts. II. The large scale space distribution.*, *ApJ* **253** (Feb., 1982) 423–445.

[26] M. Iye, K. Ota, N. Kashikawa, H. Furusawa, T. Hashimoto, T. Hattori et al., *A galaxy at a redshift $z = 6.96$*, *Nature* **443** (2006) 186–188, [`astro-ph/0609393`].

[27] S. D. M. White, C. S. Frenk and M. Davis, *Clustering in a neutrino-dominated universe*, *ApJ* **274** (Nov., 1983) L1–L5.

[28] G. Arcadi, M. Dutra, P. Ghosh, M. Lindner, Y. Mambrini, M. Pierre et al., *The waning of the WIMP? A review of models, searches, and constraints*, *Eur. Phys. J. C* **78** (2018) 203, [`1703.07364`].

[29] M. Taoso, G. Bertone and A. Masiero, *Dark Matter Candidates: A Ten-Point Test*, *JCAP* **03** (2008) 022, [`0711.4996`].

[30] J. R. Bond and A. S. Szalay, *The Collisionless Damping of Density Fluctuations in an Expanding Universe*, *Astrophys. J.* **274** (1983) 443–468.

[31] J. R. Bond, A. S. Szalay, J. Centrella and J. R. Wilson, *DARK MATTER AND SHOCKED PANCAKES*, in *3rd Moriond Astrophysics Meeting: Galaxies and the Early Universe*, pp. 87–99, 1983.

[32] C. Yèche, N. Palanque-Delabrouille, J. Baur and H. du Mas des Bourboux, *Constraints on neutrino masses from Lyman-alpha forest power spectrum with BOSS and XQ-100*, *JCAP* **06** (2017) 047, [`1702.03314`].

[33] M. Viel, G. D. Becker, J. S. Bolton and M. G. Haehnelt, *Warm dark matter as a solution to the small scale crisis: New constraints from high redshift Lyman-α forest data*, *Phys. Rev. D* **88** (2013) 043502, [`1306.2314`].

[34] T. Hambye, *On the stability of particle dark matter*, *PoS* **IDM2010** (2011) 098, [`1012.4587`].

[35] Y. Mambrini, S. Profumo and F. S. Queiroz, *Dark Matter and Global Symmetries*, *Phys. Lett. B* **760** (2016) 807–815, [`1508.06635`].

[36] P. Gondolo and G. Gelmini, *Cosmic abundances of stable particles: Improved analysis*, *Nucl. Phys. B* **360** (1991) 145–179.

[37] G. Belanger, F. Boudjema, A. Pukhov and A. Semenov, *micrOMEGAs_3: A program for calculating dark matter observables*, *Comput. Phys. Commun.* **185** (2014) 960–985, [`1305.0237`].

[38] G. F. Chapline, *Cosmological effects of primordial black holes*, *Nature* **253** (1975) 251–252.

[39] B. Carr, K. Kohri, Y. Sendouda and J. Yokoyama, *Constraints on Primordial Black Holes*, `2002.12778`.

[40] C. Boehm and P. Fayet, *Scalar dark matter candidates*, *Nucl. Phys. B* **683** (2004) 219–263, [`hep-ph/0305261`].

[41] H. Baer, K.-Y. Choi, J. E. Kim and L. Roszkowski, *Dark matter production in the early Universe: beyond the thermal WIMP paradigm*, *Phys. Rept.* **555** (2015) 1–60, [`1407.0017`].

[42] L. Roszkowski, E. M. Sessolo and S. Trojanowski, *WIMP dark matter candidates and searches—current status and future prospects*, *Rept. Prog. Phys.* **81** (2018) 066201, [`1707.06277`].

[43] J. Fan, M. Reece and L.-T. Wang, *Non-relativistic effective theory of dark matter direct detection*, *JCAP* **11** (2010) 042, [`1008.1591`].

[44] A. L. Fitzpatrick, W. Haxton, E. Katz, N. Lubbers and Y. Xu, *The Effective Field Theory of Dark Matter Direct Detection*, *JCAP* **02** (2013) 004, [`1203.3542`].

[45] G. Arcadi, A. Djouadi and M. Raidal, *Dark Matter through the Higgs portal*, *Phys. Rept.* **842** (2020) 1–180, [`1903.03616`].

[46] L. J. Hall, K. Jedamzik, J. March-Russell and S. M. West, *Freeze-In Production of FIMP Dark Matter*, *JHEP* **03** (2010) 080, [`0911.1120`].

[47] A. Boyarsky, M. Drewes, T. Lasserre, S. Mertens and O. Ruchayskiy, *Sterile neutrino Dark Matter*, *Prog. Part. Nucl. Phys.* **104** (2019) 1–45, [`1807.07938`].

[48] R. D. Peccei and H. R. Quinn, *CP Conservation in the Presence of Instantons*, *Phys. Rev. Lett.* **38** (1977) 1440–1443.

[49] P. Arias, D. Cadamuro, M. Goodsell, J. Jaeckel, J. Redondo and A. Ringwald, *WISPy Cold Dark Matter*, *JCAP* **06** (2012) 013, [`1201.5902`].

[50] W. Hu, R. Barkana and A. Gruzinov, *Cold and fuzzy dark matter*, *Phys. Rev. Lett.* **85** (2000) 1158–1161, [`astro-ph/0003365`].

[51] L. Hui, J. P. Ostriker, S. Tremaine and E. Witten, *Ultralight scalars as cosmological dark matter*, *Phys. Rev. D* **95** (2017) 043541, [`1610.08297`].

[52] E. G. M. Ferreira, *Ultra-Light Dark Matter*, `2005.03254`.

[53] M. Schumann, *Direct Detection of WIMP Dark Matter: Concepts and Status*, *J. Phys. G* **46** (2019) 103003, [`1903.03026`].

[54] J. D. Lewin and P. F. Smith, *Review of mathematics, numerical factors, and corrections for dark matter experiments based on elastic nuclear recoil*, *Astropart. Phys.* **6** (1996) 87–112.

[55] J. Billard et al., *Direct Detection of Dark Matter – APPEC Committee Report*, `2104.07634`.

[56] R. K. Leane, *Indirect Detection of Dark Matter in the Galaxy*, in *3rd World Summit on Exploring the Dark Side of the Universe*, 5, 2020. `2006.00513`.

[57] C. A. Argüelles, A. Diaz, A. Kheirandish, A. Olivares-Del-Campo, I. Safa and A. C. Vincent, *Dark Matter Annihilation to Neutrinos*, `1912.09486`.

[58] B. M. Roach, K. C. Y. Ng, K. Perez, J. F. Beacom, S. Horiuchi, R. Krivonos et al., *NuSTAR Tests of Sterile-Neutrino Dark Matter: New Galactic Bulge Observations and Combined Impact*, *Phys. Rev. D* **101** (2020) 103011, [`1908.09037`].

[59] C. Pérez de los Heros, *Status, Challenges and Directions in Indirect Dark Matter Searches*, *Symmetry* **12** (2020) 1648, [`2008.11561`].

[60] P. J. Fox, R. Harnik, J. Kopp and Y. Tsai, *LEP Shines Light on Dark Matter*, *Phys. Rev. D* **84** (2011) 014028, [`1103.0240`].

[61] J. R. Ellis, D. V. Nanopoulos, L. Roszkowski and D. N. Schramm, *Dark matter in the light of LEP*, *Phys. Lett. B* **245** (1990) 251–257.

[62] Y. Bai, P. J. Fox and R. Harnik, *The Tevatron at the Frontier of Dark Matter Direct Detection*, *JHEP* **12** (2010) 048, [`1005.3797`].

[63] CMS collaboration, A. M. Sirunyan et al., *Combined search for electroweak production of charginos and neutralinos in proton-proton collisions at* $\sqrt{s} = 13$ *TeV*, *JHEP* **03** (2018) 160, [`1801.03957`].

[64] ATLAS collaboration, M. Aaboud et al., *Search for electroweak production of supersymmetric particles in final states with two or three leptons at* $\sqrt{s} = 13$ *TeV with the ATLAS detector*, *Eur. Phys. J. C* **78** (2018) 995, [`1803.02762`].

[65] ATLAS collaboration, G. Aad et al., *Search for new resonances in mass distributions of jet pairs using 139* fb^{-1} *of pp collisions at* $\sqrt{s} = 13$ *TeV with the ATLAS detector*, *JHEP* **03** (2020) 145, [`1910.08447`].

[66] CMS collaboration, A. M. Sirunyan et al., *Search for high mass dijet resonances with a new background prediction method in proton-proton collisions at* $\sqrt{s} = 13$ *TeV*, *JHEP* **05** (2020) 033, [`1911.03947`].

[67] O. Buchmueller, C. Doglioni and L. T. Wang, *Search for dark matter at colliders*, *Nature Phys.* **13** (2017) 217–223, [`1912.12739`].

[68] ATLAS, CMS collaboration, M. Felcini, *Searches for Dark Matter Particles at the LHC*, in *53rd Rencontres de Moriond on Cosmology*, 9, 2018. `1809.06341`.

[69] A. Boveia and C. Doglioni, *Dark Matter Searches at Colliders*, *Ann. Rev. Nucl. Part. Sci.* **68** (2018) 429–459, [`1810.12238`].

[70] B. Penning, *The pursuit of dark matter at colliders—an overview*, *J. Phys. G* **45** (2018) 063001, [`1712.01391`].

[71] G. Belanger and J.-C. Park, *Assisted freeze-out*, *JCAP* **03** (2012) 038, [`1112.4491`].

[72] H. S. Cheon, S. K. Kang and C. S. Kim, *Doubly Coexisting Dark Matter Candidates in an Extended Seesaw Model*, *Phys. Lett. B* **675** (2009) 203–209, [`0807.0981`].

[73] J. Kopp, J. Liu and X.-P. Wang, *Boosted Dark Matter in IceCube and at the Galactic Center*, *JHEP* **04** (2015) 105, [`1503.02669`].

[74] A. Bhattacharya, R. Gandhi, A. Gupta and S. Mukhopadhyay, *Boosted Dark Matter and its implications for the features in IceCube HESE data*, *JCAP* **05** (2017) 002, [`1612.02834`].

[75] F. D'Eramo and J. Thaler, *Semi-annihilation of Dark Matter*, *JHEP* **06** (2010) 109, [`1003.5912`].

[76] T. Hambye, *Hidden vector dark matter*, *JHEP* **01** (2009) 028, [`0811.0172`].

[77] T. Hambye and M. H. G. Tytgat, *Confined hidden vector dark matter*, *Phys. Lett. B* **683** (2010) 39–41, [`0907.1007`].

[78] C. Arina, T. Hambye, A. Ibarra and C. Weniger, *Intense Gamma-Ray Lines from Hidden Vector Dark Matter Decay*, *JCAP* **03** (2010) 024, [`0912.4496`].

[79] G. Belanger, K. Kannike, A. Pukhov and M. Raidal, *Impact of semi-annihilations on dark matter phenomenology - an example of Z_N symmetric scalar dark matter*, *JCAP* **04** (2012) 010, [`1202.2962`].

[80] E. D. Carlson, M. E. Machacek and L. J. Hall, *Self-interacting dark matter*, *Astrophys. J.* **398** (1992) 43–52.

[81] Y. Hochberg, E. Kuflik, T. Volansky and J. G. Wacker, *Mechanism for Thermal Relic Dark Matter of Strongly Interacting Massive Particles*, *Phys. Rev. Lett.* **113** (2014) 171301, [`1402.5143`].

[82] A. A. de Laix, R. J. Scherrer and R. K. Schaefer, *Constraints of selfinteracting dark matter*, *Astrophys. J.* **452** (1995) 495, [`astro-ph/9502087`].

[83] K. Agashe, Y. Cui, L. Necib and J. Thaler, *(In)direct Detection of Boosted Dark Matter*, *JCAP* **10** (2014) 062, [`1405.7370`].

[84] A. Bhattacharya, R. Gandhi and A. Gupta, *The Direct Detection of Boosted Dark Matter at High Energies and PeV events at IceCube*, *JCAP* **03** (2015) 027, [`1407.3280`].

[85] J. F. Cherry, M. T. Frandsen and I. M. Shoemaker, *Direct Detection Phenomenology in Models Where the Products of Dark Matter Annihilation Interact with Nuclei*, *Phys. Rev. Lett.* **114** (2015) 231303, [`1501.03166`].

[86] J. Huang and Y. Zhao, *Dark Matter Induced Nucleon Decay: Model and Signatures*, *JHEP* **02** (2014) 077, [`1312.0011`].

[87] J. Berger, Y. Cui and Y. Zhao, *Detecting Boosted Dark Matter from the Sun with Large Volume Neutrino Detectors*, *JCAP* **02** (2015) 005, [`1410.2246`].

[88] K. Kong, G. Mohlabeng and J.-C. Park, *Boosted dark matter signals uplifted with self-interaction*, *Phys. Lett. B* **743** (2015) 256–266, [`1411.6632`].

[89] H. Alhazmi, K. Kong, G. Mohlabeng and J.-C. Park, *Boosted Dark Matter at the Deep Underground Neutrino Experiment*, *JHEP* **04** (2017) 158, [`1611.09866`].

[90] L. Necib, J. Moon, T. Wongjirad and J. M. Conrad, *Boosted Dark Matter at Neutrino Experiments*, *Phys. Rev. D* **95** (2017) 075018, [`1610.03486`].

[91] S. Tulin and H.-B. Yu, *Dark Matter Self-interactions and Small Scale Structure*, *Phys. Rept.* **730** (2018) 1–57, [`1705.02358`].

[92] J. F. Navarro, V. R. Eke and C. S. Frenk, *The cores of dwarf galaxy halos*, *Mon. Not. Roy. Astron. Soc.* **283** (1996) L72–L78, [`astro-ph/9610187`].

[93] F. Governato et al., *At the heart of the matter: the origin of bulgeless dwarf galaxies and Dark Matter cores*, *Nature* **463** (2010) 203–206, [`0911.2237`].

[94] B. Moore, T. R. Quinn, F. Governato, J. Stadel and G. Lake, *Cold collapse and the core catastrophe*, *Mon. Not. Roy. Astron. Soc.* **310** (1999) 1147–1152, [`astro-ph/9903164`].

[95] R. A. Flores and J. R. Primack, *Observational and theoretical constraints on singular dark matter halos*, *Astrophys. J. Lett.* **427** (1994) L1–4, [`astro-ph/9402004`].

[96] A. A. Klypin, A. V. Kravtsov, O. Valenzuela and F. Prada, *Where are the missing Galactic satellites?*, *Astrophys. J.* **522** (1999) 82–92, [`astro-ph/9901240`].

[97] S. Trujillo-Gomez, A. Klypin, J. Primack and A. J. Romanowsky, *Galaxies in lcdm with halo abundance matching: Luminosity-velocity relation, baryonic mass-velocity relation, velocity function, and clustering*, *The Astrophysical Journal* **742** (Nov, 2011) 16.

[98] D. N. Spergel and P. J. Steinhardt, *Observational evidence for selfinteracting cold dark matter*, *Phys. Rev. Lett.* **84** (2000) 3760–3763, [`astro-ph/9909386`].

[99] A. H. G. Peter, M. Rocha, J. S. Bullock and M. Kaplinghat, *Cosmological Simulations with Self-Interacting Dark Matter II: Halo Shapes vs. Observations*, *Mon. Not. Roy. Astron. Soc.* **430** (2013) 105, [`1208.3026`].

[100] M. Rocha, A. H. G. Peter, J. S. Bullock, M. Kaplinghat, S. Garrison-Kimmel, J. Onorbe et al., *Cosmological Simulations with Self-Interacting Dark Matter I: Constant Density Cores and Substructure*, *Mon. Not. Roy. Astron. Soc.* **430** (2013) 81–104, [`1208.3025`].

[101] S. W. Randall, M. Markevitch, D. Clowe, A. H. Gonzalez and M. Bradac, *Constraints on the Self-Interaction Cross-Section of Dark Matter from Numerical Simulations of the Merging Galaxy Cluster 1E 0657-56*, *Astrophys. J.* **679** (2008) 1173–1180, [`0704.0261`].

[102] L. B. Okun, *LIMITS OF ELECTRODYNAMICS: PARAPHOTONS?*, *Sov. Phys. JETP* **56** (1982) 502.

[103] B. Holdom, *Two U(1)'s and Epsilon Charge Shifts*, *Phys. Lett. B* **166** (1986) 196–198.

[104] J.-H. Huh, J. E. Kim, J.-C. Park and S. C. Park, *Galactic 511 keV line from MeV milli-charged dark matter*, *Phys. Rev. D* **77** (2008) 123503, [`0711.3528`].

[105] E. J. Chun and J.-C. Park, *Dark matter and sub-GeV hidden U(1) in GMSB models*, *JCAP* **02** (2009) 026, [`0812.0308`].

[106] E. J. Chun, J.-C. Park and S. Scopel, *Dark matter and a new gauge boson through kinetic mixing*, *JHEP* **02** (2011) 100, [`1011.3300`].

[107] J.-C. Park and S. C. Park, *Radiatively decaying scalar dark matter through U(1) mixings and the Fermi 130 GeV gamma-ray line*, *Phys. Lett. B* **718** (2013) 1401–1406, [`1207.4981`].

[108] G. Bélanger, A. Goudelis, J.-C. Park and A. Pukhov, *Isospin-violating dark matter from a double portal*, *JCAP* **02** (2014) 020, [`1311.0022`].

[109] Super-Kamiokande collaboration, M. Fechner et al., *Kinematic reconstruction of atmospheric neutrino events in a large water Cherenkov detector with proton identification*, *Phys. Rev. D* **79** (2009) 112010, [`0901.1645`].

[110] Hyper-Kamiokande Working Group collaboration, E. Kearns et al., *Hyper-Kamiokande Physics Opportunities*, in *Community Summer Study 2013: Snowmass on the Mississippi*, 9, 2013. `1309.0184`.

[111] DUNE collaboration, R. Acciarri et al., *Long-Baseline Neutrino Facility (LBNF) and Deep Underground Neutrino Experiment (DUNE): Conceptual Design Report, Volume 2: The Physics Program for DUNE at LBNF*, `1512.06148`.

[112] DUNE collaboration, J. Yu, *Status and Plan of DUNE at Fermilab*, *PoS* **NuFact2019** (2020) 022.

[113] L. K. Pik, *PhD dissertation*, *University of Tokyo* (2012) .

[114] M. Kaplinghat, T. Linden and H.-B. Yu, *Galactic Center Excess in γ Rays from Annihilation of Self-Interacting Dark Matter*, *Phys. Rev. Lett.* **114** (2015) 211303, [`1501.03507`].

[115] J. F. Navarro, C. S. Frenk and S. D. M. White, *The Structure of cold dark matter halos*, *Astrophys. J.* **462** (1996) 563–575, [`astro-ph/9508025`].

[116] J. F. Navarro, C. S. Frenk and S. D. M. White, *A Universal density profile from hierarchical clustering*, *Astrophys. J.* **490** (1997) 493–508, [`astro-ph/9611107`].

[117] G. Cowan, K. Cranmer, E. Gross and O. Vitells, *Asymptotic formulae for likelihood-based tests of new physics*, *Eur. Phys. J. C* **71** (2011) 1554, [`1007.1727`].

[118] C.-S. Chen, F.-F. Lee, G.-L. Lin and Y.-H. Lin, *Probing Dark Matter Self-Interaction in the Sun with IceCube-PINGU*, *JCAP* **10** (2014) 049, [`1408.5471`].

[119] Super-Kamiokande collaboration, C. Kachulis et al., *Search for Boosted Dark Matter Interacting With Electrons in Super-Kamiokande*, *Phys. Rev. Lett.* **120** (2018) 221301, [`1711.05278`].

[120] Q.-H. Cao, R. Ding and Q.-F. Xiang, *Exploring for sub-MeV Boosted Dark Matter from Xenon Electron Direct Detection*, `2006.12767`.

[121] C. Bunge, J. Barrientos and A. Bunge, *Roothaan-Hartree-Fock Ground-State Atomic Wave Functions: Slater-Type Orbital Expansions and Expectation Values for Z = 2-54*, *Atom. Data Nucl. Data Tabl.* **53** (1993) 113–162.

[122] R. Essig, J. Mardon and T. Volansky, *Direct Detection of Sub-GeV Dark Matter*, *Phys. Rev. D* **85** (2012) 076007, [`1108.5383`].

[123] S. K. Lee, M. Lisanti, S. Mishra-Sharma and B. R. Safdi, *Modulation Effects in Dark Matter-Electron Scattering Experiments*, *Phys. Rev. D* **92** (2015) 083517, [`1508.07361`].

[124] J. Kopp, V. Niro, T. Schwetz and J. Zupan, *DAMA/LIBRA and leptonically interacting Dark Matter*, *Phys. Rev. D* **80** (2009) 083502, [`0907.3159`].

[125] R. Catena, T. Emken, N. A. Spaldin and W. Tarantino, *Atomic responses to general dark matter-electron interactions*, *Phys. Rev. Res.* **2** (2020) 033195, [`1912.08204`].

[126] F. J. Gálvez, E. Buendía, P. Maldonado and A. J. Sarsa, *Optimized effective potential energies and ionization potentials for the atoms Li to Ra*, *European Physical Journal D* **50** (Dec., 2008) 229–235.

[127] P. Maldonado, A. Sarsa, E. Buendía and F. Gálvez, *Relativistic, numerically parameterized, optimized, effective potentials for the ground state of the atoms He through Ra*, *Atom. Data Nucl. Data Tabl.* **97** (2011) 109–133.

[128] D. N. Laikov and K. R. Briling, *Atomic effective potentials for starting molecular electronic structure calculations*, *Theoretical Chemistry Accounts* **139** (Jan, 2020) .

[129] F. Salvat and J. M. Fernández-Varea, *radial: A fortran subroutine package for the solution of the radial schrödinger and dirac wave equations*, *Computer Physics Communications* **240** (2019) 165 – 177.

[130] B. Roberts, V. Dzuba, V. Flambaum, M. Pospelov and Y. Stadnik, *Dark matter scattering on electrons: Accurate calculations of atomic excitations and implications for the DAMA signal*, *Phys. Rev. D* **93** (2016) 115037, [`1604.04559`].

[131] O. Čertík, J. E. Pask and J. Vackář, *dftatom: A robust and general schrödinger and dirac solver for atomic structure calculations*, *Computer Physics Communications* **184** (Jul, 2013) 1777–1791.

[132] I. M. Bloch, A. Caputo, R. Essig, D. Redigolo, M. Sholapurkar and T. Volansky, *Exploring New Physics with O(keV) Electron Recoils in Direct Detection Experiments*, `2006.14521`.

[133] B. M. Roberts and V. V. Flambaum, *Electron-interacting dark matter: Implications from DAMA/LIBRA-phase2 and prospects for liquid xenon detectors and NaI detectors*, *Phys. Rev. D* **100** (2019) 063017, [`1904.07127`].

[134] XENON collaboration, E. Aprile et al., *Excess electronic recoil events in XENON1T*, *Phys. Rev. D* **102** (2020) 072004, [`2006.09721`].

[135] B. Bhattacherjee and R. Sengupta, *XENON1T Excess: Some Possible Backgrounds*, *Phys. Lett. B* **817** (2021) 136305, [`2006.16172`].

[136] K. Kannike, M. Raidal, H. Veermäe, A. Strumia and D. Teresi, *Dark Matter and the XENON1T electron recoil excess*, *Phys. Rev. D* **102** (2020) 095002, [`2006.10735`].

[137] L. Su, W. Wang, L. Wu, J. M. Yang and B. Zhu, *Atmospheric Dark Matter and Xenon1T Excess*, *Phys. Rev. D* **102** (2020) 115028, [`2006.11837`].

[138] G. Paz, A. A. Petrov, M. Tammaro and J. Zupan, *Shining dark matter in Xenon1T*, *Phys. Rev. D* **103** (2021) L051703, [`2006.12462`].

[139] Y. Jho, J.-C. Park, S. C. Park and P.-Y. Tseng, *Leptonic New Force and Cosmic-ray Boosted Dark Matter for the XENON1T Excess*, *Phys. Lett. B* **811** (2020) 135863, [`2006.13910`].

[140] B. Fornal, P. Sandick, J. Shu, M. Su and Y. Zhao, *Boosted Dark Matter Interpretation of the XENON1T Excess*, *Phys. Rev. Lett.* **125** (2020) 161804, [`2006.11264`].

[141] H. Alhazmi, D. Kim, K. Kong, G. Mohlabeng, J.-C. Park and S. Shin, *Implications of the XENON1T Excess on the Dark Matter Interpretation*, `2006.16252`.

[142] D. Buttazzo, P. Panci, D. Teresi and R. Ziegler, *Xenon1T excess from electron recoils of non-relativistic Dark Matter*, `2011.08919`.

[143] R. Essig, A. Manalaysay, J. Mardon, P. Sorensen and T. Volansky, *First Direct Detection Limits on sub-GeV Dark Matter from XENON10*, *Phys. Rev. Lett.* **109** (2012) 021301, [`1206.2644`].